Dust ejection from cometary nuclei and the formation of meteoroid streams

Nathan W. Harris
Department of Physics
University of Sheffield

Submitted for degree of Ph.D.
December 1994

BLANK
IN
ORIGINAL

11, VIII, X, 8. 52, 88, 134

Summary

Dust ejection from cometary nuclei and the formation of meteoroid streams

Nathan W. Harris

The relationship between meteoroid streams and meteor showers is discussed and a method for identifying stream meteoroids from a random meteoroid orbital parameter data set is described. Three different methods are used to estimate the sporadic to stream meteoroid ratio for a specific photographic meteor data set. This data set contains meteors with estimated causative meteoroid masses, m, in the range $0.001 \leq m \leq 1000$ g. The ratio is found to be 0.17 ± 0.04. The analysis also shows that 27 ± 3 per cent of the general sporadic background consists of undetected stream meteoroids. The physical characteristics (i.e. meteor magnitudes and causative meteoroid masses) of stream and sporadic meteoroids are compared and their orbital parameter distributions are then compared to those of the known short-period comets. The orbits of the 136 known short-period comets are replaced with 'typical' distributions of meteoroid orbits to produce 136 meteoroid streams. These orbits are then used to model the velocity distribution of large (mass $> 10^{-3}$ g) cometary meteoroids in the inner solar system. A velocity dependent factor is introduced to account for the observational selection that favours the detection of high velocity meteors.

The 'core' Perseid meteoroids are identified from photographic meteor data catalogues and the relationship between the mass and orbital semi-major axis of these Perseid meteoroids is investigated. It is found that there is no systematic variation in the spread of the semi-major axis data as a function of meteoroid mass and it is thus concluded that the meteoroid cometocentric ejection velocity is also independent of meteoroid mass. This leads to the further conclusion that the meteoroid radius-density product is a constant.

A model is developed to represent the dust ejection mechanism from comet P/Swift-Tuttle and the consequent formation of the Perseid meteoroid stream. The meteoroid cometocentric ejection velocity, emission plane orientation and sublimation activity are all factors that are considered. The modelled semi-major axis distributions are compared to that of the observed core photographic Perseids to determine the most appropriate model. The model that most closely resembles the observations is produced using a Maxwellian meteoroid ejection velocity distribution that peaks at a velocity of 0.6 km s^{-1}, and a meteoroid ejection lag angle of $-5°$. It is thus concluded that the nucleus of P/Swift-Tuttle spins slowly in a prograde mode and that around 14% (by number) of the dust particles lost by the comet are placed onto hyperbolic orbits. The modelled Perseid meteoroid orbital parameters are used to determine

the ecliptic distribution of meteoroid descending nodes and an estimate is made of the Perseid meteoroid influx as the Earth passes through the stream.

The model is improved by allowing for the past orbital evolution of the parent comet due to planetary perturbations. The orbit of P/Swift-Tuttle is integrated back over 270,000 years. Modelled Perseid meteoroids are ejected from the comet orbit at 5000 year intervals of orbital evolution, over the last 160,000 years BP and the ecliptic distribution of modelled meteoroid descending nodes is again determined. It is seen that the Earth only intersects the 'inner edge' of the dust complex, although it does pass close to the centre of the most recently formed concentration of meteoroid orbits. A new estimate is made of the Perseid meteoroid influx as the Earth passes through the dust complex. The modelled Perseid meteor radiant distribution is determined and compared with the observed radiant distribution.

The spatial and size distribution of main belt asteroids is reviewed. The mass distribution index is found to be 2.09 ± 0.1. Using this result, an estimate of the total mass of the asteroid belt, $M_A(\mathrm{g})$, is made. This is found to be $\log M_A(\mathrm{g}) = 26.21(+1.4, -1.0)$. It is concluded that the Trojan asteroid population is significantly larger than observations indicate. The Koronis family of asteroids is discussed and a method for calculating the mass of the parent body is developed. Taking 243 Ida as an example, the collisional history of the family is investigated and the collision velocity distribution of Koronis family asteroids is modelled. It is concluded that 243 Ida is around 11 times more likely to be hit by a main belt asteroid than an asteroid in its own family and the largest main belt asteroid that Ida has encountered during its collisional history is one of diameter around 10 km.

The orbital classification and potential sources of Near Earth Asteroids (NEAs) are briefly discussed. Using an orbital data set of 255 NEAs, the Earth-impact velocity distribution is determined. The mean intersection velocity is found to be 20.8 km s^{-1} and the standard deviation of the data about the mean value is 6.2 km s^{-1}. It is also found that there exists an anomalous population of low diameter (< 2 km), low eccentricity ($e < 0.225$) NEAs with perihelia near to the Earth's orbit. Possible explanations for these observations are considered. The mass distribution index of NEAs is estimated by analysing the size distribution of Lunar impact-craters. The index is found to be 1.64 ± 0.01, considerably less than that for the main belt asteroids.

Preface and acknowledgements

This thesis documents the majority of the work that I have performed during my three years as a Ph.D. research student. Much of the work contained within has been published (or accepted for publication) in refereed scientific journals and the remaining work will hopefully form the basis for future publications.

I would like to thank David Hughes for being keen to have me as a research student and also for his constant support and encouragement throughout my studies. I am also grateful to the SERC for funding the research work. General thanks go to Clive, James, Neil McB., Hugo, Neil C., Bob and Bill for all their help, support, discussions and contributions.

Contents

List of Figures

List of Figures

List of Tables

Chapter 1

A brief introduction

The Sun and its eight planets (nine if you count Pluto) are the major bodies of the solar system, of which the Sun accounts for around 99% of the total mass. The solar system is also populated by a multitude of smaller or minor bodies, namely the asteroids, comets and meteoroids. The minor planets, or asteroids, revolve around the Sun mainly between the orbits of Mars and Jupiter in a wide belt of rocky/metallic debris (see Chapter 5), the remnants of a 'failed' planetary accretion process. The largest asteroid observed today, Ceres, is only around 924 km in diameter ($\sim 2 \times 10^{24}$ g) and the smallest are of the order of a few metres (although this is almost certainly not a lower limit). The majority of observed asteroids have diameters, D_{ast}, in the range $10 < D_{ast} < 55$ km. This diameter range, however, is purely due to observational selection and not a clue as to the size distribution of the asteroids. The numbers of observed asteroids with diameters less than 130 km begins to decrease due to the fact that they are more difficult to detect from Earth. The total mass of the asteroid belt, M_A(g), was estimated by Hughes & Harris (1994) to be $\log M_A(\mathrm{g}) = 26.21(+1.4, -1.0)$. During the calculation it was assumed that the majority of the mass of the belt is contained in the smaller, undetected bodies. This total mass amounts to approximately half the mass of Mercury.

Apart from the asteroids, the solar system is populated with meteoroid particles varying in size from about a micron (10^{-6} m) to hundreds of metres in diameter. The higher end of this meteoroid size spectrum (diameter > 1 m, say) could conceivably be classified as asteroidal bodies (as are the Near Earth Asteroids described in Chapter 6). Some of these meteoroid particles collide with the Earth's atmosphere. The smaller, micron-sized fragments (micro-meteoroids) are too small to produce any visible effect. Larger meteoroids (1mm up to tens of cm) cause the atmospheric phenomenon of meteors, colloquially known as 'shooting stars', as they 'burn up', or ablate, at about 100 km altitude (see Chapter 2). Even larger chunks of rocky or iron composition cause the rare and brilliant 'fireballs', some of which survive their high-speed ($\sim 15 - 20$ km s^{-1}) flight through the Earth's atmosphere and may later be recovered at ground level as meteorites. Such objects are very important in

providing examples of extraterrestrial rocks and thus giving the composition of some of the most primitive material left in the solar system. Collisions with very large meteoroids (or small asteroids) are now, fortunately, very rare. However, the large meteorite crater in Arizona is one recent reminder that such collisions still occur, although much less frequently now than earlier in the history of the planetary system. The mean collision velocity between an asteroid and the Earth is found to be 20.8 ± 6.2 km s^{-1} (see Harris & Hughes, 1994, and Chapter 6). The surfaces of Mercury, Venus, Mars, the Moon and other planetary satellites still show the scars from collisions with a multitude of objects of up to tens of km in diameter.

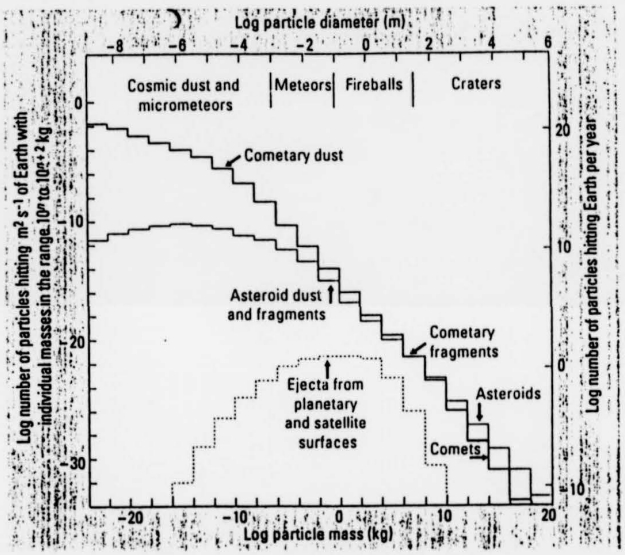

Figure 1.1: The influx of interplanetary material to Earth (taken from Hughes, 1993). The vertical histogram bars represent the logarithm of the number of particles in the specific mass region between 10^n and 10^{n+2} kg that hit Earth each year. Three components of the flux are shown, these being cometary (bold line), asteroidal (light line) and ejecta (broken line).

Comets are still enigmatic objects which, from time to time, provide a spectacular sight. They appear in the sky as having a bright head known as the coma, and may develop a long luminous tail. They consist of a small solid nucleus (typically 1-10 km diameter) made up from a low-density (< 1 g cm^{-3}) frozen conglomerate of dust and 'snowy' materials (mainly H_2O [around 95%], but also NH_3, CH_4, CO_2, CO, N_2 and HCN) often described as a 'dirty snowball', where the dust to snow mass ratio is typically of the order 0.1 to 1 (see Wyckoff, 1982). The masses of observed comets are thought to be in the range 10^{12} to 10^{18} g. Comets can be crudely split up into three groups according to their orbital periods. Those with orbital periods less than 15 years are referred to as 'short-period', those with periods between 15 and 200 years are referred to as 'intermediate-period' and those with periods greater than

200 years as 'long-period'.

Cometary nuclei are thought to be the left-over planetesimal building blocks of the cores of the outer planets which have been gravitationally perturbed back into the inner solar system. The source of the short-period comets is probably a disk of left-over cometary planetesimals that orbits the Sun at a heliocentric distance of between 40 and 100 AU (known as the Kuiper belt [see Luu, 1994]), although it is also possible that some low inclination long-period comets are eventually transformed into intermediate- or short-period comets by successive close approaches to the major planets. The long-period comets are thought to originate from a vast swarm of $\sim 10^{12}$ comets which lies at the very edge of the solar system ($\sim 50,000$ AU), known as the Oort cloud (Oort, 1950). The intermediate-period comets, as their name suggests, are in a transition stage between long- and short-period orbits. Their origins could have been the Oort cloud and/or the Kuiper belt. A very small fraction of these three types of objects have actually been observed. There are records of $\sim$ 1300 different comets and orbital data is available for around 750 of them (see Marsden's Catalogue of Cometary Orbits, 1986). Of these, 136 are short- and intermediate-period comets (see Fig. 1.2). The majority of the short-period comets belong to the 'Jupiter family', a population of cometary bodies that have been gravitationally captured by Jupiter so that their aphelia (furthest distance from the Sun) are concentrated near Jupiter's orbit ($\sim$ 5.2 AU).

In their highly elliptical orbits, the majority of cometary nuclei spend most of their existence at heliocentric distances, r, greater than 3 AU. At these distances, the temperature is very low because of the feeble solar radiation, so that all the icy materials are solid. Periodically, when each comet returns to the inner parts of the solar system, the increasing solar radiation heats the surface layers, evaporating the volatile ices, which carry the surface dust away from the cometary nucleus, forming the expansive coma. The volatile activity of the nucleus surface is not uniform. The GIOTTO spacecraft mission to comet P/Halley in 1986 indicated that the nucleus surface had 3 active regions that covered around 10% of the total surface area, from which around 95% of the mass loss originated. The remainder of the nucleus surface is thought to be covered in an insulating layer of loosely packed dust (thickness of the order of centimetres). After this heating up and evaporating process, the ultra-violet component of sunlight further breaks down the parent icy molecules, a process known as photo-dissociation, and many molecules also become ionised. Solar radiation pressure, acting on the sub-micron sized dust constituents, and the solar wind acting on the ionised constituents, form the gigantic cometary tails which may reach 2×10^8 km in length - larger than the radius of the Earth's orbit.

It is important to define exactly what we mean as a 'comet' or an 'asteroid', as it is beginning to emerge that the boundary between the two distinct types of object is by no means clear:

1. A 'comet' is a body that has been formed in the outer (> 10 AU) regions of the solar system. There exist a number of subsets of cometary bodies:

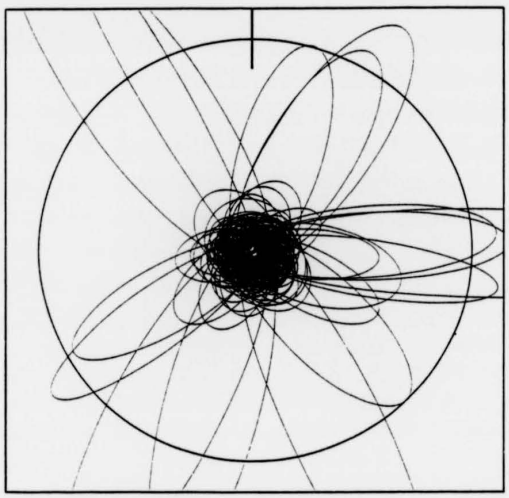

Figure 1.2: The orbits of 136 observed short- and intermediate-period comets have been drawn assuming that these comets all have zero inclination. This is a reasonable assumption for the majority of this group of comets, which has a median inclination to the ecliptic of around 11°. The Sun lies at the centre of the figure and the line at the top indicates the direction of the First Point of Aries. The cometary orbits are orientated such that the angle, First Point of Aries-Sun-perihelion, is the sum of the longitude of the ascending node, Ω, and the argument of perihelion, ω, in the case of inclinations, i, between 0° and 90°. This angle is changed to $(\Omega - \omega)$ for $90° < i < 180°$.
The two circles on the figure have radii of 5.2 and 30.1 AU, representing the orbits of Jupiter and Neptune respectively (the circle of radius 5.2 AU is partially obscured by the Jupiter family cometary orbits).

(i) Active comet - a comet that produces a detectable coma due to gas and dust loss.

(ii) Dormant comet - a comet that has no detectable coma as there is negligible gas and dust loss (due to the volatile ices being shielded from solar radiation by an insulating layer of dust). A dormant comet may have been active in the past and may become active once again in the future. During the dormant phase, the comet may be mistaken for an asteroidal body.

(iii) Extinct comet - a comet that has completely lost its volatile fraction, leaving behind a porous, dusty remnant. An extinct comet may not be reactivated and may essentially take on the resemblance of an asteroidal body.

2. An 'asteroid' is a body that originally formed in the region of the solar system between the orbits of Mars and Jupiter. Successive collisional fragmentation events coupled with gravitational perturbation may remove some of these bodies from their original reservoir into

a variety of orbits, including those that cross the Earth's orbit.

The surface temperature at which the cometary ices begin to sublimate depends on the composition of the volatile fraction. Assuming that water ice controls the sublimation process of most comets, this will begin at a heliocentric distance of around 2.9 AU (where the nucleus surface temperature will have exceeded 170 K). As the comet nucleus continues on its inward orbit the sublimation rate is generally proportional to the incident solar radiation flux, i.e. following an r^{-2} relationship. This means that the comet will be most active close to perihelion (i.e. its closest approach to the Sun, where r is at a minimum) and hence it is here that most of the cometary mass is lost.

The surface dust, that has been loosened by the sublimation of the snows, is pushed away from the nucleus by momentum transfer from the gas molecules (think of leaves in the wind or sand storms). This dust expansion velocity is of the order of 0.6 km s^{-1} and is considered in more detail by Harris et al. (1994) and also in Chapter 4. The larger dust particles ($> 1\mu$m) are not swept away into the tail by the solar radiation pressure but are ejected radially away from the nucleus, generally in the solar direction, onto individual orbits around the Sun. The result is the formation of a meteoroid stream in which many of the meteoroids describe orbits that are quite similar to that of the parent comet. This process is modelled in Chapter 4 for the case of P/Swift-Tuttle, the parent comet of the Perseid meteoroid stream. The heliocentric velocity of P/Swift-Tuttle at perihelion is around 42.2 km s^{-1} (very close to the parabolic limit at that heliocentric distance). It is clear then that dust particles escaping the nucleus surface with cometocentric velocities of the order of 0.6 km s^{-1} would attain heliocentric velocities, V_m, within the range $41.6 \leq V_m \leq 42.8$ km s^{-1}, depending on their direction of emission (i.e. the angle between the direction of particle ejection and the path of the comet's orbit at emission). The semi-major axis of P/Swift-Tuttle is around 26 AU. This narrow range of meteoroid heliocentric velocities is enough to produce a broad quasi-Gaussian distribution of the 'daughter' meteoroid semi-major axes ($6 \leq a_m \leq \infty$ AU) peaking at around 13 AU, although the variation in the other parameters such as perihelion distance, inclination and longitude of ascending node, are more restricted to Gaussian distributions centred on the orbital parameters of the parent comet. As the semi-major axes of many of the ejected meteoroids differ from that of the parent comet, the orbital periods, T, of these meteoroids will also vary (according to $T = a^{\frac{3}{2}}$, where T is in years and the semi-major axis, a, is in AU). Due to these differing orbital periods, the ejected dust particles become quickly distributed around the orbit of the parent comet resulting in a continuous stream of meteoroids. These meteoroids can be in close proximity to each other at perihelion. This is shown, in Chapter 4, to occur in only a few orbital periods of the comet.

During its orbit around the Sun the Earth may pass through one of these dust streams. When this occurs, meteoroids will enter the Earth's upper atmosphere at geocentric velocities between 11 and 72 km s^{-1} (see Chapter 2), depending on the orientation of the collision (i.e. whether the collision is from behind or head-on respectively). The passage of a meteoroid

through the atmosphere causes the surrounding 'air' to become highly excited and ionised due to the friction produced. The result is the formation of a long, thin 'tube' of photoluminescing gas which is referred to as a meteor 'trail' (if visible) and a meteor 'train' if it is not bright enough to be detected with the naked eye (but can be detected by radiowave reflectance methods). The brightness of the meteor depends on the mass of the incident meteoroid and its geocentric velocity (see Chapter 3).

Annually, the Earth passes through around 40 easily detectable meteoroid streams, and the resulting appearance of meteors is referred to as a meteor shower. As the Earth travels through the stream the observed rate of meteors rises steadily over a number of days to a maximum value and then drops away again to negligible numbers as the Earth re-emerges from the stream. The point of maximum meteor activity corresponds to the point of closest approach to the 'centre' of the meteoroid stream, where the meteoroid spatial density is highest. The activity of a meteor shower is determined by its zenithal hour rate (ZHR). The ZHR is defined as the observed hourly rate, at maximum meteor activity, divided by the cosine of the radiant-zenith angle (where the zenith is the point in the sky directly above the observer's head).

Meteoroids enter the Earth's atmosphere from a particular direction, depending on the orientation of the stream with respect to the Earth's orbital plane. Thus, the meteors that belong to a specific shower are observed to emanate from a particular region of the sky. This region is referred to as the radiant. Most meteor showers are named after the star constellation which contains the shower radiant e.g. Perseids and Geminids, or the nearest bright star in the constellation if two or more radiants occupy the same region of the sky (celestial sphere) e.g. δ Aquarids and ι Aquarids. Some of the major meteor showers are listed in Table 2.1 (Chapter 2) along with their ZHRs and probable parent bodies.

Throughout the year there is a near constant influx of meteors that are not associated with any particular meteoroid stream. These meteoroids belong to the sporadic background. The origins of the sporadic background are considered in more detail in Chapter 2, but it can be noted here that the general sporadic background arises from decay and dispersion of meteoroid streams due to processes such as radiation pressure, the Poynting-Robertson effect and collisional fragmentation with other meteoroids in the solar system dust cloud. The ratio of numbers of stream to sporadic meteoroids is also considered in Chapter 2, as is the percentage of sporadic meteoroids that belong to undetected streams.

The Perseids are one of the most famous annual meteor showers. They appear with remarkable consistency of numbers every August, maximising now around August 12/13. As mentioned earlier, their parent comet is P/Swift-Tuttle (1862 III=1992t), and, with the exception of Earth, the causative meteoroids stay clear from perturbing planets. The meteoroids considered in the following work have estimated masses in excess of 0.001 g, so they will be relatively unaffected by stream dispersion processes such as those listed in the previous paragraph. Therefore, of all the known streams, the origin and evolution of the

Perseids should be the easiest to understand.

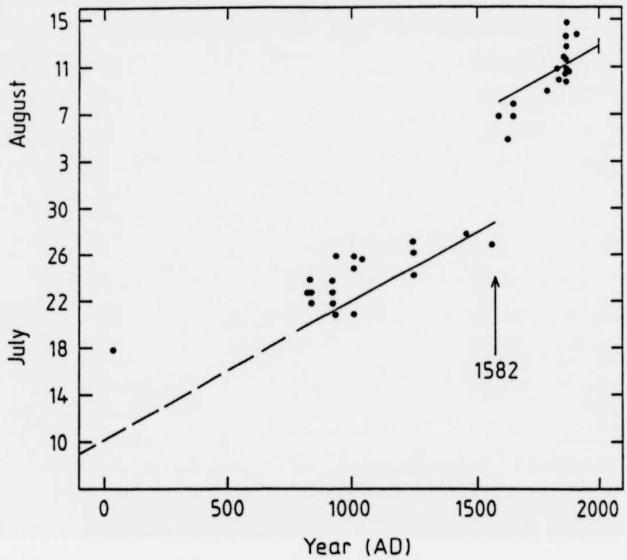

Figure 1.3: The progression of the times of Perseid maximum activity (progression of the descending node)[taken from Hasegawa, 1993]. The straight lines have gradients of 0.01417 days y^{-1} and indicate the progression of the Perseid node with time if gravitational perturbations are ignored.

Meteors that are produced by the influx of an extraterrestrial meteoroid stream should occur every *sidereal* year. With the absence of significant gravitational perturbations and therefore also nodal progression (see Hughes & Emerson, 1982), the Perseids should change their date of maximum activity by 0.01417 days per year (i.e. one day in about 70.6 years). Fig. 1.3 shows the progression of the times of maximum Perseid activity (taken from Hasegawa, 1993). The straight lines on the graph are not fits to the data but are simply lines of gradient 0.01417 days y^{-1}. The gaps in the data between AD. 1042 and 1243 and 1243 and 1451 most probably indicate that people lost interest in recording data in that period and not that the Perseids were absent. The first 'reasonable' record of the Perseids was taken in AD. 830. The AD. 36 record is seven days away from the line and is therefore distinctly suspect.

The Perseid meteor shower maximises at a solar longitude of around 140°, this longitude being reached about August 12/13 in the present epoch. Perseids can be seen between July 23 and August 23 (Cook, 1973). At maximum the meteors have a radiant at Right Ascension 3 hr. 4 min. and declination +58°. For the U.K. the radiant is circum-polar and the local time of transit is 5.7 hours after midnight.

Chapter 2

Meteor showers and meteoroid streams

2.1 Introduction

A meteor, or *shooting star*, is the trail of light observed in the night sky when a small particle of interplanetary matter, known as a meteoroid, enters the Earth's atmosphere and burns up due to the friction produced. The origins and dynamics of meteor showers were poorly understood until the great Leonid storms of 1799 and 1833. The annual occurrence of meteor showers and the periodic occurrence of meteor storms that coincided with the appearance of a comet led astronomers to recognise that these spectacular events might have a cometary origin. In 1861 Daniel Kirkwood suggested (see Kirkwood, 1867),

> May not our periodic meteors be the debris of ancient but now disintegrated comets, whose matter has become distributed around their orbits?

It is now an accepted fact that the meteoroids that cause periodic meteor showers orbit the Sun in meteoroid streams. Random meteor activity throughout the year is caused by the sporadic (or non-stream) population of meteoroids that orbit the Sun. The sporadic component observed from Earth can reach an hourly rate of around 20, depending on the time of day. The mean rate of visual sporadic meteors for an individual observer is 9.7 ± 0.7 hr^{-1} (Hughes, 1974). This sporadic population of meteoroids is observed as a result of three processes:

(i) sporadic meteoroids are stream meteoroids that have had their orbits perturbed so that there is no longer any clear association with a stream ('true sporadics'). Characteristic time-scales are of the order of 10^4 y for stream meteoroid dispersal due to the gravitational influences of the major planets, although this figure does not apply to meteoroids in all streams, e.g. the Perseids. For physical loss due to impacts with zodiacal dust particles (i.e. collisions with sporadic meteoroids in the general solar system dust cloud) the characteristic time scales are of the order of 10^5 y (Olsson-Steel, 1986).

(ii) the Earth may happen to pass through the 'outer edges' of a stream such that the zenithal hourly rate (ZHR) is too low to be identified as a shower, and
(iii) the Earth may pass through the 'centre' of a stream but, due to the stream's paucity of members, the shower remains undetected above the general meteoroid background (i.e. the ZHR is again too low for shower detection).

Throughout the year there are around 40 identifiable meteor showers i.e. the ZHRs are great enough so that the shower is 'noticed' and the meteors are characterised by having similar radiants. Meteoroids that belong to a specific stream all have the same parent comet. A few examples of meteor shower/comet associations are given in Table 2.1, along with the shower ZHR values at maximum activity.

Shower	Date of shower maximum	ZHR_{max}	Parent comet
Quadrantids	Jan 3	140	P/Machholz
η Aquarids	May 3	30	P/Halley
Perseids	Aug 12	70	P/Swift-Tuttle
Orionids	Oct 21	30	P/Halley
Taurids	Nov 3, 13	< 14	P/Encke
Leonids	Nov 17	14000(1883)	P/Tempel-Tuttle
Geminids	Dec 14	70	3200 Phaethon ?

Table 2.1: Some meteor shower/comet associations. Notice how an individual comet can be responsible for more than one meteor shower. e.g. P/Halley, P/Encke. This is probably true of most short-period comets due to their past orbital evolution, or the fact that some cometary meteoroid streams intersect the Earth's orbit at both nodes. The assumed parent body of the Geminid meteoroid stream (3200 Phaethon) is asteroidal in appearance and is a possible candidate for an extinct/dormant cometary nucleus. The ZHRs are taken from Cook, 1973.

A particular comet may be responsible for more than one meteor shower. For example, comet P/Machholz is thought to be the progenitor of the Quadrantids and seven other showers, including the daytime Arietids, δ Aquarids and the Ursids. It is also possible that comet 1491 I is associated with these showers (Williams & Wu, 1993). This may indicate that the complex was formed by the break-up of a single larger parent body. This is also true of the Taurids meteoroid complex which displays up to twelve distinct showers and is thought to be associated with comet P/Encke and ten or more Earth-crossing asteroids.

Most meteoroid streams are named after the region (i.e. constellation) of the sky from where the meteors appear to radiate on the day of maximum shower activity. It is convenient to define the apparent meteor radiant point by right ascension and declination coordinates. The concentration of meteor observations around the radiant is the most direct evidence for shower activity. Fig. 2.1 shows the radiant of the Leonids during the night of 13-14 November 1866.

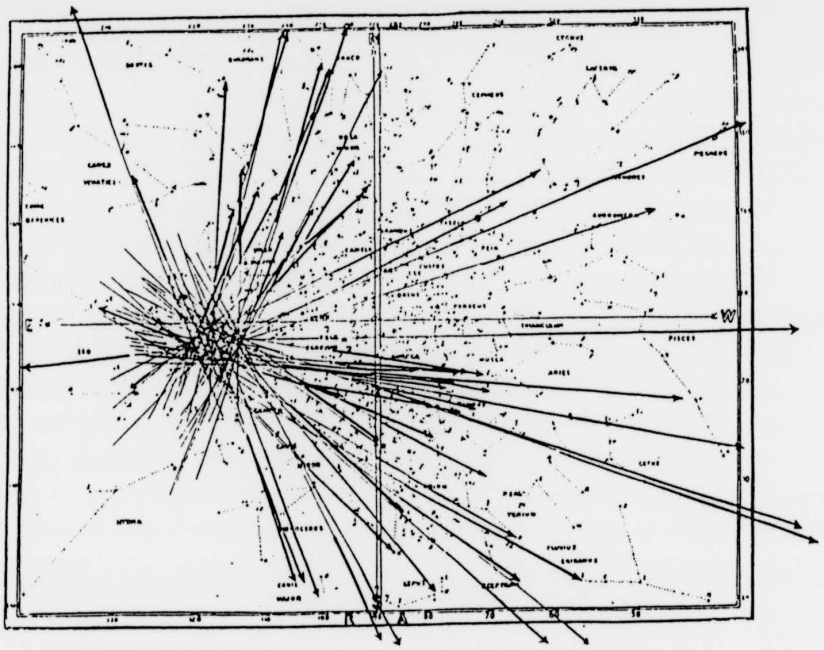

Figure 2.1: Tracks of the meteors seen from Greenwich during the night of 13-14 November 1866 showing the radiant of the Leonids.

A stream meteoroid can only produce an observable meteor if its ascending or descending node intersects with the Earth's orbit. Therefore, in such a case, as the Earth passes through the stream, the ascending or descending nodes of the detected meteoroids must also change and as a result the apparent radiant will move with time. If the other orbital elements remain constant the shift in ascending/descending node causes the radiant point to move more or less parallel to the ecliptic. This daily radiant shift is typically of the order of $+1°$ in right ascension (RA) and $\pm 0.5°$ in declination (dec) (Cook, 1973).

A meteoroid stream is defined as a concentration of particles moving on similar orbits. A particle's orbit size is defined by the heliocentric velocity of the particle at any known point on that orbit. Therefore meteoroids that travel on similar orbits will have similar Earth intersection velocities. The similarity of meteoroid orbits in a particular stream is discussed in this chapter. The sporadic to stream meteoroid ratio is investigated, as is the way in which this ratio varies as a function of meteoroid mass. Finally the physical and orbital characteristics of stream and sporadic meteoroids are compared and the geocentric velocity distribution of cometary meteoroids is modelled.

2.2 Identifying meteoroid streams

A first approximation for meteoroid stream membership involves restricting the acceptable meteor radiant and heliocentric velocity values. It is also possible to identify shower meteors

directly from their calculated orbital elements. A meteoroid orbit is defined by five orbital elements, q, e, i, ω and Ω. Each orbit occupies a point in the corresponding parameter space and the presence of a stream will be seen as a significant concentration of the number of meteoroid orbits around a common point in this space.

2.2.1 The D' criterion

The D' criterion is a measure of the similarity between two orbits (Southworth and Hawkins, 1963; Drummond, 1981). The construction of a four dimensional co-ordinate system based on the differences between specific sets of orbital elements allows a quantative measure of orbital similarity to be performed. The coordinates used to compare two meteoroid orbits are q, e, I and Θ, where I is the angle between the orbital planes and Θ is the difference between the longitudes of perihelion measured from the intersection of the orbits. For a pair of meteoroid orbits labelled 1 and 2 the Drummond D' criterion takes the mathematical form:

$$D' = \left(\frac{e_1 - e_2}{e_1 + e_2}\right)^2 + \left(\frac{q_1 - q_2}{q_1 + q_2}\right)^2 + \left(\frac{I}{180^\circ}\right)^2 + \left(\frac{e_1 + e_2}{2}\frac{\Theta}{180^\circ}\right)^2 \tag{2.1}$$

where

$I = \cos^{-1}[\cos i_1 \cos i_2 + \sin i_1 \sin i_2 \cos(\Omega_1 - \Omega_2)]$

$\Theta = \cos^{-1}[\sin \beta_1 \sin \beta_2 + \cos \beta_1 \cos \beta_2 \cos(\lambda_1 - \lambda_2)]$

The ecliptic latitude, β, and ecliptic longitude, λ, are defined as

$\beta = \sin^{-1}(\sin i \sin \omega)$

$\lambda = \Omega + \tan^{-1}(\cos i \tan \omega)$

180° is added to λ if $\cos \omega < 0$.

The resulting D' ranges from a perfectly matching 0 to a perfectly 'mismatching' 1.8. To identify specific stream members from a data set of meteoroid orbital parameters, an appropriate mean stream orbit must first be chosen. Stream meteoroids may initially be identified 'by eye' using a series of restricted orbital parameter, radiant and heliocentric velocity constraints. An initial mean stream orbit can be chosen in this way. Any meteoroid orbit that lies within a given D' limit, D_0, when compared to the initial mean orbit (i.e. $D' < D_0$), is assumed to be a shower meteor. The meteoroid orbits with $D' < D_0$, according to equation 2.1, are then used to calculate a new mean orbit. When calculating the new mean orbit, each identified stream meteoroid contributes by the weighting factor $(1 - \frac{D'}{D_0})$. The process is then repeated until the same set of meteoroids is selected on two successive loops of the program.

The D' limit, D_0, must be set by the investigator. Southworth and Hawkins (1963) proposed that D_0 should vary inversely with the fourth root of sample size. Lindblad (1971) concluded that the D' limit should be

$$D_0 = 0.80 N^{-\frac{1}{4}} \tag{2.2}$$

where N is the number of meteoroid orbits in the data set. Equation 2.2 results in reasonable agreement with conventional shower classification (i.e. using constrained orbital parameter, heliocentric velocity and radiant point ranges), so this will be adopted for the following analysis.

2.3 Major and minor meteor showers

The Perseid meteor shower dominates the period July 23 to August 23 each year, maximising around August 12/13 (Cook, 1973). During this time period numerous other minor showers and sporadic meteors are also detected. The IAU Photographic Meteor Data Catalogue (see Lindblad, 1987) was found to contain 576 meteors, with calculated meteoroid orbits and estimated meteoroid masses, that occurred between these dates. Fig. 2.2(a) shows the D' distribution for these 576 photographic meteors when compared to the initial mean orbit of the Perseid stream (q = 0.951 AU; e = 0.971; i = 113.1°; ω = 151.0°; Ω = 139.0°.). The prominent peaks correspond to major and minor showers that occur during this time of the year, namely from left to right, (P) the Perseids, (κ) κ Cygnids & o Draconids, (α) α Capricornids, (ι) ι Aquarids and (δ) δ Aquarids. Fig. 2.2(b) displays these meteoroid streams as concentrations of points in an argument of perihelion ω versus inclination i plot. The intervening areas contain those meteoroids that are unresolved into showers. These meteoroids are known as the sporadic background. Fig. 2.2(c) shows a plot of ω versus i for those meteoroids that have a $D' < 0.32$ when compared to the assumed mean orbit of the Perseids. This D' limit was chosen so as to exclude all non-Perseid stream meteoroids from the data set [0.32 lies midway between the Perseid and κ Cygnid D' concentrations in Fig. 2.2(a)].

The boxed area in Fig. 2.2(c) indicates a group of 7 meteoroids corresponding to $0.156 < D' < 0.234$. Their orbital parameters are displayed in Table 2.2. The similarity of their

Meteor	e	q (AU)	ω(deg)	Ω(deg)	i(deg)	α (hours)	δ (deg)
1	0.996	0.999	172.2	142.7	94.4	1.817	+68.56
2	0.923	1.000	166.1	136.6	89.8	1.417	69.5
3	0.942	1.013	177.0	136.5	91.7	0.883	66.26
4	0.912	1.014	182.9	136.0	95.0	0.817	62.8
5	1.011	1.013	182.2	137.7	93.5	0.80	64.86
6	0.945	1.012	178.7	145.3	83.7	0.783	73.3
7	0.841	1.012	185.4	135.8	89.8	0.417	64.3
mean	0.9386	1.009	177.8	138.66	91.13	0.967	67.23

Table 2.2: The above table displays the orbital parameters of the 7 associated meteoroids that are boxed in Fig. 2.2(c). The inference is that these meteors belong to a visually unresolved shower. i.e. the shower is not detected above the general sporadic background due to its paucity of members.

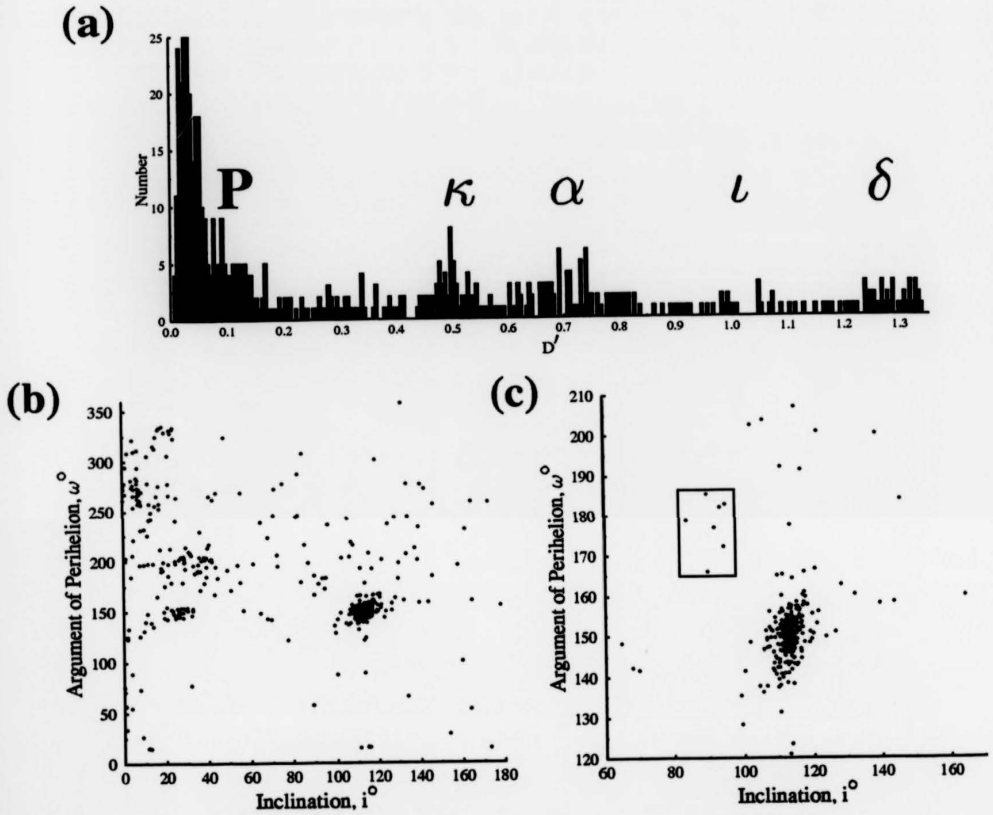

Figure 2.2: The histogram in (a) shows the D' distribution of the 576 photographic meteors when compared to the assumed mean orbit of the Perseid meteor shower ($D' = 0$). Major and minor meteor showers during this time of the year are indicated by the prominent peaks around specific D' values. These showers are, from left to right, the Perseids, κ Cygnids & o Draconids, α Capricornids, ι Aquarids and δ Aquarids. Plot (b) shows how these showers are distributed in ω/i space. The concentrations of points correspond to the observable meteor showers and the intervening points make up the sporadic background. Plot (c) shows the ω/i distribution for those meteor orbits with $D' < 0.32$. The boxed area indicates a group of 7 meteors that have similar orbital parameters and can be thought of as a visually unresolved shower that contributes to the general sporadic background.

orbits suggests that they belong to a visually unresolved shower. The sporadic meteoroid background is thought to contain a significant proportion of these unresolved minor streams.

2.3.1 Calculation of the shower radiant

The corrected geocentric radiant of the shower listed in Table 2.2 can be calculated by following the method described by Porter (1952). The method relies on using trigonometric functions with associated decisions by the investigator about which quadrant the radiant is in. A number of small velocity corrections are ignored or calculated only partially. These simplifications are introduced so as to reduce the calculation effort and the method is quite sufficient for calculating an approximate corrected geocentric radiant.

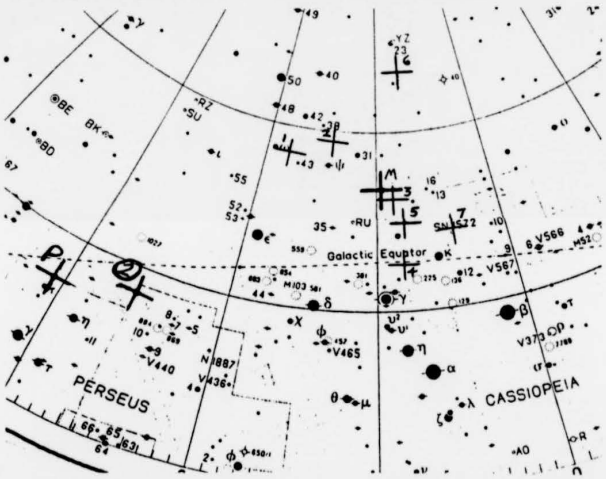

Figure 2.3: The star map shows the area of the celestial sphere containing the constellations Perseus and Cassiopeia. The meteor radiants listed in Table 2.2 are indicated by crosses in the above map and the mean radiant is represented by the bold cross. The position of the mean radiant of the Perseid meteor shower is indicated by the bold cross labelled (P) and the mean radiant of a second visually unresolved shower is indicated by the cross labelled (2).

The resulting radiants are listed in Table 2.2 and indicated by crosses in Fig. 2.3. The mean shower radiant is represented by the bold cross in Fig. 2.3. The Shower is clearly unrelated to the Perseids and appears to originate from the constellation Cassiopeia. Fig. 2.3 also shows the position of the mean radiant of the Perseid shower, (P), and a second visually unresolved shower which is more closely associated with the Perseids, (2). The existence of these background showers illustrates the fact that the sporadic background consists of two components: unresolved shower meteors and 'true sporadics' i.e. those meteoroids whose orbits cannot be associated with any other meteoroid orbits. The true sporadics themselves are likely to have once been members of streams that suffered large orbital perturbations. Thus the 'true sporadic' to stream meteoroid ratio will be less than the sporadic background

to stream meteoroid ratio for the data set. This will now be investigated in more detail.

2.4 The sporadic to stream meteoroid ratio

The sporadic meteor background is now generally thought to contain a significant proportion of resolvable minor streams. Nilsson (1964), using a multistation radar technique capable of determining individual orbits, concluded that at least 25 per cent of sporadic meteors are members of these streams. Similar results have also been obtained by Terentjeva (1967), Kashcheyev & Lebedinets (1967) and Poole & Kaiser (1972). Hughes (1990b) concluded that, on a typical 'non-shower' night, (20 ± 3) per cent of the observed visual meteors belong to minor showers and the remaining percentage are truly sporadic. Davies & Gill (1960), however, used very stringent stream membership criteria in their three station radar experiment and they found a sporadic background shower component of only 3 per cent. It must be stressed that these percentages are meteoroid mass dependent.

2.4.1 The D' Difference

Meteoroids in a particular stream have a narrow range of D' values when compared to the mean stream orbital parameters. If the orbital data used to produce Fig. 2.2(a) is sorted in order of D' it is seen that an individual stream meteoroid in the list has a very similar D' value (i.e. a difference of less than 0.005) to the preceding and following stream meteoroid. Therefore, the difference between the D' values, D_{dif}, of successive meteoroids in the list is an indication of whether the meteoroids are associated with one another. The higher D_{dif} is for a successive pair of meteoroids, the less associated their orbits are.

A plot of number versus D_{dif} for the 576 meteoroids is shown in Fig. 2.4(a). A reasonable and convenient cut-off point for stream association is taken to be $D_{dif} < 0.005$. As a crude first approximation, this indicates that (84 ± 8) per cent of the 576 meteoroids are members of streams, leaving (16 ± 8) per cent that are true sporadic meteoroids.

2.4.2 Undetected stream meteoroids

The 576 meteoroids were sorted into visible showers and a sporadic background component using $D_0 = 0.16$, according to equation 2.2. This was done by comparing the 576 meteoroid orbits with the accepted mean orbital parameters (Cook, 1973) of each of the showers displayed in Fig. 2.2(a) using the stream search method described earlier. The resulting visible showers with corresponding numbers of representative meteoroids are listed in Table 2.3, along with the newly calculated mean orbits for each stream. This analysis leaves a sporadic background of 164 meteors i.e. around 28.5 per cent of the total. This number, however, corresponds to the total sporadic background, including unresolved streams, which explains why it is somewhat higher than the (16 ± 8) per cent quoted earlier for the true

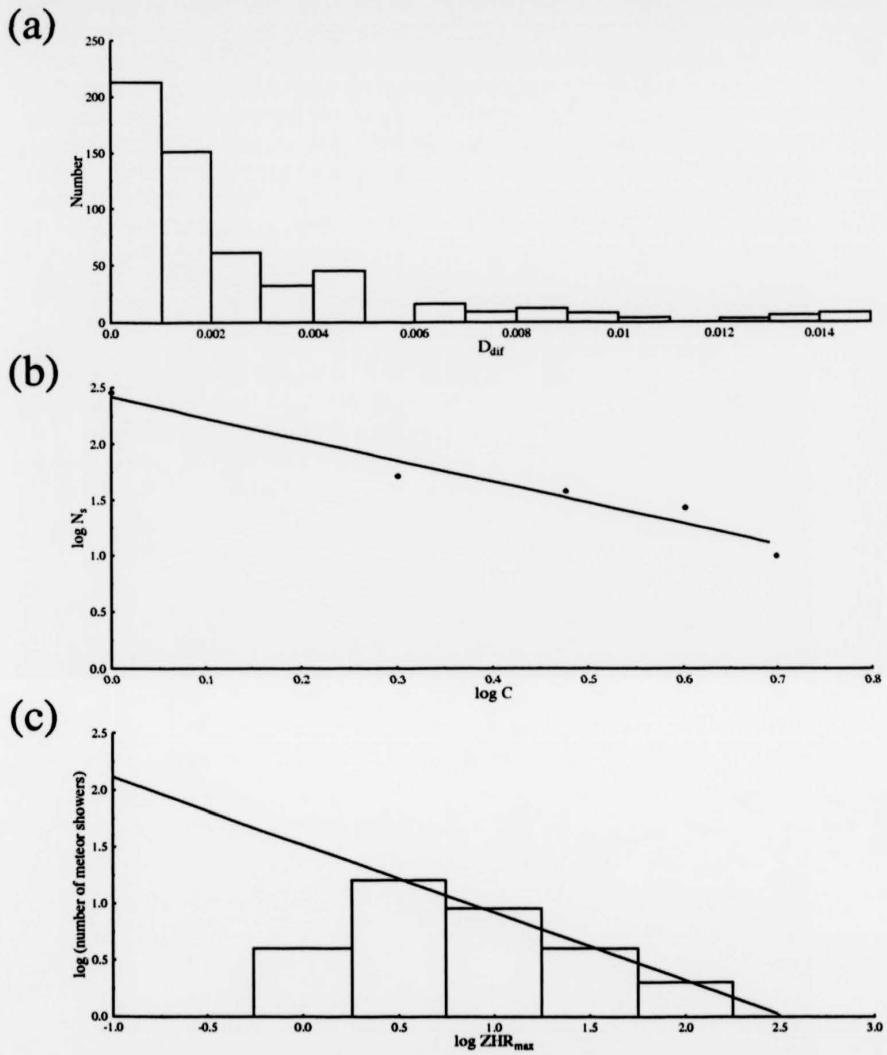

Figure 2.4: The stream to sporadic meteor ratio has been estimated using three different methods. Histogram (a) shows the D_{dif} distribution for the 576 meteors, where D_{dif} is the difference between the D' values of successive meteors in the data set. Low values of D_{dif} (< 0.005) indicate meteoroid stream association. In order to produce plot (b) the 576 meteors were initially sorted into visible showers and sporadic background by applying a D' limit of 0.16 for each of the showers shown in Fig. 2.2(a). Then the number of meteors in each shower, N_s, is plotted against the order of shower representation, C (i.e. the shower with the most members has $C = 1$.). An extrapolation of the straight line in (b) down to $\log N_s = 1$ allows us to estimate the contribution to the sporadic background by underlying stream meteors. Histogram (c) shows the number of annual meteor showers as a function of their maximum zenithal hour rate, ZHR_{max} (adapted from Hughes, 1990b) As the shower ZHR decreases it is more likely to be missed by observers. The straight line represents the estimated numbers of low ZHR showers after allowing for observational selection.

Meteoroid Stream	N_s	C	q(AU)	e	i(deg)	ω	Ω
Perseids	**285**	1	0.949	0.969	113.1	150.8	138.8
κ Cygnids	44		0.986	0.70	30.9	198.5	139.14
o Draconids	+8=**52**	2	0.988	1.003	45.3	197.77	127.8
α Capricornids	**38**	3	0.612	0.763	7.6	260.3	138.5
$S.\delta$ Aquarids	20		0.095	0.966	25.1	147.8	313.8
$N.\delta$ Aquarids	+7=**27**	4	0.066	0.977	20.0	333.1	134.2
$(N+S)\iota$ Aquarids	**10**	5	0.26	0.84	8	260	188

Table 2.3: The 576 meteoroids have been sorted out into their respective streams and the newly calculated mean stream orbital parameters are listed above. N_s is the number of meteoroids in each stream and C is the order of shower representation. This data is used to plot Fig. 2.4(b). A few of the streams have been combined due to their similar orbital parameters and D' values e.g. the κ Cygnids (44 meteoroids) and the o Draconids (8 meteoroids) have been merged into one stream containing 52 meteoroids.

sporadics.

Fig. 2.4(b) is a plot of $\log_{10}N_s$ against $\log_{10}C$ where N_s is the number of meteoroids in the stream and C is the order of shower representation. The shower with the most members is assigned a shower representation, C, of 1. The shower with the second highest number of members has $C = 2$, and so on (see Table 2.3). For the following analysis the κ Cygnids and o Draconids are considered as a single stream due to their similar orbital parameters and consequently similar D' values. This is also the case for the northern and southern δ Aquarids and the northern and southern ι Aquarids. By extrapolating Fig. 2.4(b) we can estimate the fraction of the sporadic background contributed by underlying streams i.e. those with $N_s \geq 1$. It follows that as many as a further 14 underlying showers may exist during this time period, taking a total of (45 ± 5) meteors from the 164 sporadic background meteors. Thus, the analysis has shown that (27 ± 3) per cent of the sporadic background consists of stream meteoroids, a result which agrees favourably with the work of both Nilsson and Hughes.

Consequently, (457 ± 5) of the 576 meteors observed between July 23 to August 23 are stream meteoroids, leaving only (119 ± 5) true sporadics. This corresponds to a true sporadic fraction of around (21 ± 1) per cent which is within the limits of the original estimate of (16 ± 8) per cent.

2.4.3 The over-representation of the Perseids

The meteoroid data set being used is a collection of observations taken by different experimenters, using different instruments that were used for different time periods. The number of camera systems that were running was certainly not constant throughout the July 23 to August 23 period. More are expected to have been active around the time of Perseid shower maximum (August 12/13). The considerable peak in Fig. 2.2(a) corresponding to the

Perseids, raises the question as to whether Perseid meteoroids are over-represented in the data set due to an increase in observational activity around Perseid shower maximum. If this is the case then the gradient of the line in Fig. 2.4(b) would be less negative. On extrapolation of the line down to $N_s = 1$, this would result in an increased number of inferred undetected streams and consequently a decrease in the percentage of true sporadics.

To investigate this suggestion, those meteoroids that were observed between August 11.0 and August 14.0 were extracted from the data set. These dates correspond to the period of maximum Perseid meteor activity and maximum observer activity. The extracted meteoroids numbered 217. These 217 meteoroids were then sorted out into streams and sporadic background using the same D' criterion method as before ($D_0 = 0.16$) and the number of meteoroids in each stream was noted. Then a graph similar to the one shown in Fig. 2.4(b) was plotted in order to estimate the number of undetected stream meteoroids in the sporadic background. The results of this procedure are shown in Table 2.4.

Meteoroid stream	Number of members
Perseids	159
κ Cygnids	6
α Capricornids	3
δ Aquarids	2
Undetected stream meteoroids	(2 ± 1)
True sporadics	(45 ± 1)

Table 2.4: The table shows how the 217 meteors observed between August 11.0 and August 14.0 break down into showers/streams and sporadics.

Around 75% of the 217 meteoroids that were observed between August 11.0-14.0 are Perseids whereas only around 50% of the 576 meteoroids that were observed between July 23-August 23 are Perseids. The true sporadic representation during the August 11.0-14.0 period is found to be around (21 ± 0.5) per cent (for the mass range $0.001 \leq m \leq 152$ g) which agrees favourably with the previous result for the 576 meteoroids that were observed between July 23 and August 23. This result suggests that the numbers of stream meteoroids and true sporadics observed increase at approximately the same rate with increasing observer activity. Therefore the over-representation of the Perseids shouldn't affect the results of section 2.4.2.

2.4.4 Statistical evidence

Fig. 2.4(c) shows a histogram of the number of meteor showers active each year as a function of their maximum zenithal hour rate, ZHR_{max}, plotted on logarithmic scales (adapted from Hughes, 1990). As the ZHR decreases the shower is more likely to be missed by observers, so the drop-off in numbers of showers with $\log ZHR_{max} < 1.0$ is purely an observational selection

error. The straight line extrapolation represents the estimated numbers of low ZHR showers after allowing for observational selection. The straight line has a gradient of (0.614 ± 0.03). This means that, in the July 23 to August 23 period, if there is 1 shower with a ZHR between 100 and 1000 then there are $10^{0.614} = 4.11$ showers with $10 < ZHR < 100$, $4.11^2 = 16.9$ with $1 < ZHR < 10$ and $4.11^3 = 69.4$ with $0.1 < ZHR < 1$. As the mean values for these ZHR ranges are approximately 300, 30, 3 and 0.3 respectively and if we assume that these mean values correspond to the total number of meteors observed then this results in a total of (495 ± 22) stream meteoroids from a total of 576 meteors. This crude statistical analysis leaves a true sporadic component of (81 ± 22) meteoroids which corresponds to (14 ± 4) per cent of the total. This is within the original true sporadic component estimate of (16 ± 8) per cent.

Taking the three true sporadic percentage estimation methods into account, we come to the conclusion that the mean true sporadic component is represented by (17 ± 4) per cent of the total photographic meteoroid influx.

2.4.5 Variation of the sporadic to stream ratio with meteoroid mass

True sporadic meteoroids are those stream meteoroids that have had their orbits changed to such an extent that they can no longer be associated with any stream. Likely origins for these orbit perturbations include (a) the collisional fragmentation of meteoroids within a stream, either with members of the stream itself or with meteoroids in the general zodiacal dust cloud, (b) the Poynting-Robertson (PR) effect, a radiation phenomenon that selectively reduces the eccentricities and semi-major axes of small particles and (c) the gravitational perturbation of meteoroid orbits by the major planets.

Only high velocity collisional fragmentation is capable of producing true sporadic meteoroids. According to Hughes (1993), an impactor of mass i capable of producing a crater of, say, 0.4 the diameter of the primary (mass m) will cause fragmentation. For a collision at 20 km s^{-1} this requires $\frac{i}{m} > 0.00002$. If this ratio is only just exceeded the fragments are given a velocity which is only just in excess of the escape velocity from the primary body. As a result the fragments will have orbits that differ only slightly from that of the primary and the effect will be to slightly broaden the meteoroid stream. The ejecta will still be recognised as stream meteoroids. For high velocity fragmentation to occur, $\frac{i}{m}$ must be much greater than 0.00002. In this case, the fragments are scattered throughout the inner solar system as true sporadic meteoroids. Thus high velocity fragmentation has the effect of producing a population of low mass, low diameter sporadic particles. A typical 0.1 g stream meteoroid will be broken up to form around ten thousand true sporadics with randomly orientated orbits. The only non-random aspect of the collision fragments is that their orbits will continue to pass through the point in space where the collision took place. This feature will itself soon disappear due to other orbital perturbation mechanisms. However, the mass distribution

of cometary meteoroids is such that the number of low mass meteoroids vastly exceeds the number of high mass meteoroids (the relative number of cometary meteoroids decreases by a factor of 10 for every decade of mass increase). This means that high velocity fragmentation is less common than low velocity fragmentation (which in turn is less common than erosive collisions). So the dominant result of inter-meteoroid collisions is to steadily broaden the streams.

Gravitational perturbations and the PR effect change the orbits of stream meteoroids without changing the meteoroids' physical form. The PR effect, however, selectively changes the orbits of meteoroids at the lower end of the size spectrum. The scattering and reflection of solar radiation will cause an orbiting body to eventually spiral into the Sun. An expression for the time t (s) taken for a perfectly absorbing body of diameter D (cm) and density ρ (g cm^{-3}) to spiral in from a circular orbit of radius r_1 to one of radius r_2 (cm) is

$$t = \frac{4\pi c^2 D_\rho}{6L_0}(r_1^2 - r_2^2) \quad , \tag{2.3}$$

where c is the velocity of light ($\simeq 3 \times 10^{10}$ cm s^{-1}) and L_0 is the luminosity of the Sun ($\simeq 3.9 \times 10^{33}$ erg s^{-1}). This is known as the PR lifetime. Hence, the PR effect selectively changes the orbits of low diameter, low mass (say $m < 0.1$ g) meteoroids to a greater extent and on a shorter timescale than higher ($m > 0.1$ g) mass ones.

As a result of high velocity fragmentation and the PR effect, the true sporadic component is expected to be concentrated in the lower mass population of photographic meteors. Therefore, as we sample higher and higher mass meteoroids, the sporadic to stream ratio is expected to decrease.

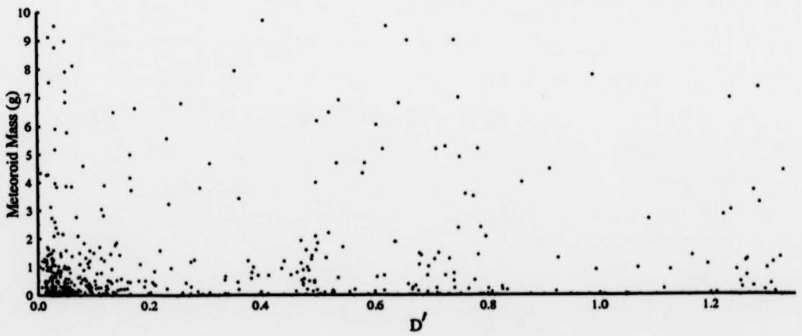

Figure 2.5: Estimated meteoroid mass (up to 10 g) has been plotted against meteoroid orbital D' value for the meteoroids that were observed between July 23 to August 23. The higher the D' value, the less 'Perseid-like' the meteor orbit is. Visible showers can be seen as concentrations of high mass ($m > 1$ g) meteoroids around specific D' values.

Fig. 2.5 shows a plot of estimated meteoroid mass (up to 10 g) versus meteoroid orbit

D' for the meteoroids observed between July 23 and August 23 when compared to the mean orbit of the Perseids. The showers can be identified as concentrations of high mass ($m > 1$ g) meteoroids around specific D' values. By dividing this data up into mass groups containing equal numbers of particles we can investigate the relationship between true sporadic to stream ratio and meteoroid mass.

The data is split into 4 mass bins each containing 144 meteoroids. The bins cover the mass ranges $2.17 \leq m \leq 1000$ g, $0.55 \leq m \leq 2.1$ g, $0.115 \leq m \leq 0.545$ g and $0.00036 \leq m \leq 0.112$ g respectively and the mean meteoroid mass for each bin is 116.86, 1.12, 0.305 and 0.037 g respectively.

The next step is to sort the 144 meteoroids in each bin into either Perseids, κ Cygnids, o Draconids, α Capricornids, Northern ι Aquarids, Southern ι Aquarids, Northern δ Aquarids, Southern δ Aquarids, undetected stream meteoroids and true sporadics. This is done by comparing the 144 meteors in each bin with the mean stream orbital parameters listed in Table 2.3 (section 2.4.2) using $D_0 = 0.16$ and the stream search method described earlier.

For the meteoroid bins with mean masses 0.037 g, 0.305 g and 1.118 g the true sporadic to stream ratios are found to be 0.29, 0.18 and 0.14 respectively. The results of the analysis show that as the mean meteoroid mass begins to increase the true sporadic to stream ratio does indeed steadily decrease. However, when we reach the final mass bin corresponding to $2.17 \leq m \leq 1000$ g ($\overline{m} = 116.86$ g) there is a sudden unexpected rise in the ratio to 0.25. Thus, the true sporadic to stream meteoroid ratio does not seem to vary systematically with meteoroid mass in the data set I have evaluated. The increase in the ratio for meteoroids with $2.17 \leq m \leq 1000$ g cannot be due to increased high velocity collisional fragmentation or a more marked PR effect as we are dealing with the larger end of the meteoroid size spectrum ($\overline{m} = 116.86$ g).

The explanation could lie with the fact that the progenitors of many high mass ($m >$ 100 g) meteoroids are known to be in a variety of subjovian Earth-crossing orbits similar to those of many Apollo-Amor asteroids. Although some proportion of the Apollo-Amor asteroids may originate from the asteroid belt (Wetherill, 1974), many of them are probably cometary disintegration products (see, for example, Wasson & Wetherill, 1979). Thus, the meteoroid streams distributed around the orbits of short-period comets may be accompanied by as many meteoroid streams distributed around orbits of Apollo-Amor asteroids. Therefore, a proportion of the high mass meteoroids ($m > 2.17$ g) that have been identified as true sporadics could in reality be members of unidentified asteroidal meteoroid streams.

2.5 The physical and orbital characteristics of stream and sporadic meteors

A search through the IAU Photographic Meteor Data Catalogue (Lindblad, 1991) yielded 1827 meteoroids whose orbits had been calculated, 999 of which were listed as stream meteoroids and 828 as sporadics (the term 'sporadic' here refers to the general sporadic background which includes undetected meteoroid streams). Fig. 2.6 shows the distribution of these meteors as a function of date of observation for (a) the 999 stream meteoroids and (b) the 828 sporadics. The three prominent peaks in the stream influx are dominated by, from the left, the Quadrantid, the Perseid and the Geminid meteor showers, occurring in early January, mid August and mid December respectively. It is likely that these three peaks, especially for the case of the Perseids, are over-represented due to increased observer activity at these times of the year (the numbers of Perseids observed during shower maximum [Aug. 12/13] accounts for around 6.5% of the total catalogue stream meteoroid recordings). The increase in stream meteoroid activity around October and November is mainly due to the combined presence of the Taurid, Orionid and Leonid meteor showers. Plot (b) shows that the sporadic component influx is relatively constant throughout the year with increases in sporadic activity being contemporaneous with Perseid and Geminid shower activity. This is explained by the increase in observer activity during these periods. The gaps in the stream meteor influx (e.g. mid-July) correspond to periods of sparse meteor shower activity where those meteors detected are largely of sporadic origin.

Fig. 2.6(c) shows a comparison between the absolute visual magnitudes of stream and sporadic meteors. The white bars represent the percentage of the recorded stream meteors in each 0.5 magnitude bin whereas the black bars represent the relative percentages of sporadics. The mean magnitudes for the observed stream and sporadic meteors are -1.17 and -0.786 respectively. The standard deviation of the magnitude data about these mean values is ± 2.49 and ± 2.23 respectively. This suggests that, in general, stream meteoroids contain a higher proportion of massive particles than the sporadic background. The most probable magnitude seen is between +1.0 and +1.5. The sporadic contribution is clearly more prevalent for those meteors with magnitudes greater i.e. fainter than -1.5.

Fig. 2.7 shows a plot of $\log N$ versus absolute visual magnitude, M, where N is the cumulative number of observed meteors less bright than magnitude M. The linear part of the curve (i.e. $M < -4$) corresponds to the meteor magnitude range that is comfortably detected by photographic techniques. For meteor magnitudes greater (i.e. less bright) than around -4 the curve begins to deviate from linearity, the deviation becoming more pronounced as the meteor magnitude increases. This indicates that meteors are starting to be missed by observers due to their increased difficulty of detection on the photographic plate. This increase in difficulty can be due to decreasing meteoroid mass and decreasing meteoroid geocentric velocities, both of which lead to fainter ionisation trails.

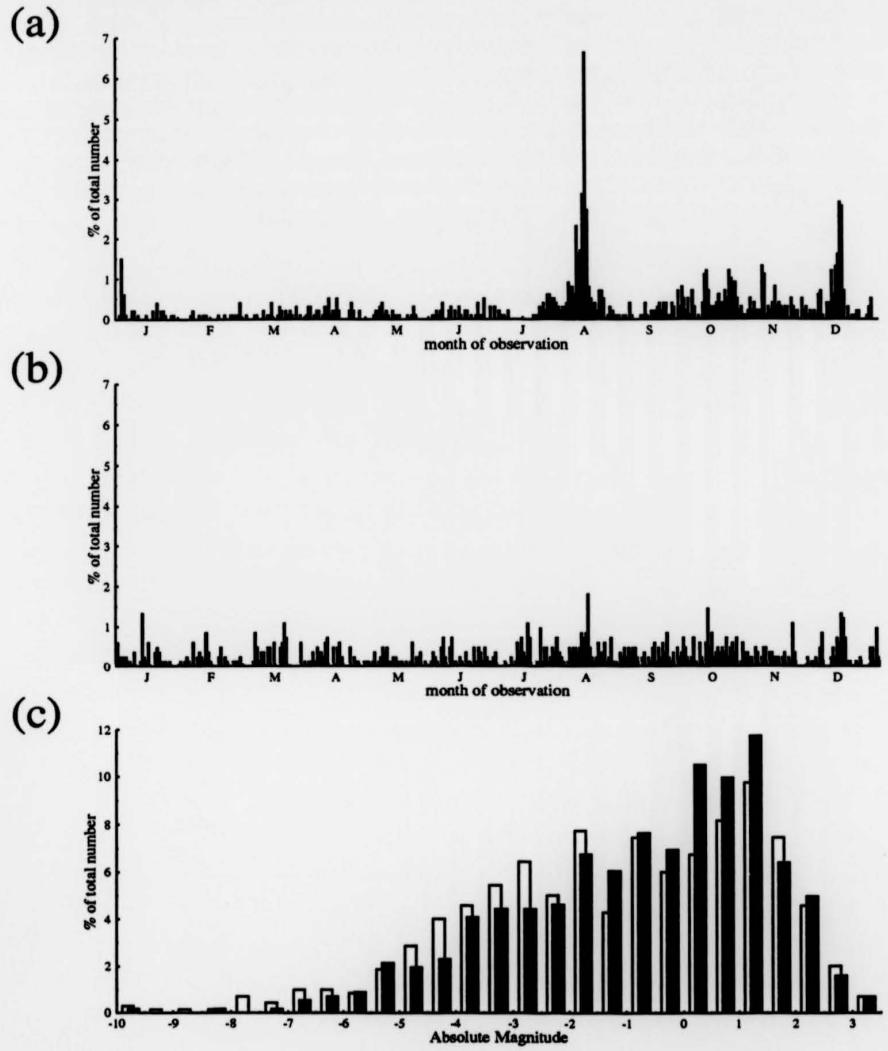

Figure 2.6: Plot (a) shows the influx of stream meteoroids as a function of date of observation. 999 stream meteoroids were identified from the IAU Photographic Meteor Data Catalogue. The annual stream meteoroid influx is dominated by the Quadrantids, the Perseids and the Geminids, occurring during January, August and December respectively. Plot (b) shows the influx of sporadic meteors as a function of date of observation. The data set contains 828 meteors and the influx is relatively constant throughout the year. Plot (c) shows a comparison between the absolute visual magnitudes of the meteors represented in plots (a) and (b). The white and black bars represent the relative percentages of stream and sporadic meteoroids respectively. The mean magnitudes for observed stream and sporadic meteoroids are -1.17 and -0.786 respectively.

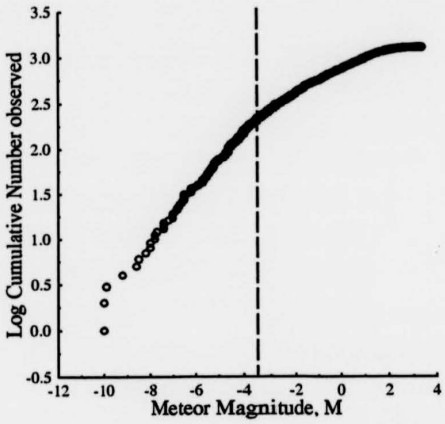

Figure 2.7: The cumulative number of observed photographic meteors (stream and sporadic) less bright than magnitude M. The curve begins to deviate from linearity at a meteor magnitude of around -4. A proportion of meteors with magnitudes greater (i.e. less bright) than this are missed by observers due to their less obvious ionisation trails.

Photographic meteors are detected by systems such as the Baker Super-Schmidt meteor camera. This has a very wide aperture (an f-number of 0.8) and a circular field of view 55° in diameter. Using high-speed film it can photograph down to fourth magnitude meteors (Whipple, 1949; Jachia and Whipple, 1956). The magnitude cut-off point in Figs. 2.7 and 2.6(c) is +3.5. There are obviously a vast number of meteors with magnitudes greater than -4 that have not been detected by observers scanning the photographic plates. This number will increase as the meteor magnitude increases. The observed mean magnitudes quoted above are therefore not a true reflection of the incident meteor magnitude distribution.

An investigation of the estimated masses, m, of the 1827 meteoroids reveals that around 44% of the stream meteoroids have $m < 0.1$ g whereas the corresponding number for the sporadic meteoroids is nearly 60%. The median estimated masses for the stream and sporadic meteors are 0.147 g and 0.0462 g respectively. This concurs with the sporadics' increased representation at above zero magnitudes. Again, these median mass values are not a true reflection of the incident meteoroid mass distribution as meteor trail brightness is a function of meteoroid mass. Therefore, observers will preferentially detect higher mass meteors.

A comparison between the orbital parameters $\frac{1}{a}$, e, q and i are shown in Figs. 2.8 and 2.9 for stream meteoroids (white bars), sporadic meteoroids (black bars) and the known short-period comets (right-hand plots, white bars) with $q < 1.1$ AU (i.e. those which could potentially produce Earth-intersecting meteoroids). The mean $\frac{1}{a}$ values for stream and sporadic meteoroids are 0.35 AU^{-1} and 0.288 AU^{-1} respectively, whereas the corresponding value for the short-period comets is 0.202 AU^{-1}. The standard deviations around these

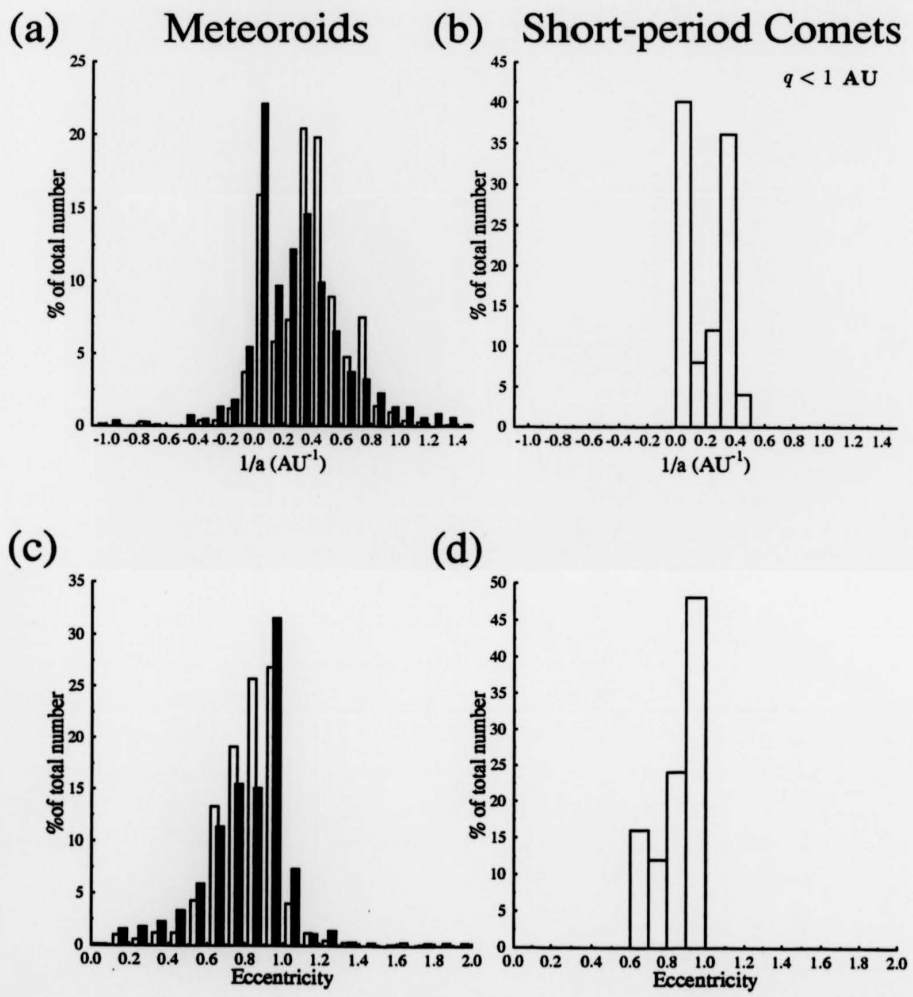

Figure 2.8: Histogram (a) shows a comparison between the distribution of reciprocal semi-major axis, $1/a$, for stream meteoroids (white bars) and sporadic meteoroids (black bars). Histogram (b) shows the corresponding $1/a$ distribution for the short-period comets with perihelia less than 1.1 AU. Histogram (c) compares the orbital eccentricity distribution of stream and sporadic meteoroids, and histogram (d) shows the orbital eccentricity distribution of the short-period comets with perihelia less than 1.1 AU.

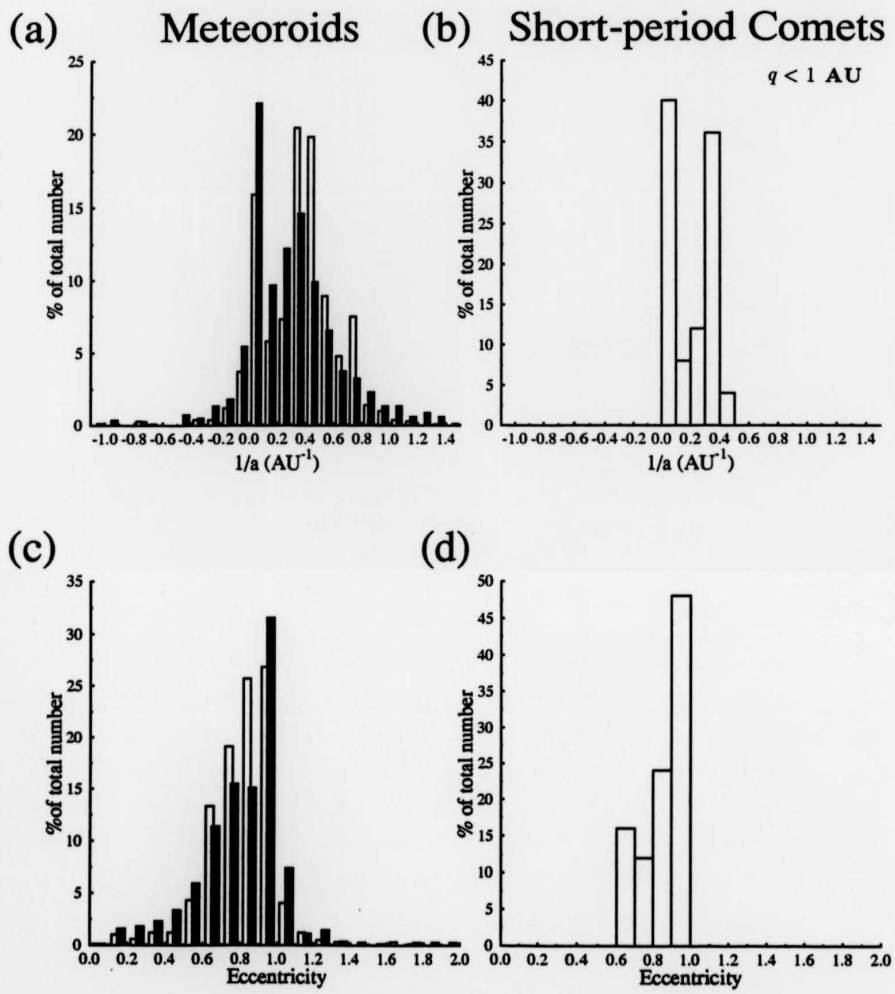

Figure 2.8: Histogram (a) shows a comparison between the distribution of reciprocal semi-major axis, $1/a$, for stream meteoroids (white bars) and sporadic meteoroids (black bars). Histogram (b) shows the corresponding $1/a$ distribution for the short-period comets with perihelia less than 1.1 AU. Histogram (c) compares the orbital eccentricity distribution of stream and sporadic meteoroids, and histogram (d) shows the orbital eccentricity distribution of the short-period comets with perihelia less than 1.1 AU.

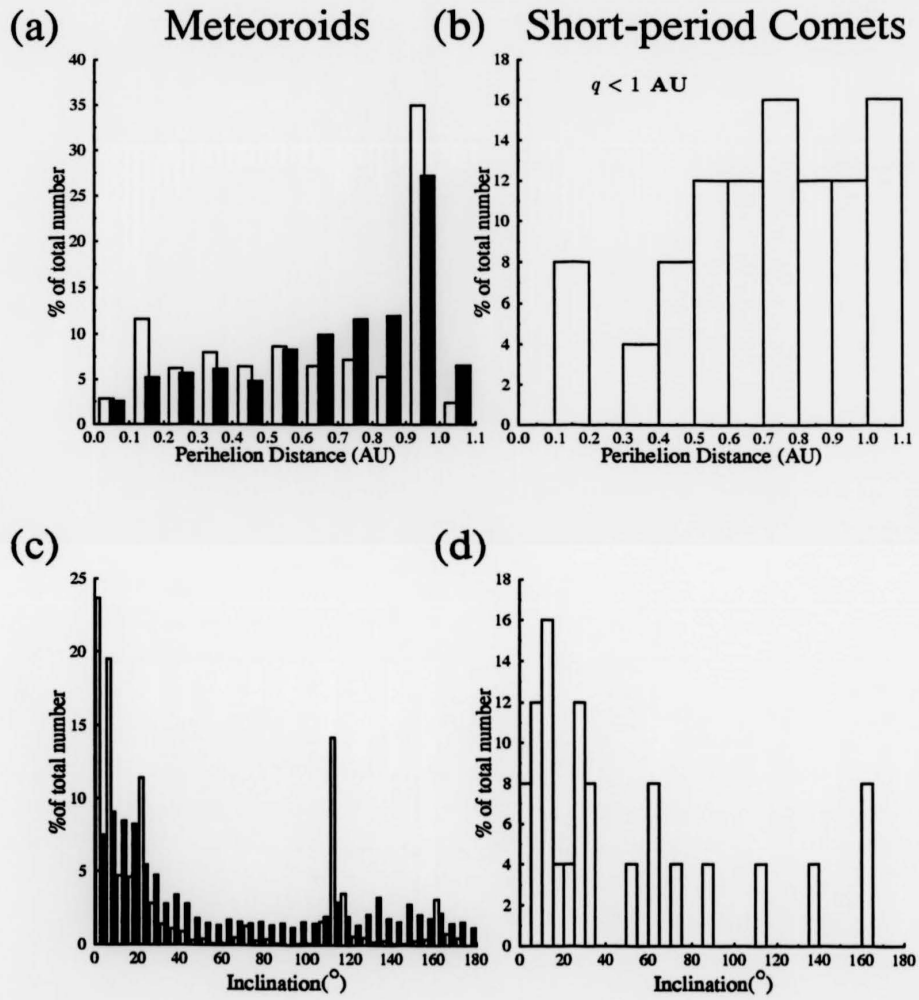

Figure 2.9: Histogram (a) shows a comparison between the distribution of orbital perihelion distance, q, for stream meteoroids (white bars) and sporadic meteoroids (black bars). Histogram (b) shows the corresponding q distribution for the short-period comets with perihelia less than 1.1 AU. Histogram (c) compares the orbital inclination distribution of stream and sporadic meteoroids, and histogram (d) shows the orbital inclination distribution of the short-period comets with perihelia less than 1.1 AU.

mean values are ± 0.275, ± 0.343 and ± 0.139 AU^{-1} respectively. One can see that the meteoroid $\frac{1}{a}$ distribution resembles the short-period comet $\frac{1}{a}$ distribution for $0.0 < \frac{1}{a} < 0.4$ (i.e. $a > 2.5$ AU). The short-period comets with $\frac{1}{a} > 0.4$ that produced the corresponding meteoroids are obviously absent, except for the solitary comet P/Encke at $\frac{1}{a} = 0.45$ AU^{-1} ($a = 2.22$ AU). Three possible explanations for this are

(i) the low semi-major axis, low period (< 4 years) comets have long since decayed completely, leaving the meteoroids behind in their place.

(ii) the meteoroids did not originally describe these orbits but have suffered orbit change over history due to gravitational perturbations and the PR effect.

(iii) the meteoroid progenitors do exist on these low period orbits but have not been discovered or identified. It is possible that many Apollo-Amor-Aten type objects, whether they are asteroidal or cometary, could be the parent bodies of meteoroid streams.

The short-period comet eccentricity distribution has a cut-off point at $e = 0.6$. The reason for this is the same as that for the $\frac{1}{a}$ distribution in that the low semi-major axis, low eccentricity comets are assumed to be absent. Over many thousands of orbital periods, the PR effect has progressively lowered the meteoroid orbital eccentricities and semi-major axes. This explains the increased representation of sporadic meteoroids with $e < 0.6$ and $a < 1.25$ AU ($\frac{1}{a} > 0.8$ AU^{-1}). The mean eccentricity values are 0.82 and 0.817 for stream and sporadic meteoroids respectively and the value for the short-period comets is 0.857. The standard deviations around these mean values are ± 0.197, ± 0.241 and ± 0.113 respectively.

As expected due to observational selection the majority of detected meteoroids have perihelia around 1 AU. The remaining distribution is relatively flat. This should also be the case for the short-period comets but it is not hard to understand why there is a deficit of comets with $q < 0.5$ AU; the closer a comet nucleus approaches the Sun the more active it will become and hence the shorter its orbital life. Therefore at any time there will always be fewer short-period comets with low perihelion distances. The mean stream and sporadic perihelion distances are 0.638 AU and 0.696 AU and the mean short-period comet perihelion distance is 0.713 AU. The standard deviations around these mean values are ± 0.316, ± 0.28 and ± 0.262 AU respectively.

The stream meteoroid inclination distribution closely resembles that of the short-period comets. The majority of stream meteoroids lie close to the ecliptic plane and the peaks in the distribution at $i = 24°$ and $i = 114°$ correspond to Geminid and Perseid meteoroids respectively. The sporadic component profile gives us a clue as to its stream meteoroid origins. The mean inclination values are 43.1° for stream meteoroids, 64.3° for sporadic meteoroids and 47.3° for short-period comets. The standard deviations around these mean values are $\pm 51.4°$, $\pm 55.9°$ and $\pm 49.2°$ respectively.

2.6 The velocity distribution of meteoroids in the inner solar system

The majority of large interplanetary dust particles (mass greater than 10^{-6} g) are concentrated in meteoroid streams (Whipple, 1967 and Hughes, 1975) and these stream meteoroids have orbital parameters that are still very similar to those of the parent comets. This means that meteoroids with similar orbits will produce meteors with similar geocentric velocities and therefore each meteor shower has a characteristic range of meteor velocities. The observed corrected geocentric velocity (V_C) distributions (velocity data from the IAU Photographic Meteor Data Catalogue) shown in Fig. 2.10 are the result of the accumulation of these velocities for many streams. Fig. 2.10(a) shows a comparison between the velocity distributions of photographic stream (clear bars) and sporadic (black bars) meteors from the IAU Meteor Data Catalogue and Fig. 2.10(b) shows the combined photographic meteor distribution. The lower limit of the velocity distributions are given by the free-fall velocity of a particle hitting the Earth which started out with zero geocentric velocity at infinity. This is also equal to the Earth's escape velocity, V_{esc}, which is approximately 11.2 km s^{-1}. The upper limit of 72 km s^{-1} is obtained by the vector summation of the maximum meteoroid heliocentric velocity at 1 AU from the Sun (this is approximately 42 km s^{-1}, assuming that the meteoroid is a member of the Solar System) with the Earth's mean heliocentric velocity (30 km s^{-1}). The small percentage of meteors having observed velocities greater than 72 km s^{-1} may be due to three possible causes:

(i) errors in the velocity determination,

(ii) interparticle collisions causing the acceleration of meteoroid velocities above the parabolic limit, and

(iii) the existence of true hyperbolic meteoroids (i.e. meteoroids that have a velocity greater than the solar escape velocity at the Earth's radius). These particles are inter-stellar in origin. It is likely that all three causes contribute meteoroids to the hyperbolic flux.

The photographic meteors have a 'double-humped' velocity distribution with the main peak occurring at around 25 km s^{-1} and a secondary peak at around 63 km s^{-1} caused by the relatively high geocentric velocities associated with retrograde meteoroid orbits. The mean geocentric velocities are 37.5 km s^{-1}, 41.5 km s^{-1} and 39.3 km s^{-1} for stream meteoroids, sporadic meteoroids and the total population respectively. McKinley (1967) quotes a mean visual meteor geocentric velocity, V_g, of 35.6 km s^{-1}. Fig. 2.10(c) shows the velocity distribution for faint radio meteors for comparison ($\overline{m} \sim 8^m.2$) observed at Havanna, Illinois (Verniani, 1973). The faint radio meteors have a single maximum at around 32 km s^{-1}.

We can model the meteoroid velocity distribution by using the 136 short-period comets listed in Marsden (1986) to create a general distribution of comets and hence meteoroids. The cometary meteoroids in the inner Solar System are modelled by placing computer generated meteoroids on and around the orbits of these 136 short-period comets, thus

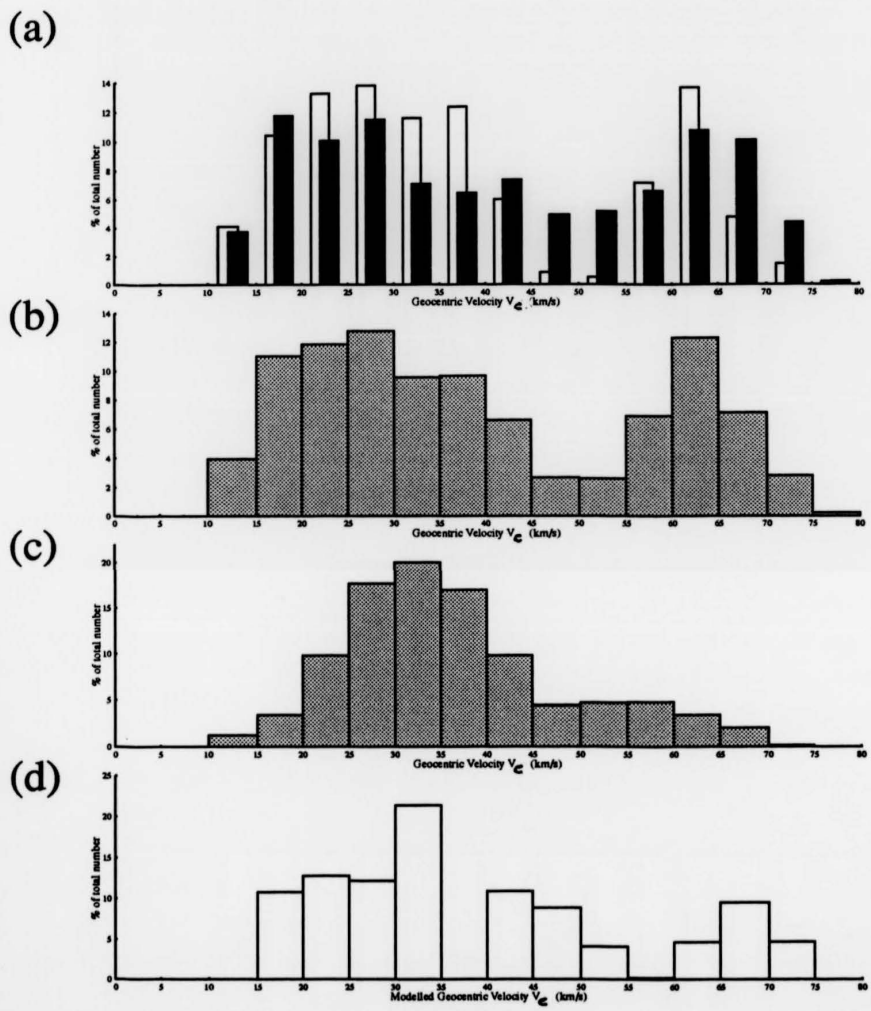

Figure 2.10: Histogram (a) shows a comparison between the observed geocentric velocity distributions for stream meteors (white bars) and sporadic meteors (black bars). The velocities are in km s^{-1}. Histogram (b) shows the combined velocity distribution and histogram (c) shows the observed velocity distribution for faint radio meteors. Histogram (d) shows the result of modelling the observed velocity distribution by placing computer generated meteoroids around the orbits of the 136 known short period comets.

producing 136 meteoroid streams (see McBride & Hughes, 1990a). Three real meteoroid streams, the Quadrantids, the Taurids and the Perseids are investigated to assess how their orbital parameters vary. A 'typical' meteoroid stream is then modelled such that it will vary in a similar fashion to the average observed parameter spreads of the real streams. The orbital parameters modelled are the semi-major axis and the inclination. It is not necessary to model the longitude of the ascending node, Ω, as this does not affect the Earth-meteoroid intersection velocities as long as the planetary orbit is assumed to be circular. The stream perihelion distance distribution is also ignored. As a result the parent cometary orbit is given an 'anchor point' at perihelion where most meteoroid emission occurs. If a cometary orbit had a semi-major axis a_c AU then the modelled meteoroids were given sixteen orbital semi-major axes of $0.5a_c$, $0.6a_c, \ldots, 2.0a_c$ AU respectively and each was given a weighting factor derived from the 'typical' stream orbital parameter profiles. Nine weighted inclinations were also introduced for each stream ranging from -4° to +4° giving a total number of modelled meteoroids in each stream of 16×9 = 144.

The particles placed around the cometary orbits are identical, i.e. of equal mass. This means that all 136 comet-streams are assumed to have identical masses, an assumption that is incorrect in reality. The relationship between the mass of a parent comet and the mass of its meteoroid stream has been investigated by Hughes (1985). Hughes assumed that the comet nucleus lost on average a constant thickness of material at each perihelion passage. (In reality the majority of mass loss will be restricted to active areas on the nucleus surface. However, the positions of these active areas will probably change with time resulting in the erosion of the whole nucleus surface). The nucleus radius can be thought of as decreasing linearly as a function of the time spent in the inner solar system. This decay process results in the mass of a meteoroid stream increasing quickly at first and hence the mass of a meteoroid stream depends on the original size and the 'age' of the parent comet. It is considered valid, however, to consider an equal mass comet-stream model in order to gain an insight into the general time averaged meteoroid geocentric velocity distribution.

A further question that must be considered is whether the 136 short-period comets is a truly representative data set. It is almost certain that the 136 short-period comets is not the *whole* data set. Stream-producing comets may decay, disintegrate or become generally inactive or dormant. Comets are only detected if they are bright enough to be observed from Earth. Therefore the 136 short-period comets are just a data set containing the brightest short-period comets. There must be many small and/or inactive comets that go unnoticed. To gain an insight into the size distribution of the short-period comets we must calculate a parameter known as the mass distribution index. A mass distribution index, s, is used to characterise a distribution of particles over a specific mass range (see Chapter 5). Hughes (1990a) concluded that the mass distribution index for comets is (1.57 ± 0.003). This means that the large majority of the total mass of cometary material is concentrated in the few largest comets. This also means that the contribution by mass to the cometary meteoroid

dust cloud in the inner solar system is likely to be dominated by the few largest meteoroid streams. Therefore, the contribution to the stream meteoroid population from low mass comets is negligible.

The long period comet population has been ignored in the following analysis as it is also considered to have a negligible contribution to the inner solar system meteoroid dust cloud due to their infrequent perihelion passages.

2.6.1 The meteoroid-Earth intersection velocity

Given any point on a meteoroid orbit defined by the heliocentric distance, r, and the true anomaly, θ, it is possible to express its position in terms of Cartesian coordinates x, y, z by

$$x = r\,(\cos\Omega\cos(\omega+\theta) - \sin\Omega\sin(\omega+\theta)\cos i) \tag{2.4}$$

$$y = r\,(\sin\Omega\cos(\omega+\theta) + \cos\Omega\sin(\omega+\theta)\cos i) \tag{2.5}$$

$$z = r\,(\sin(\omega+\theta)\sin i) \tag{2.6}$$

where Ω, ω and i are the longitude of the ascending node, the argument of perihelion and the orbital inclination respectively.

If a meteoroid orbit has a perihelion distance, q, less than or equal to the mean heliocentric distance of the planet in question (1.000 AU for Earth) and an aphelion distance, Q, that is greater than 1.000 AU, then an intersection of orbits may occur. In such a case $(\omega+\theta)$ is zero (or 180°). i.e.

$$|\cos(\omega+\theta)| = 1 \qquad \sin(\omega+\theta) = 0 \tag{2.7}$$

This means that $(\omega+\theta)$ is automatically known for the co-ordinate calculations in equations 2.4, 2.5 and 2.6. We can *force* each of our modelled meteoroids to intersect the Earth's orbit by assuming the equalities in equation 2.7. In essence we are rotating each meteoroid orbit in its own plane until an intersection occurs. This is equivalent to increasing or decreasing the meteoroid's orbital argument of perihelion, ω. There is an astronomical justification for this procedure. Although certain meteor showers are observed in the present epoch, this does not mean that they were seen from Earth in the past, or that they will be seen in the future. Secular planetary perturbations may cause some meteoroid streams to precess in argument of perihelion and longitude of ascending node. As a result the positions of the ascending and descending nodes in the ecliptic plane will move with time. Thus, a stream which presently has its nodes some way away from 1 AU, so that no shower occurs on Earth, may eventually become visible to Earth observers due to orbital precession. For example, the Geminids have only been observed since the middle of the last century (Fox et al., 1982).

The angle of collision, A, (i.e. the angle between the velocity vectors of meteoroid and planet) is determined by a method using directional cosines. The relative or geocentric

producing 136 meteoroid streams (see McBride & Hughes, 1990a). Three real meteoroid streams, the Quadrantids, the Taurids and the Perseids are investigated to assess how their orbital parameters vary. A 'typical' meteoroid stream is then modelled such that it will vary in a similar fashion to the average observed parameter spreads of the real streams. The orbital parameters modelled are the semi-major axis and the inclination. It is not necessary to model the longitude of the ascending node, Ω, as this does not affect the Earth-meteoroid intersection velocities as long as the planetary orbit is assumed to be circular. The stream perihelion distance distribution is also ignored. As a result the parent cometary orbit is given an 'anchor point' at perihelion where most meteoroid emission occurs. If a cometary orbit had a semi-major axis a_c AU then the modelled meteoroids were given sixteen orbital semi-major axes of $0.5a_c$, $0.6a_c, \ldots, 2.0a_c$ AU respectively and each was given a weighting factor derived from the 'typical' stream orbital parameter profiles. Nine weighted inclinations were also introduced for each stream ranging from -4° to +4° giving a total number of modelled meteoroids in each stream of $16 \times 9 = 144$.

The particles placed around the cometary orbits are identical, i.e. of equal mass. This means that all 136 comet-streams are assumed to have identical masses, an assumption that is incorrect in reality. The relationship between the mass of a parent comet and the mass of its meteoroid stream has been investigated by Hughes (1985). Hughes assumed that the comet nucleus lost on average a constant thickness of material at each perihelion passage. (In reality the majority of mass loss will be restricted to active areas on the nucleus surface. However, the positions of these active areas will probably change with time resulting in the erosion of the whole nucleus surface). The nucleus radius can be thought of as decreasing linearly as a function of the time spent in the inner solar system. This decay process results in the mass of a meteoroid stream increasing quickly at first and hence the mass of a meteoroid stream depends on the original size and the 'age' of the parent comet. It is considered valid, however, to consider an equal mass comet-stream model in order to gain an insight into the general time averaged meteoroid geocentric velocity distribution.

A further question that must be considered is whether the 136 short-period comets is a truly representative data set. It is almost certain that the 136 short-period comets is not the *whole* data set. Stream-producing comets may decay, disintegrate or become generally inactive or dormant. Comets are only detected if they are bright enough to be observed from Earth. Therefore the 136 short-period comets are just a data set containing the brightest short-period comets. There must be many small and/or inactive comets that go unnoticed. To gain an insight into the size distribution of the short-period comets we must calculate a parameter known as the mass distribution index. A mass distribution index, s, is used to characterise a distribution of particles over a specific mass range (see Chapter 5). Hughes (1990a) concluded that the mass distribution index for comets is (1.57 ± 0.003). This means that the large majority of the total mass of cometary material is concentrated in the few largest comets. This also means that the contribution by mass to the cometary meteoroid

velocity, V_g, at the Earth's distance from the Sun will be the vector sum of the meteor's heliocentric velocity, V_H, and the Earth's orbital velocity, V_E. Hence,

$$V_g = \sqrt{V_H^2 + V_E^2 - 2V_H V_E \cos A} \tag{2.8}$$

To account for the acceleration due to the Earth's gravity the corrected geocentric velocity, V_C, is

$$V_C = \sqrt{V_g^2 + V_{esc}^2} \tag{2.9}$$

where V_{esc} is the Earth's escape velocity. The correction for the Earth's attraction varies from about 1 km s^{-1} to 5 km s^{-1} for the extreme cases of head-on collisions (i.e. high relative velocities) and approach from behind (low relative velocities) respectively. So we end up with an intersection velocity V_C km s^{-1} for each modelled meteoroid that has $q \leq 1$ AU and $Q \geq 1$ AU. The results are shown in Fig. 2.10(d) in the form of a histogram.

The mean corrected geocentric velocity is found to be 40.6 km s^{-1}. The absence of meteoroids with velocities in the range 35 km s^{-1} to 39 km s^{-1} is due to the fact that comets associated with meteoroid streams with these characteristic geocentric velocity values have disappeared entirely e.g. Virginids and Geminids. (This may not be true for the case of the Geminids after the discovery of apollo asteroid 3200 Phaethon (1983 TB) which is moving on an orbit that is essentially identical to the mean orbit of the observed Geminid stream). It is important to note that histogram 2.10(d) corresponds to cometary meteoroids produced by presently observed short-period comets only. The model does not account for sporadic meteoroids, meteoroids of asteroidal origin, or for the existence of meteoroid streams for which no parent body can be directly observed.

The scarcity of meteoroids with velocities between 55 km s^{-1} and 59 km s^{-1} is a real characteristic due to the lack of existing high inclination ($\leq 90°$) prograde and low inclination ($\geq 90°$) retrograde short-period comets.

The gravity corrected geocentric velocity distribution can be resolved into a series of peaks which are dominated by major showers (see Table 2.5 and Fig. 2.11(a)) and the correlation between the observed average shower velocities (Cook, 1973) and the modelled geocentric velocities (V_g) is good.

The process can be repeated for the other planets. The velocity distribution for Mars is shown in Fig. 2.11(b). This suggests that approximately half of all visual meteors incident on Mars have gravity corrected planetocentric velocities in the range $10 < V_g < 20$ km s^{-1}, maximising at around 16 km s^{-1} with the mean planetocentric velocity being around 23 km s^{-1}. The gravitational attraction of Mars only has a very small effect on the velocities of head-on collision meteors but does effect those catching up by up to 3 km s^{-1}. However, a word of caution is required here. This analysis applies to large (> 1 mg) cometary meteoroids only. The resulting ratio of flux densities of meteoroids to Earth and Mars is 1 : 2.5. Mars is close to the inner edges of the asteroid belt, which is likely to contribute considerably to the

Meteoroid Stream	Observed Velocity $V_{g_{obs}}$ km s^{-1}	Modelled velocity $V_{g_{mod}}$ km s^{-1}
τ Herculids	15	14.5
Taurids	29.2	29.5
Quadrantids	41.5	41.5
Perseids	59.4	60.5
Orionids	66.4	66.5
Leonids	70.7	70.5

Table 2.5: The table shows the observed mean geocentric velocities for some of the main annual meteor showers, as given by Cook, 1973. The velocities do not include the acceleration due to the Earth's gravitational attraction. The right hand column lists the corresponding mean modelled geocentric velocities (all velocities are in km s^{-1}).

solar system meteoroid dust cloud through cratering and fragmentation events. Mars also has two small satellites which pollute the circum-martian space due to their own impacts with meteoroids (Babadzhanov, 1994). As a result the Mars to Earth ratio of meteoroid flux densities is expected to be higher in reality than it is for this model, perhaps as high as 1 : 10.

Meteoroid streams contain a much higher proportion of large particles than the sporadic background and therefore produce brighter meteors. Thus the dust cloud model based on 'typical' meteoroid streams is expected to have a geocentric velocity distribution resembling that of the observed visual meteors in Fig. 2.10(b). However, a question arises as to whether the observed velocity distribution should resemble a realistically modelled velocity distribution so closely. A meteor becomes visible because the incident meteoroid creates a trail of excited and ionised atoms in the Earth's atmosphere. The ability to detect meteor trails in the atmosphere depends on the luminosity of the trail. This is usually proportional to the electron line density, α_z, for the meteoroid mass range covered here. The electron line density can be represented theoretically (Verniani, 1973) by

$$\alpha_z = 2.0 \times 10^{-10} m V_g^4 \quad \text{m}^{-1} \tag{2.10}$$

where m is the causative meteoroid mass. Hence, if we assume m is constant then the detection limit is governed by the velocity of the incident meteoroid, V_g. This suggests that there are many meteors which cannot be observed visually simply because they have such low geocentric velocities that they produce insufficient ionisation for detection. A velocity distribution free from observational selection should show an abundance of low velocity (< 30 km s^{-1}) meteors. As the dust cloud model was derived from real meteoroid streams whose orbital parameters are determined from Earth, this too is subjected to the same observational selection. It is therefore necessary to introduce some method to compensate for this velocity dependent detection limit.

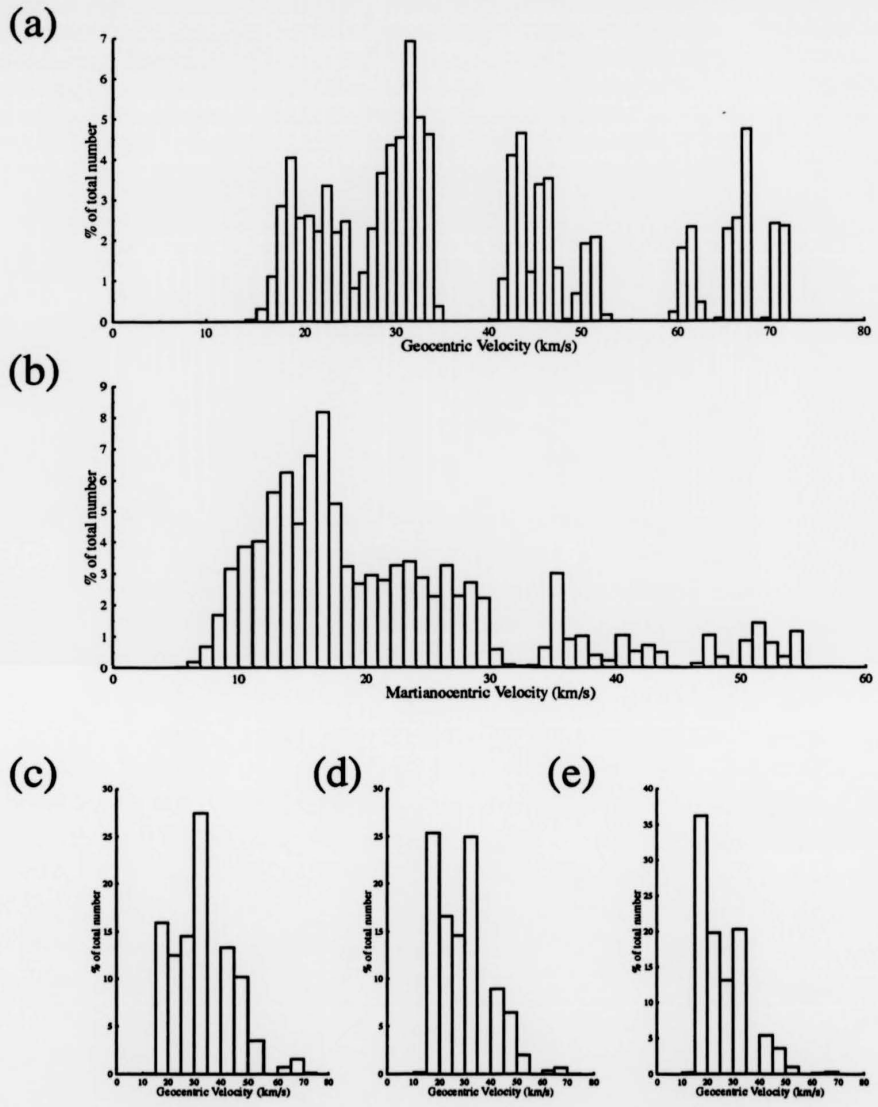

Figure 2.11: Histogram (a) shows the modelled gravity corrected velocity distribution in more detail. The peaks in the distribution correspond to contributions from one or more specific showers with a characteristic range of velocities. The mean observed and modelled geocentric velocities for these peaks are shown in Table 2.5 (after subtraction of the velocity increase due to the Earth's attraction). Histogram (b) shows the Martianocentric velocity distribution. Histograms (c), (d) and (e) show the geocentric velocity distributions after applying three different 'cosmic weighting factors'. These factors are designed to account for the velocity dependence of observability of incident meteors.

2.6.2 The cosmic weighting factor

A simple approach to the problem is to directly multiply the numbers of meteoroids by a factor that increases as the velocity decreases. The 'cosmic weighting factor' (CWF) is designed to be inversely proportional to the probability that meteoroids of constant mass in their observed orbits will, in unit time, collide with the Earth and produce photographable meteors.

Öpik (1951) considered the probability of collision, P_c, between a particle in an orbit of known a, e and i and a planet (say the Earth). He included the effects of perturbative motions in the node and the argument of perihelion, assuming that the inclination remained unchanged. The probability of collision is given by

$$P_c = \frac{\tau^2 V_i}{\pi \sin i \sqrt{2 - \frac{1}{a} - a(1-e^2)}} \qquad \text{per revolution of the particle,} \tag{2.11}$$

where τ is the planet's capture cross-section and V_i is the incident meteoroid velocity in units of the planet's orbital velocity.

Whipple (1954) considered the effects of a meteor's velocity on its chance of being photographed. Assuming that all meteor trails have the same length in the atmosphere ($\sim$ 40 km), equation 2.10 indicates that the total energy in the photographic region varies as the fourth power of the velocity, V^4, since the deceleration is not marked during the visible trail. The heights of the fainter, or shorter, trails vary roughly as $V^{\frac{1}{4}}$, and statistically the trail distances should vary similarly. The area subtended by a camera varies as the square of the height and, possibly, the reciprocity failure varies as a small power of the linear velocity, since meteors have shorter effective exposure times than the optimum.

So the velocity dependence of observability term includes V_i^4 for luminous efficiency , $V_i^{-\frac{1}{4}}$ for height of train, $V_i^{\frac{1}{2}}$ for the area on the meteor region, a small negative power of V_i for reciprocity failure, and V_i^{-1} for length of trail. This gives an overall detection probability, P_d, of approximately V_i^3, i.e.

$$P_d \propto V_i^3$$

Therefore, combining the two probabilities produces a CWF of

$$CWF = \frac{\sin i \sqrt{2 - \frac{1}{a} - a(1-e^2)}}{V_i^4} \tag{2.12}$$

i.e.

$$CWF \propto V_i^{-4}$$

With this weighting factor introduced into the dust cloud model a velocity distribution as shown in Fig. 2.11(d) is produced. Distributions are also shown corresponding to (c) $CWF \propto V_i^{-3}$ and (e) V_i^{-5} for comparison. You can see how the population of retrograde (high velocity) meteors pales into insignificance when compared to the inferred population of slower prograde orbits.

Chapter 3

Perseid meteoroids - the relationship between meteoroid mass and orbital semi-major axis

3.1 Introduction

According to presently held views of meteoroid stream formation, a meteoroid stream should have the most massive meteoroids concentrated around the mean stream orbit and the orbital parameters of the less massive meteoroids should be more and more dispersed.

When a cometary nucleus approaches the Sun (within around 3 AU) the absorption of Solar radiation causes the sublimation of the nucleus surface snows. Momentum is transferred from the radial flux of gas, emanating from the sublimating cometary snows, to the loosely bound surface meteoroid dust. This not only 'un-glues' the meteoroids but also pushes the free meteoroids away from the nucleus surface against the extremely weak cometary gravitational field (the escape velocity from the surface of the nucleus of P/Swift-Tuttle, for example, the parent comet of the Perseid meteoroid stream, is about 0.004 km s^{-1}). During meteoroid stream formation it is not the gas velocity that is important but the velocity of the dust particles that are caught up in the gas flow. Meteoroids responsible for the formation of visual Perseid meteors are thought to have densities in the region of 0.3 g cm^{-3} and they thus have a large surface area to mass ratio. The velocity, V_∞, attained by a meteoroid that has broken away from the gravitational potential well of the cometary nucleus (corresponding to a cometocentric distance of around 10 nucleus radii) is thought to be given by the equation

$$V_\infty^2 = \frac{4.3 \times 10^5 R_c}{n r_m \rho_m r^{\frac{2}{4}}} - 6370\ R_c^2 \qquad \mathrm{cm^2 s^{-2}} \tag{3.1}$$

where R_c km is the equivalent radius of the cometary nucleus, n^{-1} is the fraction of incident solar radiation that is used for ice sublimation, r AU is the heliocentric distance of the comet at the time of meteoroid ejection, and r_m and ρ_m are the radius and density of the meteoroid

in cgs units respectively (see Whipple, 1950, 1951; Hughes, 1977). Equation 3.1 is often known as the 'Whipple formula'. The semi-major axis, a_m, of the resultant meteoroid's orbit is given by

$$a_m = a_c + 2.26 \times 10^{-3} a_c^2 V_c V_\infty \cos\phi \quad \text{AU} \tag{3.2}$$

where a_c is the semi-major axis of the parent comet, V_c is the heliocentric velocity of the comet and ϕ is the angle of meteoroid emission in relation to the direction of comet motion. For typical photographic Perseids, with estimated masses in excess of 1 mg, the first term on the right hand side of equation 3.1 is at least 50 times greater than the second term. This means that the meteoroid ejection velocity should be proportional to $(r_m \rho_m)^{-0.5}$. It would thus be expected that the ejection velocity should be a function of meteoroid mass and hence the distribution of meteoroid orbital semi-major axes should also be a function of meteoroid mass.

This suggestion is investigated in the following chapter. The analysis will concentrate on the Perseid meteoroid orbits obtained from photographic meteor survey patrols. This collection of meteoroids is found to have the most probable mass m_p given by $\log m_p(\text{g}) = -0.19$, the standard deviation about this logarithmic mass value being ± 0.7. The meteoroids responsible for the Perseid meteors have characteristic velocities with respect to the Earth's atmosphere of around 60 km s^{-1}. The meteoroid mass, m (g), can be determined from the atmospheric velocity, V (cm s^{-1}), and the visual magnitude, M_V, of a meteor. Verniani (1973) analysed 6000 underdense radio meteors and found empirically that

$$0.92 \log m = 24.214 - 3.91 \log V - 0.4 M_V \tag{3.3}$$

whereas a theoretical approach to the problem gave

$$\log m = 25.7 - 4.0 \log V - 0.4 M_V \quad . \tag{3.4}$$

This places a great importance on accurate individual meteoroid velocity determination. For Perseid meteors we have, from equation 3.3

$$\overline{M}_V = -3.47 - 2.3 \log m \tag{3.5}$$

and from 3.4

$$\overline{M}_V = -3.534 - 2.5 \log m \tag{3.6}$$

assuming that $\overline{V} = 6 \times 10^6$ cm s^{-1}. Whipple (1955) gave

$$M_V = -4.25 - 2.5 \log m \quad . \tag{3.7}$$

Table 3.1 gives the causative meteoroid masses, m (g), for meteors of specific visual magnitude, M_V, determined from equations 3.5, 3.6 and 3.7. It is important to note that the meteoroid masses listed in meteor data files have not all been calculated by the same

investigator and thus the resulting values may have an associated mass error comparable to the differences between the values listed in Table 3.1. In most cases the potential errors in the semi-major axis determination are such that the third decimal place is in doubt (see Lindblad, 1991).

M_V	8	5	2	-1	-4	-7
m(g) from 3.5	1.0×10^{-5}	2.1×10^{-4}	4.2×10^{-3}	0.084	1.7	34
m(g) from 3.6	2.4×10^{-5}	3.9×10^{-4}	6.1×10^{-3}	0.097	1.54	24
m(g) from 3.7	1.3×10^{-5}	2.0×10^{-4}	3.2×10^{-3}	0.05	0.79	13

Table 3.1: The causative meteoroid masses, m(g), are listed for specific meteor magnitudes, M_V, according to varying mass/magnitude/velocity relationships.

The Perseid meteoroids have high orbital inclinations (around 113°) and their ascending and descending nodes are well away from the orbits of the major planets. Hence the stream suffers very little from short-term orbital perturbation and the orbital parameters of the stream meteoroids, especially the semi-major axes, are expected to provide a major clue as to their formation mechanism.

3.1.1 The Poynting-Robertson effect

It is widely accepted that the Poynting-Robertson effect is the main cause of mass segregation in meteoroid streams. Electromagnetic radiation absorbed by the meteoroids is reradiated isotropically, in the frame of reference of the meteoroid, causing a tangential drag. The main effect is a loss of meteoroid angular momentum resulting in the eventual spiralling of the meteoroid into the Sun. An expression for the PR lifetime was given in Chapter 2 (equation 2.3). Poynting attributed the drag to a back pressure of radiation tending to retard the motion of the emitting body due to a 'crowding-up' of radiation in front of the particle and a corresponding 'thinning-out' behind. Poynting's estimation for the magnitude of the force was $\frac{1}{3}\Theta\frac{V_H}{c^2}$, where Θ is the rate at which the body is radiating energy, V_H is the body's heliocentric velocity and c the velocity of light. Gravitational force varies as the cube of the linear dimensions of the particle whereas Θ varies as the square of the linear dimensions. Therefore the effect should increase as the size of the body decreases.

The full relativistic calculation of the effect was performed by Robertson (1937) but the simplified Newtonian approximations involving only first order terms in $\frac{V_H}{c}$ are sufficient for the calculations in this section.

The secular perturbations for an osculating ellipse of semi-major axis a and eccentricity e are:

$$\frac{da}{dt} = -\frac{\kappa(2+3e^2)}{a(1-e^2)^{\frac{5}{2}}} \tag{3.8}$$

$$\frac{de}{dt} = -\frac{5\kappa e}{2a^2(1-e^2)^{\frac{1}{2}}} \tag{3.9}$$

where

$$\kappa = \frac{2.51 \times 10^{11}}{\rho r} \tag{3.10}$$

where ρ and r are the particle density and effective radius respectively (see Lovell, 1954).

Burns *et al.* (1979) give the solution as

$$\frac{de}{dt} = -\frac{5}{2}\frac{\eta}{l^2}e(1-e^2)^{\frac{3}{2}} \tag{3.11}$$

where l is the semi-latus-rectum of the orbit, and η is a parameter given by

$$\eta = \frac{3LQ(s)}{4\pi c^2 \rho r} \tag{3.12}$$

where L is the solar luminosity and $Q(s)$ is the efficiency factor for absorption and scattering of radiation. Inserting standard values, with $Q(s) = 1$, gives

$$\eta = \frac{2.53 \times 10^{11}}{\rho r} \quad \text{cgs units.} \tag{3.13}$$

For the case of an 'average' photographic Perseid meteoroid (a=28 AU, e=0.965 (see Cook, 1973)) with a density of 0.3 g cm^{-3} and effective radius of around 1 cm (Hughes, 1977) the effect on particle orbital eccentricity is approximately -1.4×10^{-9} per year, compared to -3×10^{-8} per year for an 'average' Quadrantid meteoroid of the same radius and density (see Hughes *et al.*, 1981), an effect some 20 times greater.

Thus, the Poynting-Robertson effect is expected to have only a very limited influence on the orbital parameters of the Perseid stream meteoroids being considered here.

3.1.2 Radiation pressure

The force of repulsion arising from Solar radiation pressure on a small enough particle can be considerably greater than the gravitational attraction of the Sun on this particle. A particle of mass $\frac{4}{3}\pi r_m^3 \rho_m$ at a distance d from the centre of the Sun suffers gravitational attraction towards the Sun, F_{att}, according to Newton's law,

$$F_{att} = \frac{GM}{d^2}\frac{4}{3}\pi r_m^3 \rho_m \tag{3.14}$$

where M is the mass of the Sun. The opposite effect is the force of repulsion, F_{rad}, due to radiation pressure which is given by

$$F_{rad} = \frac{1}{c}\frac{Lr_m^2}{d^2} \tag{3.15}$$

where c is the velocity of light and L is the total luminosity of the Sun (the radiation emitted from the Sun in all directions per second). By dividing the former equation by the latter we can see that for a particle of given density, radiation pressure is larger than gravitational force if the radius r_m of the particle fulfils the inequality

$$r_m < \frac{L}{\frac{4}{3}\pi G M c} \frac{1}{\rho_m} \tag{3.16}$$

Inserting standard values for L, G, M and c into equation 3.16 gives

$$r_m < \frac{2.5 \times 10^{-4}}{\rho_m} \text{ cm} \tag{3.17}$$

Thus a Perseid meteoroid with a density of 2.9, 0.29 and 0.029 g cm^{-3} would require a corresponding radius of less than 8.62×10^{-5}, 8.62×10^{-4} and 8.62×10^{-3} cm respectively to fulfil inequality 3.17. Another expression for the ratio of these forces is approximately given by (see for example Leinert & Grün, 1989)

$$\beta = \frac{F_{rad}}{F_{att}} \simeq \frac{5.7 \times 10^{-5}}{\rho_m r_m} \tag{3.18}$$

As the meteoroid data used in the following sections have estimated effective radii, r_m, greater than about 0.05 cm and estimated masses in excess of around 10^{-3} g then radiation pressure is also not considered to be a major influence on the Perseid meteoroid orbital parameters.

3.2 Perseid orbit search

A search was made through the IAU Photographic Meteor Data Catalogue (see Lindblad, 1987, 1991) for possible Perseid meteors by using a succession of 'sieving' techniques. Meteors were firstly selected that (a) occurred between July 23 and August 23 and (b) had causative meteoroids with calculated masses and orbits. This yielded 576 Perseid candidates. This group was further reduced by selecting the meteoroids that had orbits with
$100° < i < 128°$; $140° < \omega < 164°$; and $117° < \Omega < 149°$.
These orbital constraints eliminate those meteoroids contained in the group of 576 that belong to other non-Perseid streams. Meteoroids that fell within these approximate orbital ranges were assumed to be Perseid stream members.

The resulting 291 meteoroids had median orbital parameters of
$q_{med} = 0.951$ AU; $e_{med} = 0.971$; $i_{med} = 113.1°$; $\omega_{med} = 151.0°$ and $\Omega_{med} = 139.0°$.
This orbit was taken to be the initial median orbit of the photographic Perseid meteoroid stream.

The D' criterion (see section 2.2.1) was then used to select Perseids more accurately from the original 576 meteors. The D' criterion was also used to select the 'core' of the stream and segregate these core meteoroids from the more dispersed meteoroids which could have resulted from perturbations or collisions. The method is based on a calculation of the sum of the differences between each of the five orbital elements q, e, i, ω, and Ω of a particular meteoroid and the orbital elements of the assumed median shower orbit. Initially, the meteoroids with $D' < 0.20$ ($D_0 = 0.20$) were then used, with a weighting factor of $(1 - \frac{D'}{D_0})$, to calculate a new mean orbit. The process was repeated with the new mean orbit replacing

the initial Perseid orbit until the same set of meteoroids was selected on two successive loops of the program.

The end-product was the selection of 299 photographic Perseid meteoroid orbits and their D' distribution is shown in Fig. 3.1. It can be seen that the Perseid shower probably extends out to a D' of about 0.16. This agrees favourably with the formula (2.2) for D_0 given by Lindblad for a data set of 576 meteoroids. Using $D_0 = 0.16$ gives a data set containing 285 meteors. It also seems reasonable to define the 'Core Photographic Perseids' (CPPs) as having $D' < 0.07$ (dashed line, Fig. 3.1). The selection program was run again, this time taking $D_0 = 0.07$, and the result was a data set of 205 CPPs with mean orbital parameters of

$q_m = 0.949$ AU; $e_m = 0.969$; $i_m = 113.1°$; $\omega_m = 150.8°$ and $\Omega_m = 138.8°$

This is the orbit quoted in Table 3.2 (the standard deviations for these mean stream orbital parameters are given on page 44).

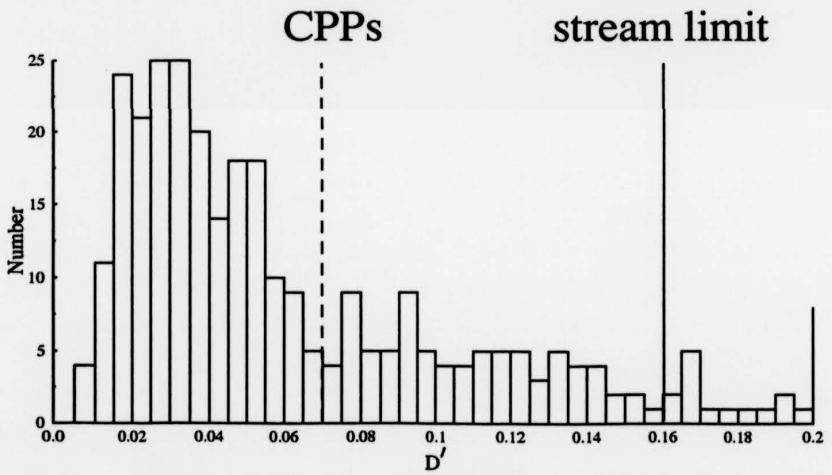

Figure 3.1: The histogram shows the distribution of D' for the 299 photographic meteors that have $D' < 0.2$. The dashed vertical line at $D' = 0.07$ segregates the 'Core Photographic Perseids'. The bold vertical line at $D' = 0.16$ indicates the probable full extent of the Perseid stream.

The orbits of the 205 CPPs are represented in Fig. 3.2. The inner and outer bold circles represent the orbits of Jupiter and Neptune respectively and the bold ellipse represents the orbit of parent comet P/Swift-Tuttle.

Fig. 3.3 shows the normalised orbital element distributions of the 205 CPPs. The semi-major axis distribution indicates that the data set contains 45 meteoroids with either hyperbolic or parabolic orbits. The distribution of perihelion distances has a mean of 0.949 AU and the standard deviation of the data about the mean is ±0.027 AU. For

Figure 3.2: The plot represents the orbits of the 205 CPPs. The inner and outer bold circles represent the orbits of Jupiter and Neptune respectively and the Sun is marked by the central dot. The black bar at the top of the diagram indicates the direction of the First Point of Aries and the bold ellipse indicates the orbit of the parent comet P/Swift-Tuttle.

	T	e	q (AU)	ω(deg)	Ω(deg)	i(deg)	P(y)	source
69 BC	Aug 27.1017	0.96136	0.98087	152.42151	139.90174	113.90174	127.91	1
188 AD	Jul 10.5453	0.96216	0.97224	152.6396	139.25850	113.86404	130.27	1
1737 II	Jun 15.8537	0.96137	0.97997	152.6931	139.46155	113.67987	127.77	1
1737 II	Jun 3.53	1.0	0.8381	129.96	135.99	63.84	∞	2
1862 III	Aug 23.42278	0.962798	0.962655	152.77369	139.37148	113.56644	131.68	1
1862 III	Aug 23.41	0.96043	0.96264	152.766	138.685	113.56	120	2
1992t	Dec 12.32394	0.963589	0.958175	153.00138	139.44442	113.42658	135.02	1
2126	Jul 12.41024	0.963876	0.956272	153.1185	139.60915	113.40857	136.20	1
Perseids		0.9577	0.9680	155.52	141.47	119.70	109.5	3
		0.9474	0.9474	150.89	149.35	112.20	77.1	4
		0.93	0.97	153.	139.5	114.	54.6	5
		0.965	0.953	151.5	139.0	113.8	148.2	6
		0.969	0.949	150.8	138.8	113.1	169.4	7

Table 3.2: The orbital parameters for comet P/Swift-Tuttle and for the Perseid meteoroid stream. T is the time of perihelion passage and P is the orbital period in years. The source numbers correspond to : 1 Yau, Yeomans & Weissman (1994), 2 Marsden (1986), 3 Whipple (1938), 4 Ceplecha (1951), 5 Hawkins & Almond (1952), 6 Cook (1973), 7 Harris & Hughes (1994).

eccentricity the values are 0.969 and $\pm$0.075. For inclination, argument of perihelion and longitude of ascending node the values are 113.1°, $\pm$4.1°; 150.8°, $\pm$5.9° and 138.8°, $\pm$5.1° respectively. We would like to know the mean orbital parameters of the Perseid meteoroid stream, together with their standard deviations. Unfortunately the values given above apply to the sub-set of Perseids that have hit Earth, and not to the stream in general.

The problem is illustrated schematically in Fig. 3.4. Every year the Earth 'drills' a hole through the Perseids. The distribution of the meteoroid ecliptic-intersection points is unknown. Another unknown is how close to the 'centre' of the stream the Earth actually passes. The acquisition of this information will be investigated in Chapter 4. The only Perseids that are detected are those that have descending nodes that intersect the Earth's orbit at the time when the Earth is present. We must ask ourselves whether the orbital parameters of this sub-set are typical of the stream in general or whether the observed orbital parameter distribution is greatly biased by the observed selection conditions.

An easy way of answering this question is to plot the parameter of an orbit as a function of the longitude of the perihelion of the specific orbit. A set of these plots are shown in Fig. 3.5.

The distributions of semi-major axis, eccentricity and inclination clearly show no trends as a function of the longitude of the perihelion. This, however, cannot be said for the distribution of perihelion distances. It can thus be concluded that the mean perihelion distance of the observed meteoroid orbits is *not* the same as the mean perihelion distance of the total stream, whereas the mean values of the other three parameters *do* apply to the total stream.

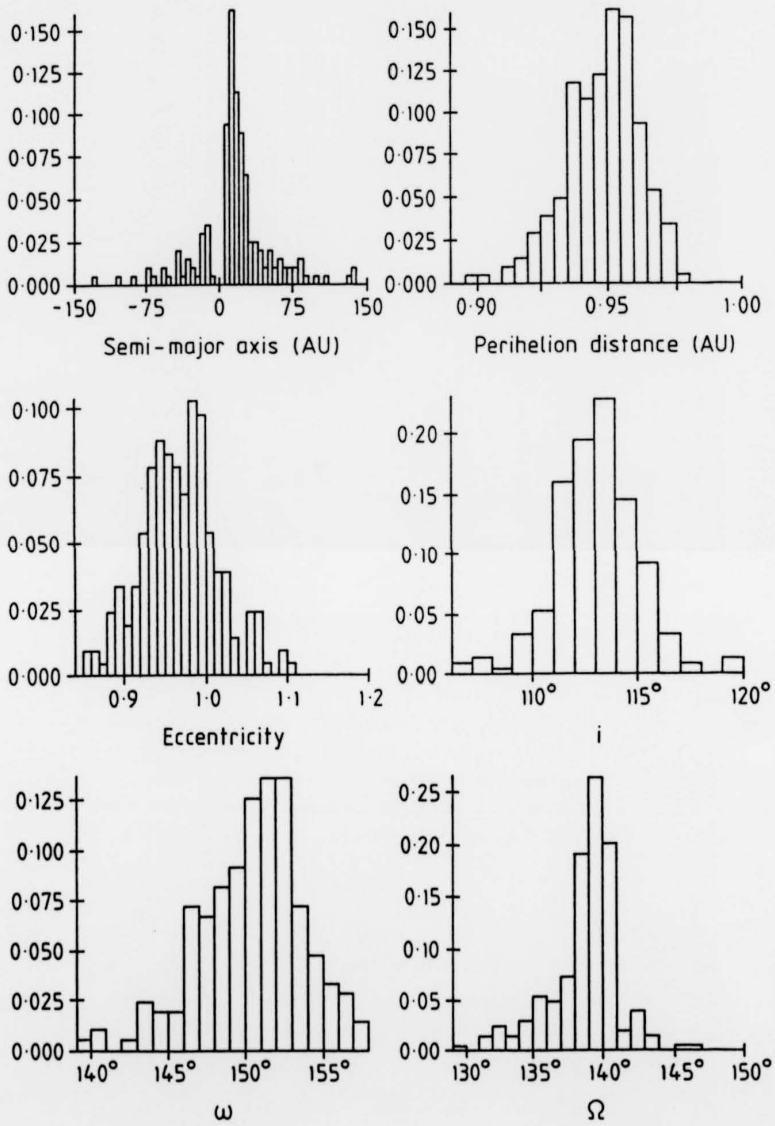

Figure 3.3: The normalised orbital parameter distributions for the 205 CPPs. The ordinate values represent the number of orbits in each histogram bar divided by the total number of orbits.

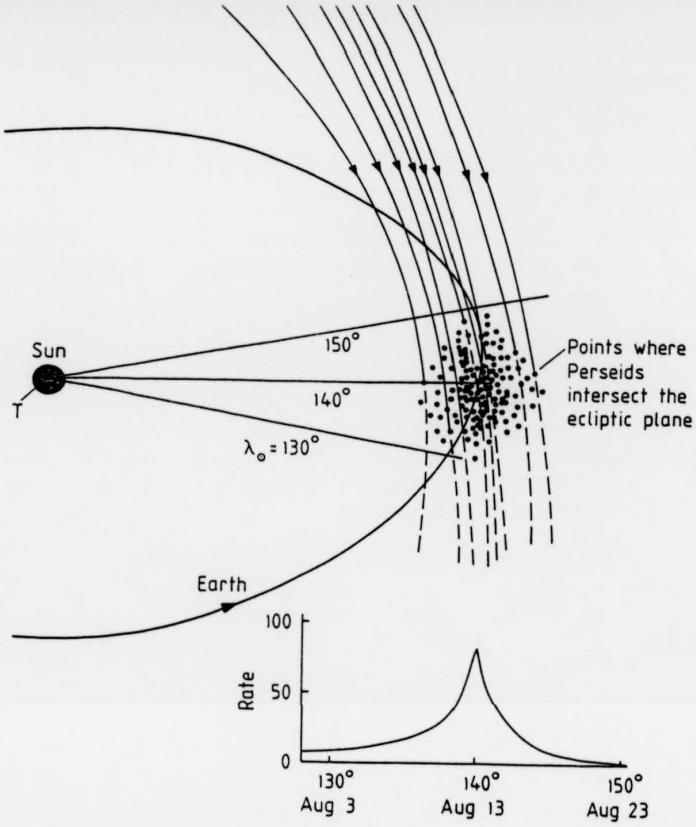

Figure 3.4: A schematic illustration of the intersection of the Perseid meteoroid stream with the ecliptic plane. The dashed portions of the meteoroid orbits are below the plane. Note that it is not known whether the profile of the intersection points is actually circular or whether the Earth passes through the most dense part of the stream. The lower diagram shows how the observed rate of meteors varies as a function of λ_0, the solar longitude.

The completeness of the data between July 23 and August 23 must also be questioned. The IAU Photographic Meteor Data Catalogue is a collection of observations taken by different experimenters, using different instruments that were used for different time periods. The number of camera systems that were running was certainly not constant throughout the July 23 to August 23 period. More are expected to have been active around the time of Perseid maximum. The completeness of the data is indicated in Fig. 3.6. The number of meteoroid orbits in the data set peaks between August 11.5 and 14.0, maximising around August 12.75. The decline in activity after August 13 is much sharper and smoother than the gradual, fluctuating rise to maximum activity. The distribution of semi-major axes, a, as a function of date of observation shows that the maximum spread in a occurs around August 13.0, coinciding with the peak in activity. The distribution of observed meteoroid masses as a function of date of observation, shown in Fig. 3.6(c) for $m < 30$ g (97% of the data set) has

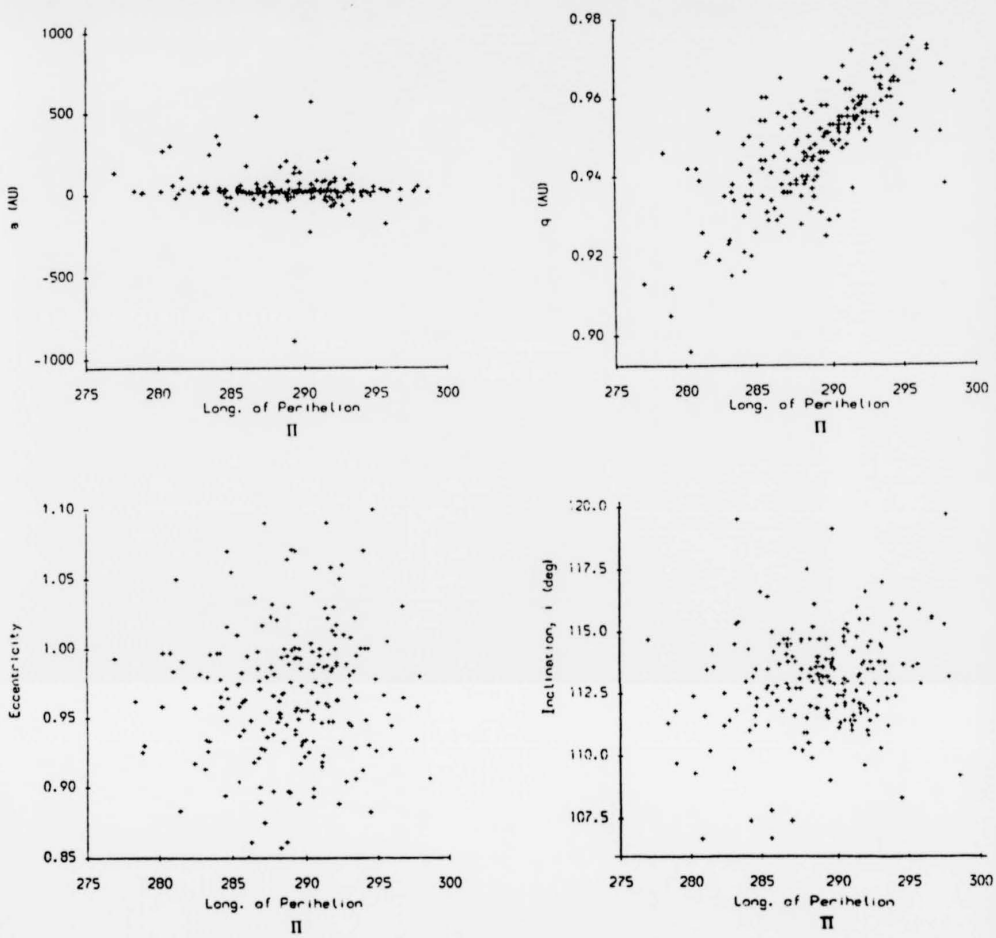

Figure 3.5: The orbital parameter distributions for the 205 CPPs with respect to longitude of perihelion Π. The perihelion distance of an observed Perseid meteor is clearly a function of its longitude of perihelion.

a meteor mass-range peak between August 12.0 and 13.0, also coinciding with the peak in activity. The general profiles of the distributions in Fig. 3.6(b) and (c) are almost identical to the meteor number distribution in (a), characterised by a gradual rise to maximum over a period of about 10 days from August 1 to August 11 followed by a steep decline to negligible numbers during the 6 days following August 13.

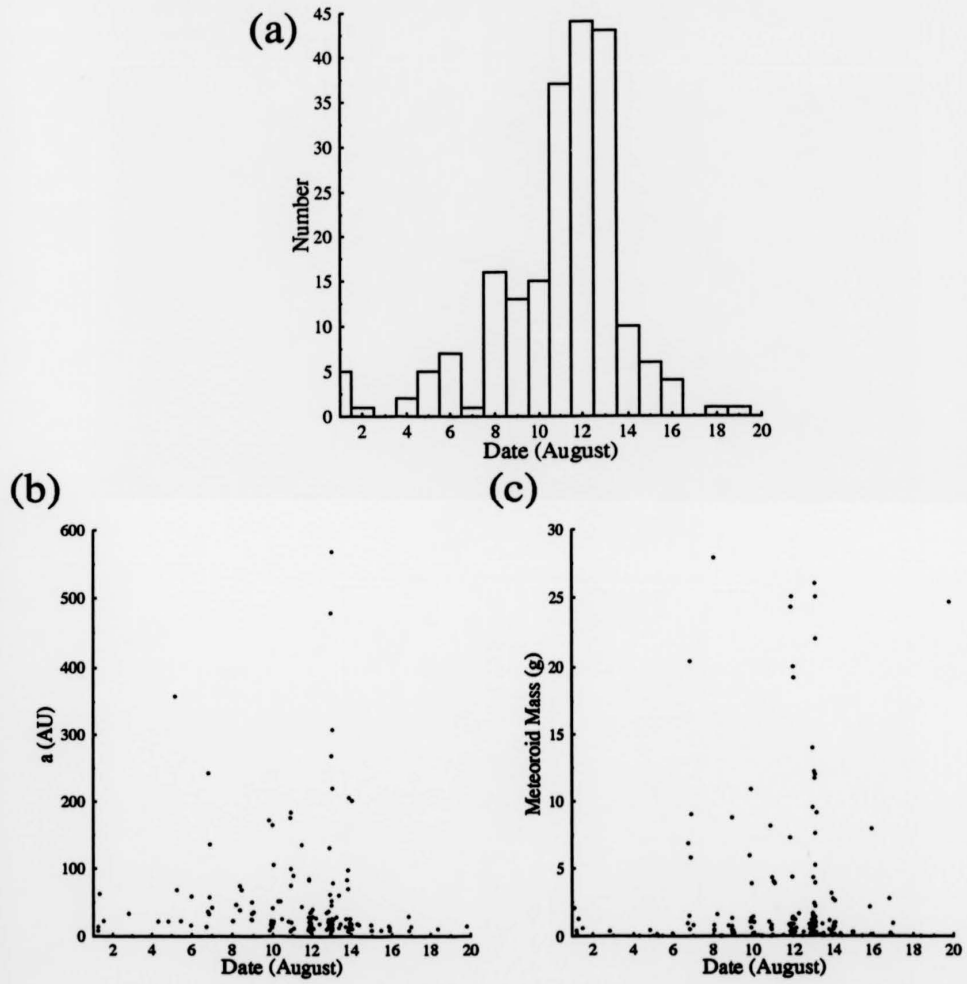

Figure 3.6: The distribution of (a) the number of recorded meteoroid orbits, (b) their semi-major axes and (c) the masses of the meteoroids, plotted as a function of time of occurrence. The maxima in all three cases occur around August 13.0.

3.3 Variation of the semi-major axis distribution as a function of meteoroid mass

Meteoroids with eccentricities of 1.00 or greater were deleted from the CPP file to produce a new file containing 160 Perseids. The distribution of meteoroid semi-major axis as a function of mass is shown in Fig. 3.7. The general impression is that the scatter in the semi-major axis distribution increases as the mass gets smaller. Unfortunately the strength of this impression is mainly due to the fact that there are many more low mass meteoroids than high mass ones.

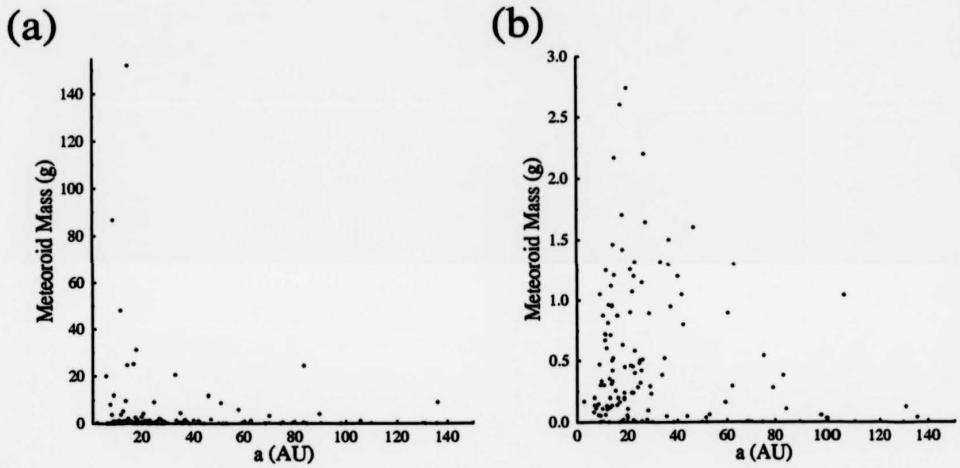

Figure 3.7: Meteoroid mass is plotted as a function of semi-major axis for (a) all the 160 Perseid stream meteoroids with $e < 1.0$ and (b) those out of the 160 with $m_p < 3.0$ g.

To counteract this the data has been sorted in order of mass and then divided into 8 bins, each containing 20 meteoroids. The meteoroids in each bin were then sorted in order of increasing semi-major axis [see Fig. 3.8(a)]. The vertical bars show the semi-major axis range that contains the central 64% of the meteoroids in each bin. The point (•) indicates the median semi-major axis value, a_{median}, and the horizontal dashed line at 21.25 AU indicates the median semi-major axis of the 160 meteoroids.

Fig. 3.8(a) shows clearly that there is *no systematic variation* in either the median semi-major axis or the spread of the data as a function of Perseid meteoroid mass.

As a check on this result the IAU Photographic Meteor Data Catalogue was searched for Geminid meteoroids. The 88 core Geminids that were found were sorted into 8 bins, each containing 11 meteoroids. The semi-major axis/mass distribution is shown in Fig. 3.8(b) and this distribution is found to have a similar lack of systematic variation with meteoroid mass.

As mentioned earlier, the semi-major axis of an ejected meteoroid orbit depends on the

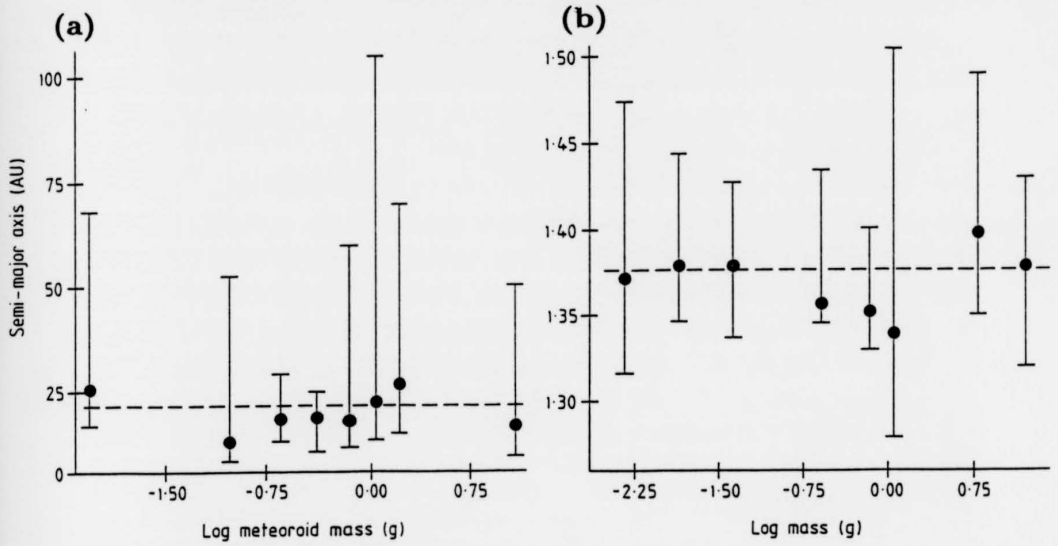

Figure 3.8: (a) The 160 Perseids with $e < 1.0$ have been sorted into eight mass bins and the vertical lines represent the centres of these bins. The dots indicate the median semi-major axis, a_{median}, of the meteoroids in each bin and the bars at the top and the bottom of each line mark the range that contains the central 64 % of the meteoroids in each bin. The horizontal line at 21.25 AU represents the a_{median} value of all 160 meteoroids.
(b) The 88 Geminids found in the IAU Catalogue have been analysed in a similar way to the Perseids shown in (a). The median semi-major axis for the Geminids is 1.376 AU.

cometocentric velocity, V_∞, that the meteoroid receives as it leaves the nucleus. If, as is shown in Fig. 3.8, the semi-major axis does not depend on mass, then V_∞ must also be independent of mass. Under these circumstances equation 3.1 indicates that the product $r_m\rho_m$ must be independent of mass over the mass range covered by the data set. Using the meteoroid densities quoted in Hughes (1978) (and bearing in mind that the median Perseid meteoroid mass in the data set is 0.6 g) a reasonable expression for this product would be

$$r_m\rho_m = (0.23 \pm 0.05) \text{ g cm}^{-2} \quad . \tag{3.19}$$

This applies to meteoroids with radii greater than about 0.05 cm and masses in excess of around 10^{-3} g.

Perseid meteoroids with masses of 0.006, 0.06, 0.6, 6 and 60 g would thus have densities of 2.9, 0.9, 0.29, 0.09 and 0.029 g cm^{-3} respectively. Verniani (1969) and Tokhtas'ev (1978) concluded that the Perseids had densities of 0.29 and 0.32 g cm^{-3} respectively. Babadzhanov (1994) has determined the densities of 85 meteoroids using the theory of quasi-continuous fragmentation (the phenomenon of gradual meteoroid fragmentation in the atmosphere) and on the basis of lightcurves of meteors. The densities were found to vary in the range from

0.1 to 8 g cm^{-3}, corresponding to porous meteoroids and more dense stony and stony-iron meteoroids. This is exactly what is to be expected of crumbly vesicular meteoroids that are fractal-like, spongy agglomerations of much smaller solid particles. Below a radius of 0.05 cm the meteoroids tend to be solid and to have a density equivalent to that of solid rock. That this description applies to the Perseids is supported by the fact that Benyukh (1970) found that about 30% of Perseid trains had end bursts. This is caused when a low density, dustball meteoroid breaks up into a multitude of grains and the sudden increase in the meteoroid surface area leads to a rapid deceleration and a concomitant loss of kinetic energy in the form of light. Large decelerations indicate low densities.

Chapter 4

Modelling the formation of the Perseid meteoroid stream

4.1 Introduction

According to Lovell (1954) the Perseid meteor shower is 'of great antiquity'. The annual occurrence of the Perseids has been observed for over 12 centuries. Olivier (1925) and Imoto & Hasegawa (1958) have traced its history and have noticed that the shower was recorded at least a dozen times between AD 36 and AD 1451. Its association with comet P/Swift-Tuttle (1737 II = 1862 III = 1992t) was established by Schiaparelli between 1864 and 1866, and was the first plausible comet-meteoroid stream link. The shower normally yields visual zenithal hourly rates of between 50 and 100 over the period of maximum activity from August 10-13 indicating that material is dispersed around the comet orbit. To quote from the 1971 edition of the Encyclopaedia Brittanica:

> In the case of the Perseid shower.. the dispersion (of meteoroids) around the orbit is so complete that no evidence of long-term periodicity can be found.

The shower also extends considerably either side of maximum, the main bulk of the activity occurring between July 23 and August 23 (Cook, 1973).

Since 1971 meteor astronomers have studied the shower intensity more closely and it is now clear that the annual rate of Perseid meteors varies considerably about the mean value. In 1991 and 1992 short-lived 'bursts' of visual activity were noticed, these increasing the rate by a factor of about 4 above what was expected. The fact that these 'bursts' were reasonably contemporaneous with the perihelion passage of P/Swift-Tuttle has not gone unnoticed. The existence of these short outbursts have been seen in forward scatter radar data. Fig. 4.1 shows a plot of Perseid meteor activity between August 12.125 and August 12.25 1994 (03:00 to 06:00) [data from the Sheffield University meteor radar group]. The variation in the observed meteor rates is seen to be very erratic and the short-lived periods of high activity seem to correspond to the Earth moving through discrete, closely spaced filaments of high meteoroid

spatial density. Considering the velocity of the Earth with respect to the stream, these filaments would be typically less than 20,000 km wide. It is more likely, however, that this erratic activity is simply the result of random fluctuations (noise) in the meteoroid influx.

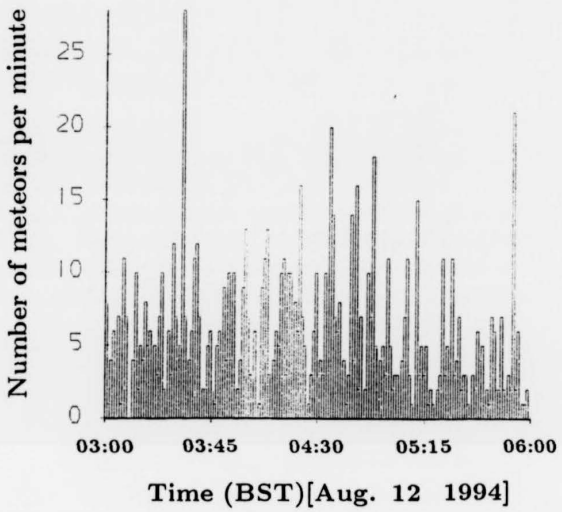

Figure 4.1: The erratic short-term variation of Perseid meteor activity (from the Sheffield University meteor radar group). The histogram bar width corresponds to 1 minute. The activity plot runs from August 12 03:00 to 06:00 BST. Notice the short-lived bursts of high activity attributed to the Earth's passage through discrete 'filaments' of high meteoroid spatial density. This phenomenon could also be attributed simply to random 'noise' in the meteoroid influx.

P/Swift-Tuttle has an absolute magnitude of about 4.5, this being a whole magnitude brighter than P/Halley. There have been no obvious changes in the comet's absolute magnitude over the past three apparitions. Using formulae given by Hughes (1990) the nucleus of P/Swift-Tuttle is found to have an effective radius of about 9 km, making it the largest object known to have an Earth-intersecting orbit (Marsden, 1993). Hughes & McBride (1989) found that the dust in the observed stream had a total mass of about 3×10^{17} g, making the Perseids the most massive known meteoroid stream in the solar system. Both the parent comet and the stream have high orbital inclinations (around 113°) and their aphelia are well away from the orbits of the major Jovian planets. Hence the comet and the stream suffer very little from short-term orbital perturbation and the orbital parameters of the stream meteoroids provide a major clue as to their formation mechanism. The stability of the cometary orbit is indicated by the fact that over the last 2700 years parameters such as the eccentricity, the argument of perihelion, the longitude of the ascending node

and the inclination have only varied by 0.28, 0.47, 0.51 and 0.57 % respectively. Table 4.1 shows that between about 574 BC and AD 2261 the perihelion has decreased progressively by only 0.023 AU (see Yau, Yeomans & Weissman, 1994). This unusual orbital stability has provided a positionally stable source for the production of Perseid Meteoroids over the last few millennia. However, a note of caution is needed here. P/Halley loses on average about 1×10^{14} g of dust per apparition (Hughes 1985). As P/Swift-Tuttle has an absolute magnitude that is one magnitude brighter it is expected to lose about 2.5 times more dust. The perihelion velocity of P/Swift-Tuttle is such that around 14% of the ejected meteoroid dust is forced onto hyperbolic orbits and is thus lost from the stream and the solar system (see section 4.3). A simple division shows that the presently observed stream took about 1500 cometary apparitions to produce. This conclusion assumes that the observed stream is a close representation of the P/Swift-Tuttle dust complex. At a mean orbital period of 130 years this indicates that P/Swift-Tuttle has been producing observable Perseid meteoroids for the past 200,000 years.

In the following chapter the formation of the Perseid meteoroid stream is modelled by considering the way in which the velocity of the meteoroids emitted from the surface of a cometary nucleus (P/Swift-Tuttle), and their numbers, varies as a function of heliocentric distance and comet-Sun-meteoroid ejection angle. Note from the previous chapter that the meteoroid ejection velocity is independent of the mass of the meteoroids in the mass range covered by the data being used. The distribution of modelled Perseid meteoroid orbital parameters will be compared to the observed distributions. The past orbital evolution of parent comet P/Swift-Tuttle is investigated in order to model the meteoroid dust complex that has resulted from the comet's activity over the past 160,000 years. This will then enable us to determine the distribution of the meteoroid descending nodes in the vicinity of the Earth's orbit and also how close to the 'centre' of the stream the Earth passes.

4.2 The cometary ejection of Perseid meteoroids

The way in which the velocity of the gas molecules emitted from the surface of a cometary nucleus changes as a function of sublimation temperature and distance from the nucleus is illustrated schematically in Fig. 4.2. Following Delsemme (1982), let us start by assuming that the subliming gas leaves the nuclear snows with a mean radial efflux velocity, v_0, that is slightly below the mean Maxwellian velocity $\overline{v}$ for the temperature T of the snows ($\frac{1}{2}\overline{v} \leq v_0 \leq \frac{2}{3}\overline{v}$, where $\overline{v} = (\frac{8kT}{\pi m})^{0.5}$, and m is the molecular mass). The upper and lower limits of v_0 correspond to (a) the effusive flow of gas into vacuum from a small hole in a pressurised vessel, and (b) from a subliming solid whose surface is a perfect plane. As this gas is expanding into a vacuum it expands adiabatically in the direction of the pressure gradient. When the gas is a few nucleus radii away from the nucleus surface it has reached a velocity of about 1.77 $\overline{v}$. If it is assumed that the sublimation temperature is 200 K the mean terminal velocity, $\overline{V}_T$,

Table 4.1: Osculating orbital elements for P/Swift-Tuttle (J2000) (Yau, private communication). The mean values have been calculated using the 20 apparitions of the comet prior to 1862.

Return			T(ET)		q(AU)	e	P(Yrs)	ω	Ω	i	Epoch		
2392	2392	9	16.11262	2594978.61262	0.9498238	0.9634832	132.66	153.12568	139.62064	113.58504	2392	9	17.0
2261	2261	8	10.73872	2547095.23872	0.9584214	0.9635052	134.59	153.13973	139.74166	113.49411	2261	8	11.0
2126	2126	7	12.41024	2497757.91024	0.9562718	0.9638758	136.20	153.11853	139.60915	113.40857	2126	7	15.0
1992t	1992	12	12.32394	2448968.82394	0.9582175	0.9635892	135.02	153.00138	139.44442	113.42658	1992	12	4.0
1862III	1862	8	23.42278	2401375.92278	0.9626545	0.9627979	131.68	152.77369	139.37148	113.56644	1862	8	8.0
1737II	1737	6	15.85369	2355652.35369	0.9799742	0.9613652	127.77	152.69309	139.46155	113.67987	1737	6	4.0
1610	1610	2	6.69101	2309137.19101	0.9766687	0.9620380	130.50	152.82010	139.50112	113.55631	1610	2	6.0
1479	1479	10	18.29315	2261552.79315	0.9698281	0.9628540	133.41	152.88476	139.55365	113.48837	1479	10	18.0
1348	1348	5	2.32867	2213536.82867	0.9752229	0.9629495	135.05	152.96871	139.66877	113.47667	1348	5	2.0
1212	1212	11	6.13635	2164050.63635	0.9737912	0.9632596	136.46	152.93792	139.54068	113.38788	1212	11	6.0
1079	1079	9	17.61023	2115422.11023	0.9718508	0.9629921	134.58	152.90036	139.40658	113.48602	1079	9	17.0
950	950	4	19.45072	2068153.95072	0.9762973	0.9620177	130.32	152.70299	139.30202	113.67368	950	4	19.0
826	826	4	19.49363	2022862.99363	0.9770292	0.9614039	127.37	152.86643	139.44021	113.93156	826	4	19.0
698	698	9	6.41835	1976250.91835	0.9726568	0.9620703	129.86	152.86503	139.42888	113.84648	698	9	6.0
569	569	3	1.08586	1928944.58586	0.9702814	0.9623991	131.09	152.70112	139.32056	113.78758	569	2	28.0
441	441	11	3.07052	1882439.57052	0.9793991	0.9615435	128.53	152.48903	139.23131	113.85888	441	11	2.0
316	316	10	27.22997	1836776.72997	0.9777498	0.9615439	128.21	152.68367	139.30258	113.89181	316	10	27.0
188	188	7	10.54528	1789916.04528	0.9722372	0.9621649	130.27	152.63962	139.25850	113.86404	188	7	10.0
59	59	5	17.98690	1742744.48690	0.9698231	0.9624007	131.00	152.52240	139.18612	113.87888	59	5	17.0
69 BC	-68	8	27.10172	1696459.60172	0.9808664	0.9613614	127.91	152.42151	139.12362	113.90174	-68	8	26.0
194 BC	-193	3	9.53874	1650632.03874	0.9775645	0.9615623	128.26	152.53233	139.11327	113.93442	-193	3	9.0
322 BC	-321	9	27.65803	1604082.15803	0.9710275	0.9619826	129.09	152.46289	139.03279	114.03470	-321	9	27.0
447 BC	-446	6	2.14601	1558308.64601	0.9833087	0.9611945	127.56	152.41816	139.03830	113.96947	-446	6	2.0
574 BC	-573	8	1.41288	1511981.91288	0.9794732	0.9617904	129.79	152.53682	139.06154	113.85545	-573	8	1.0
703 BC	-702	4	3.28685	1464744.78685	0.9729864	0.9624775	132.05	152.53402	139.08842	113.82023	-702	4	3.0
Mean values					0.975	0.962	129.97	152.7	139.3	113.8			

(1737-703 B.C.)

attained by the gas (H_2O) is equal to around 0.86 km s^{-1}.

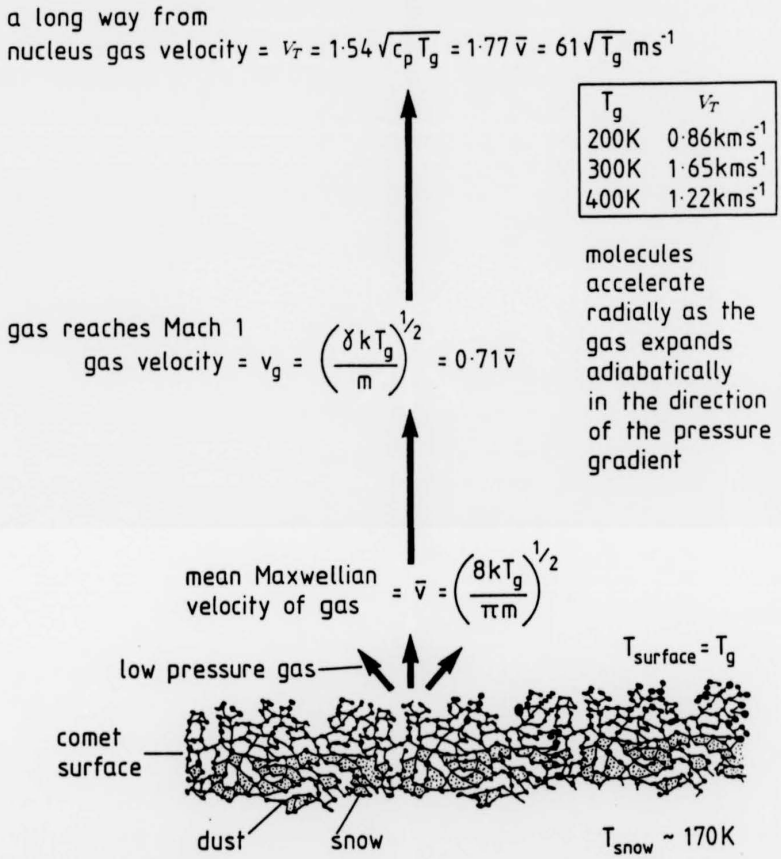

Figure 4.2: A schematic diagram showing how the subliming gas molecules accelerate away from the nucleus surface in the direction of the pressure gradient.

The pressure exerted by this gas not only breaks up the fragile surface dust layers of the cometary nucleus but also, by momentum transfer, accelerates the meteoroid dust particles radially away from the nucleus surface. Note from the previous chapter that this meteoroid ejection velocity is *independent* of the mass of the meteoroids in the mass range covered by the data being used. The meteoroid ejection velocity is thus a function of the radial gas velocity and not the meteoroid size. The perceived mass versus semi-major axis distributions shown in Fig. 3.7 are therefore due to the fact that there are many more low mass meteoroids than high mass ones.

The formation of the Perseid meteoroid stream is illustrated schematically in Fig. 4.3. The actual shape of the nucleus of P/Swift-Tuttle is unknown but it can be thought to have

an equivalent radius of 9 km. (This is the radius of a sphere that has the same surface area). Start by assuming that the radial gas flow has a constant velocity of 0.86 km s^{-1} (equal to the gas terminal velocity, V_T) and that *all* meteoroids, independent of mass, are also ejected from the nucleus with a velocity, V_∞, of 0.86 km s^{-1}, i.e. it is assumed that the meteoroids are accelerated up to 100 % of the gas velocity (note that this velocity is over five times that predicted by the 'Whipple Formula' for a Perseid meteoroid with a radius of 0.05 cm and a density of 0.29 g cm^{-3} [see equation 3.1]). Also assume that emission occurs at perihelion, where cometary activity is generally at a maximum. At perihelion the comet is moving with a heliocentric velocity V_C given by

$$V_C^2 = GM_0(\frac{2}{q_C} - \frac{1}{a_C}) \tag{4.1}$$

where G is the universal constant of gravitation, M_0 is the mass of the Sun, and q_C and a_C are the perihelion distance and semi-major axis of the comet respectively. (For P/Swift-Tuttle the mean values of q_C = 0.975 AU and a_C = 25.6579 AU have been used. These values were obtained by averaging the orbits of the 20 apparitions prior to the perihelion passage of 1862 (see Table 4.1). This gives a V_C of 42.2447 km s^{-1}). Let each meteoroid be emitted from the nucleus at an angle α to the comet-Sun line (see Fig. 4.3). It will then have a heliocentric velocity, V_m, given by

$$V_m^2 = V_C^2 + V_\infty^2 - 2V_C V_\infty \cos(90 - \alpha) \tag{4.2}$$

If the heliocentric velocity, V_m, and the heliocentric distance at emission, r, are known then the semi-major axis of the meteoroid's orbit, a_m, is given by

$$\frac{1}{a_m} = \frac{2}{r} - \frac{V_m^2}{GM_0} \tag{4.3}$$

The semi-major axis of the orbit is independent of the direction of the heliocentric velocity vector and depends only on the magnitude of the velocity (see Roy, 1982).

The variation of a_m with α (for perihelion emission at a constant velocity of 0.86 km s^{-1}) is shown in Fig. 4.3. Meteoroids with a_m less than 25.66 AU will have orbital periods less than that of the comet. They will therefore return to their perihelia sooner than the comet returns to its perihelion. Thus they will progressively move further and further ahead of the cometary nucleus, around the mean stream orbit. Meteoroids with a_m greater than the comet's will progressively fall behind the cometary nucleus. The large range of orbital semi-major axes leads to an even larger range of orbital periods. Think of the progress made by the meteoroids emitted at a specific perihelion passage. After about 250 years, nearly two orbital periods of the comet, meteoroids emitted originally at angles α of -90, -50, -30 and -10° will have orbited 10.42, 8.0, 5.56 and 3.0 times. It is clear that a complete stream of meteoroids is quickly established around the cometary orbit and the annual flux at Earth quickly reaches a constant value.

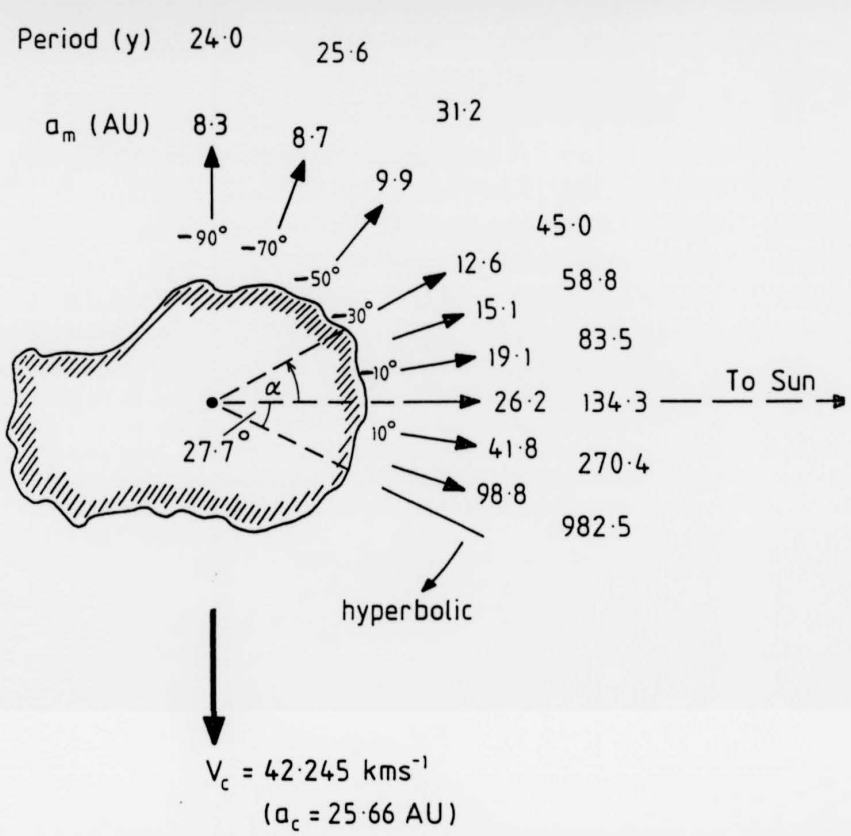

Figure 4.3: A schematic diagram showing the formation of a section of the Perseid meteoroid stream. For simplicity the nucleus of comet P/Swift-Tuttle is assumed to be at perihelion. If meteoroid dust is ejected from the nucleus at a constant cometocentric velocity of 0.86 km s^{-1} in the direction of the arrows the meteoroids move off on to orbits with the semi-major axes and periods indicated. All 'perihelion' meteoroids emitted with $\alpha > 27.7°$ move off on hyperbolic orbits.

At perihelion (0.975 AU from the Sun) comet P/Swift-Tuttle is moving at a heliocentric velocity of 42.245 km s^{-1}. This is only 0.414 km s^{-1} below the 'parabolic' velocity at that distance (42.65936 km s^{-1}). If the meteoroids are ejected from the nucleus of the comet with a velocity of 0.86 km s^{-1} it is quite clear that many will find themselves on hyperbolic orbits and as such will leave the solar system altogether. In the case of Fig. 4.3, meteoroids ejected at angles $\alpha >$ 27.7° (in the direction of comet orbital motion) will move off on hyperbolic orbits.

To model the formation of the Perseid meteoroid stream we have to estimate how the number of emitted meteoroids varies as a function of α. This depends on the spin axis orientation and on the spin direction. The latter introduces a lag angle α_L. The sub-solar point is probably the region of the nucleus having the maximum surface temperature but the cometary snow is expected to be a centimetre or so beneath a surface dust layer (see Hughes,

1986). Heat takes a finite time to pass through this dust and thus the maximum snow sublimation rate is expected to occur at an angle α_L, this angle being positive or negative depending on the spin mode of the cometary nucleus. A simple weighting function can be introduced by assuming that the emission varies as a function of $\cos(\alpha + \alpha_L)$. If $\alpha_L = 0°$ this enhances emission from the sub-solar point and gives no emission from the 'night' side of the comet.

With a simple cosine emission function, a zero lag angle, a constant gas velocity of 0.86 km s^{-1} and a consequent meteoroid ejection velocity of 0.86 km s^{-1} and emission only at perihelion, one finds that 26.7 % of the meteoroids are emitted onto hyperbolic orbits. For values of α_L equal to -30, -20, -10, +10, +20 and +30° the percentage of hyperbolic meteoroids becomes 7.7, 13.0, 19.4, 34.8, 43.3 and 52.0 respectively.

4.3 The semi-major axis distribution

The distribution of observed Perseid semi-major axes, a, is shown in Fig. 4.4 as a function of both $(1/a)$ and a. Remember that an observer measures the upper-atmosphere velocity of the ablating meteoroid and this is then converted into the out-of-atmosphere velocity that the causative meteoroid would have had if it had not been accelerated by the Earth's gravitational field. The latter velocity is directly related to $(1/a)^{0.5}$ (see equation 4.3). Fig. 4.4(c) shows a running-three-mean smoothed version of Fig. 4.4(b).

The distribution of $1/a$ contains all the 205 CPPs. It is quasi-gaussian, peaking at $1/a = 0.034$ AU^{-1}, the standard deviation of the data set being 0.05 AU^{-1}. The histograms of number versus semi-major axis (see Fig. 4.4) have abscissae that only have a range $0 < a < 50$ AU. All meteoroids with $1/a < 0.02$ are thus omitted, leaving 122 meteors in all. This group can be quantified by noting that there are no meteoroid orbits with $a < 6.25$ AU, the most probable semi-major axis is 12.7 ± 0.5 AU, and the central 64% of the 122 meteoroids have $11 < a < 27$ AU.

The presently observed semi-major axis distribution is assumed here to be a direct result of cometary meteoroid ejection and not due to subsequent perturbation effects. The 'Whipple Formula' for cometary meteoroid ejection (see equation 3.1) results in a cometocentric dust ejection velocity of around 0.05 km s^{-1}, for an 'average' photographic Perseid meteoroid. The resulting semi-major axis distribution for a modal ejection velocity of 0.05 km s^{-1} is shown in Fig. 4.5. The low dust ejection velocities produce a semi-major axis distribution with $20 < a < 38$ AU with a peak that coincides with that of the parent comet at around 26.58 AU. The mean semi-major axis is 26.72 AU. Considering the relative orbital semi-major axis stability of the parent comet and therefore also the mean orbit of the stream, it is difficult to imagine the evolution of this semi-major axis distribution into the observed distribution shown in Fig. 4.4(c) due to orbital perturbations alone, especially the evolution of the peak from 26.58 AU to around 13 AU (a 50 % change in the original value).

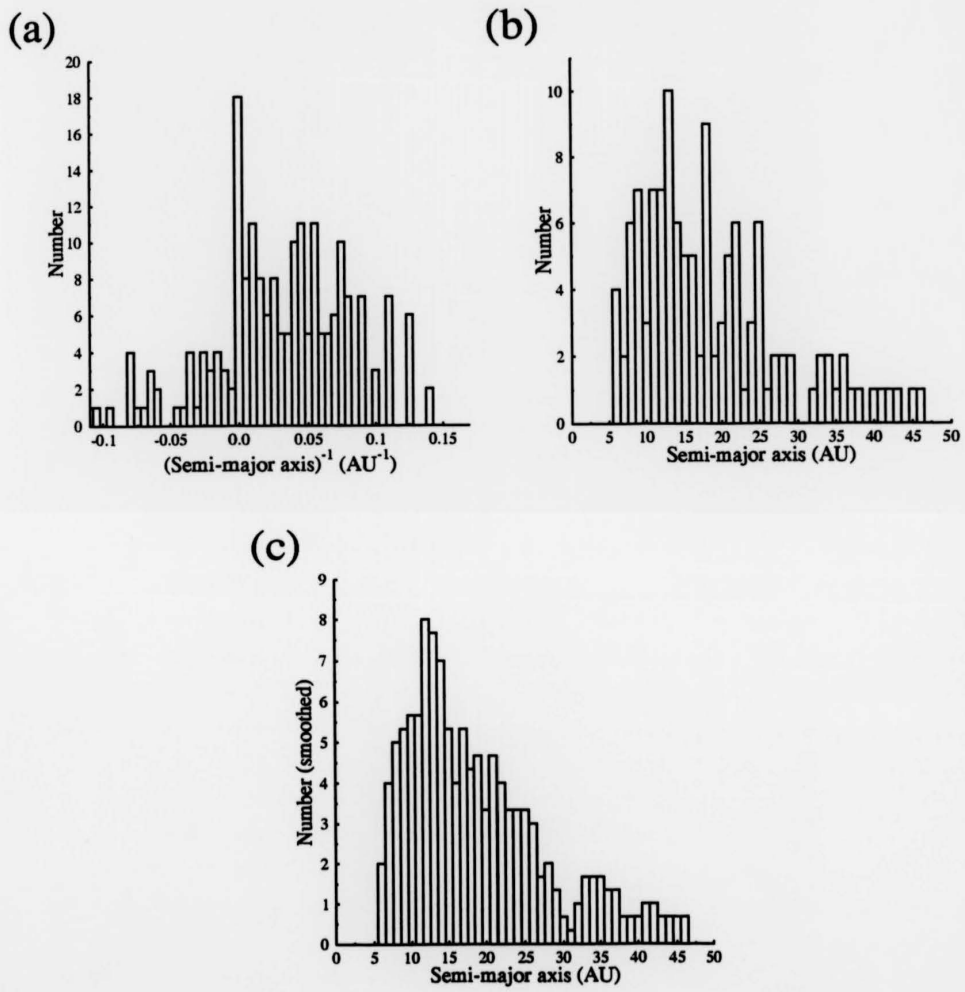

Figure 4.4: The observed semi-major axis distribution of photographic Perseid meteoroids. The histograms are plotted as a function of (a) $1/a$ and (b) a. Histogram (c) is a running-three-mean smoothed version of histogram (b).

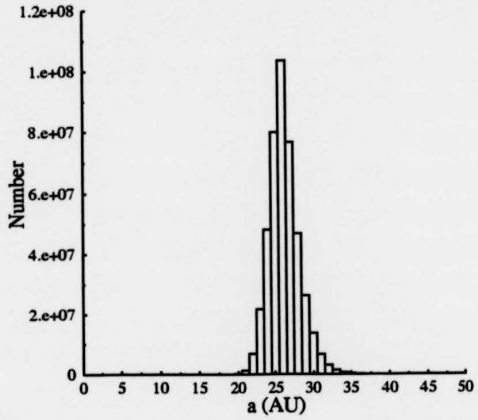

Figure 4.5: The histogram has been produced by modelling the emission of meteoroids from the nucleus of P/Swift-Tuttle assuming a modal ejection velocity of 0.05 km s^{-1}. Meteoroids have been ejected in all Sun-ward directions, with most ejection taking place at perihelion directly towards the Sun.

Williams, Murray and Hughes (1979) have modelled the effects of planetary perturbations on the orbits of 10 'test' Quadrantid meteoroids over a time period of 4500 years (approximately 840 meteoroid orbital periods). It was found that the semi-major axis varied very little from its original value with the exception of one meteoroid which was 'lost' from the stream after a close encounter with Jupiter. In other words, planetary perturbations have only amounted to a 0.3 % increase in the semi-major axis over 840 meteoroid orbits. Jones and Wheaton (1985) have investigated the dispersion of the Geminid stream resulting from planetary perturbations. The orbits of seven meteoroids were integrated for 2000 years into the future (corresponding to approximately 1200 orbital periods) using a fourth-order Runge-Kutta technique in much the same way as Williams, Murray and Hughes (1979) performed for the Quadrantids. The results showed that there was only a 0.00059 AU decrease in the mean semi-major axis, corresponding to a 0.04 % change in the original value, over 1200 meteoroid orbital periods. Similarly, Fox, Williams and Hughes (1981) evaluated the orbital evolution of the mean Geminid orbit using the Gauss-Jackson technique. A linear regression analysis was applied to the orbital parameter variations and the equation relating to the evolution of semi-major axis was given as

$$a = 1.35 - (5.9 \times 10^{-6})t \tag{4.4}$$

where t is the evolution time in years. Inserting $t = 2000$ years into equation 4.4 results in a mean semi-major axis decrease of 0.0118 AU. This is equivalent to a change of 0.84 % of the original value.

It is evident that long-term planetary perturbations do not explain the width and profile of the Perseid meteoroid semi-major axis distribution. This means that the observed semi-major axis distribution must be close to the original distribution produced during cometary dust ejection. Whipple's gas dynamic drag equation (3.1) does not provide a sufficiently high meteoroid ejection velocity to account for the observed semi-major axis distribution. In order to produce the observations we must increase the meteoroid cometocentric ejection velocity by a factor of at least twelve, i.e. up to a mean velocity of around 0.6 km s^{-1}.

As there is no variation in the semi-major axis distribution with the longitude of ascending node of the meteoroid orbit then the observed semi-major axis distribution *is* representative of the stream as a whole and not just those meteoroids that happen to intersect the Earth's orbit.

The expected meteoroid semi-major axis distribution has been modelled in the following ways. First the distribution given in Fig. 4.6(a) has been obtained by assuming that (i) the mass loss occurs *only* at perihelion, (ii) meteoroids are only emitted on the Sun-ward side of the cometary nucleus (iii) meteoroids are ejected at specific α values only, these being separated by increments of 1° (see Fig. 4.3) and the number emitted in each 1° increment is proportional to $\cos(\alpha)$ (the comet-Sun radius vector corresponds to $\alpha = 0°$), (iv) the meteoroid cometocentric velocity when away from the nucleus is equal to the radial gas velocity and is constant and has a value of 0.86 km s^{-1} and (v) the lag angle α_L is zero.

A comparison between the observed distribution in Fig. 4.4(c) and the first modelled distribution in Fig. 4.6(a) indicates that the latter rises too sharply to the most probable semi-major axis value and that the magnitude of the most probable semi-major axis obtained by the model is too low.

The second distribution given in Fig. 4.6(b) has been obtained by changing condition (i) above. Emission is now assumed to only occur *before* perihelion passage. Emission is taken to start at a heliocentric distance of $r = 2.9$ AU (the heliocentric distance at which water ice is assumed to begin sublimating). The amount of emission per unit of true anomaly angle is weighted according to r^{-2}. The gas pressure at the nucleus surface depends on the amount of absorbed solar radiation, so gas and dust emission is typically proportional to r^{-2} and most sublimation therefore takes place close to perihelion.

To obtain the third distribution, Fig. 4.6(c), condition (i) is changed so that emission only now occurs *post*-perihelion, the weighting being the same as in the Fig. 4.6(b) case. The major difference between histograms (c) and (b) is due to the orientation of the emission surface with respect to the direction of comet orbital motion. A larger number of meteoroids are ejected in the 'forward' direction during the pre-perihelion part of the orbit than during the post-perihelion part of the orbit. This produces a larger number of hyperbolic orbits and a corresponding reduction of the number of orbits with $a < 25$ AU. Likewise a larger number of the meteoroids are ejected in the 'reverse' direction during the post-perihelion part of the orbit, explaining the sharp peak at low semi-major axis values ($a < 13$ AU) as seen in Fig.

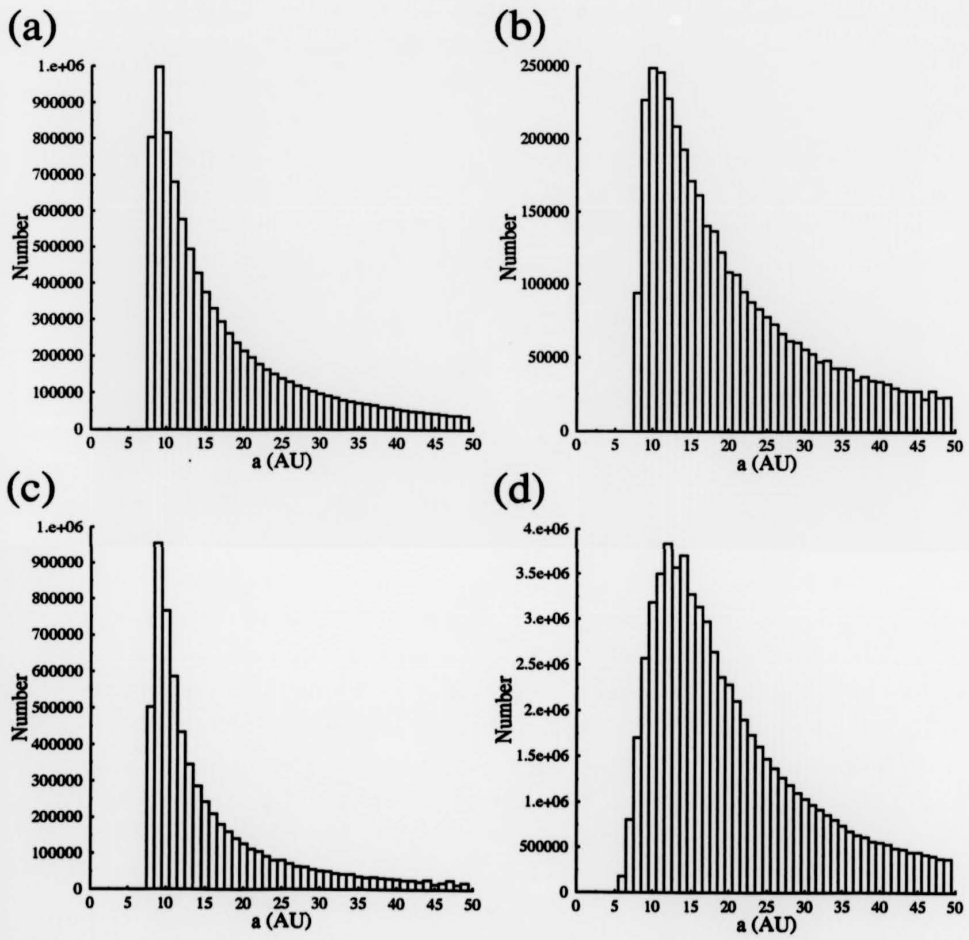

Figure 4.6: The modelled distribution of meteoroid semi-major axes that could be produced by the decay of P/Swift-Tuttle. The decay is assumed to occur on the Sun-ward side of the cometary nucleus (a) at perihelion, (b) pre-perihelion, (c) post-perihelion and (d) both pre- and post-perihelion. In (a, b & c) the meteoroids have a constant cometocentric emission velocity of 0.86 km s^{-1}. In (d) the emission has a Maxwellian velocity distribution that maximises at a mean velocity of 0.6 km s^{-1}.

4.6(c). As a result of the increased number of hyperbolic orbits that are produced during the pre-perihelion emission period, a greater number of *stream* meteoroids are produced in the post-perihelion phase. This is confirmed by the values on the ordinate scales of the histograms 4.6(b) and 4.6(c).

To obtain the fourth distribution, Fig. 4.6(d), condition (i) has been changed to include both pre- *and* post-perihelion emission and in both cases the rate of emission is put proportional to r^{-2}. Condition (iv) is also changed. The gas terminal velocity, $\overline{V}_T$, used in cases (a) to (c) is for an adiabatically expanding gas. In reality the thermal energy of the gas will be changed slightly by various sources and sinks of heat in the cometary coma (see Delsemme, 1982). The true mean terminal velocity, $\overline{v}_t$, of the gas is thus given by

$$\overline{v}_t = V_0 r^{-0.5} \quad .$$

Observations of the rate of water gas expansions in cometary comae, as a function of heliocentric distance, have confirmed this theoretical relationship and the value of V_0 is found to be around 0.58. The mean radial velocity of water gas, in km s^{-1}, is therefore given by

$$\overline{v}_{H_2O} = 0.58 r^{-0.5} \tag{4.5}$$

where r is in AU. This corresponds to a velocity of 0.58 km s^{-1} at a heliocentric distance of 1.0 AU. At the assumed perihelion distance of P/Swift-Tuttle (0.975 AU), where most emission takes place, equation 4.5 predicts a mean gas radial velocity of around 0.6 km s^{-1}. To produce the fourth distribution the modelled gas flow has a Maxwell Boltzmann velocity distribution that peaks at a velocity of 0.6 km s^{-1}. It is still assumed that meteoroids are emitted with velocities that are independent of meteoroid mass and are equal to the radial gas velocities, i.e. meteoroids are also emitted with a Maxwell Boltzmann velocity distribution that peaks at a mean velocity of 0.6 km s^{-1}.

A comparison between Fig. 4.6(d) and Fig. 4.4(c) indicates that the model is now producing a histogram that reasonably fits the observations. The assumption that the ejected meteoroids attain velocities comparable to the radial gas velocities thus seems reasonable. In order for this to be achieved the meteoroid surface area to mass ratio must be high. The proportion of hyperbolic meteoroid orbits produced in each of cases (a), (b), (c) and (d) are 26.7 %, 40.2 %, 13.0 % and 16.4 % respectively.

Fig. 4.7 shows how the peak positions and the distribution widths of the modelled meteoroid orbital semi-major axis distributions change as a function of the mean meteoroid ejection velocity. Histograms (a) to (e) correspond to mean ejection velocities of 0.4, 0.5, 0.6, 0.7 and 0.8 km s^{-1} respectively. The observed core Perseids are characterised by a semi-major axis distribution that peaks at (12.7 ± 0.5) AU, has a width at half maximum of (13 ± 1) AU and has a minimum value of 6.26 AU. This observation restricts the mean ejection velocity, to a narrow range of values, this being $0.56 \leq \overline{V} \leq 0.65$ km s^{-1} ($\sim 0.6 \pm 0.05$ km s^{-1}).

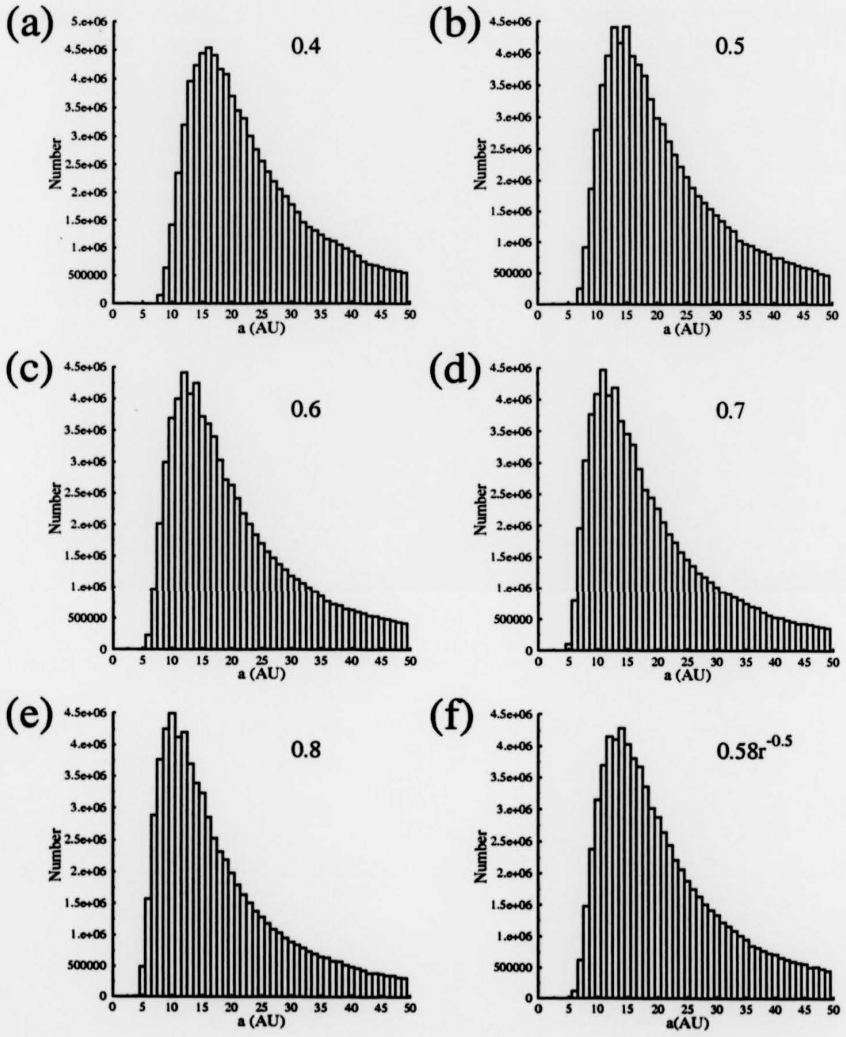

Figure 4.7: The histograms show how the modelled meteoroid semi-major axis distribution varies with mean meteoroid ejection velocity. Histograms (a) to (e) correspond to mean ejection velocities of 0.4, 0.5, 0.6, 0.7 and 0.8 km s^{-1} respectively. Histogram (f) shows the modelled semi-major axis distribution for a mean ejection velocity that changes as a function of heliocentric distance according to equation 4.5.

Histogram (f) (Fig. 4.7) gives the semi-major axis distribution that is produced using a mean ejection velocity that varies with heliocentric distance according to equation 4.5 i.e. the mean ejection velocity will be at a maximum (0.587 km s^{-1}) at perihelion (0.975 AU) and at a minimum around 2.9 AU ($\sim$ 0.34 km s^{-1}). Histogram (f) shows the significance of the $\frac{1}{r^2}$ activity parameter which has the effect of producing around 9 times more dust per unit time at perihelion than at 2.9 AU. This ensures that much of the dust is ejected with higher ejection velocities ($>$ 0.5 km s^{-1}) and the resulting semi-major axis distribution is similar to Figs. 4.7(b) and (c). The r^{-2} emission function could be adjusted so that the relationship either weakens to $r^{-1.5}$ or strengthens to r^{-3} and beyond. Mobberley (1994) found that comet P/Swift-Tuttle followed an $r^{-5.2}$ activity relationship during the 1992 perihelion passage. An activity factor such as this would produce nearly 300 times more dust per unit time at perihelion than at 2.9 AU, rendering pre- and post- perihelion emission a long way from perihelion fairly insignificant.

Notice that including both pre- and post-perihelion emission in case (d) is tantamount to assuming that the mass loss from the comet and thus its heliocentric magnitude varies symmetrically with respect to perihelion. This is reasonable. Green (1993) wrote, 'the post-perihelion brightness of P/Swift-Tuttle appears to be fairly symmetrical with its pre-perihelion light-curve'. Mobberley (1994) indicated the pre-perihelion light-curve followed

$$M_V - 5\log\Delta = 4.56 + 18.95\log r$$

where Δ is the comet-Earth distance in AU. During post-perihelion the light-curve was found to be

$$M_V - 5\log\Delta = (4.6 \pm 0.3) + (16.8 \pm 0.5)\log r \quad .$$

According to Mobberley, therefore, the comet is somewhat brighter after perihelion than before perihelion. Bortle (1993) concluded, however, that a pre-perihelion law of

$$M_V - 5\log\Delta = 4.5 + 15\log r$$

was followed by a post-perihelion law of

$$M_V - 5\log\Delta = 4.45 + 17.4\log r \quad .$$

This indicates the opposite trend to that found by Mobberley.

Notice also that the semi-major axis distributions given in Fig. 4.6 have been obtained by assuming a zero lag angle, i.e. that the emission occurs symmetrically around the sub-solar point. The fact that Fig. 4.6(d) and Fig. 4.4(c) are in general agreement indicates that this assumption is reasonably valid. So the dust emission by comet P/Swift-Tuttle is not greatly effected by the nucleus spin mode. Two possible explanations are

(i) the comet is spinning ***slowly*** about an axis that is approximately perpendicular to the orbital plane. Thus the nucleus only spins through a few degrees ($<$ 10°) in the time that

it takes the sub-solar heat pulse to travel from the surface of the nucleus to the underlying snows.

(ii) the nucleus is spinning about an axis that is approximately in the orbital plane and is pointing approximately along the perihelion-Sun line.

Explanation (i) is the most likely. Boswell and Hughes (1992) indicated that around 75 % of known comets exhibit brightness profiles that are symmetrical with respect to perihelion passage. An explanation for this is that as comets evolve and lose mass their spin axes tend to orientate themselves so that they are normal to the comet's orbital plane. Sekanina (1981) derived a *prograde* rotation period of around 66.5 hr. (2.77 days) for the nucleus of P/Swift-Tuttle by examining the dynamical evolution of jet structures exhibited by the 1862 apparition of the comet. He also established that the spin axis made an angle of around 60° with the direction to the Sun, at perihelion.

The work above can be extended slightly by plotting the semi-major axis distribution as a function of the lag angle, again assuming that emission is symmetrical with respect to perihelion. These plots are shown in Fig. 4.8. One can see how the modelled semi-major axis distribution peak and the ordinate magnitude changes for various lag angles. Negative lag angles (here defined as prograde nucleus rotation) result in more meteoroids being ejected in the 'reverse' direction with respect to the direction of parent comet motion and hence more low semi-major axis meteoroids are produced ($a < 25$ AU). Positive lag angles (retrograde nucleus rotation) result in fewer meteoroids being produced in the 'reverse' direction with a consequent reduction in the peak ordinate magnitude and a shift in the peak abscissa value to $a > 12$ AU. The higher proportion of dust ejection in the 'forward' sense also adds to the stream mass loss due to increased hyperbolic meteoroid production.

Only the low positive or low negative lag angle scenario is realistic. This would result in nucleus activity being reasonably symmetrical about the comet-Sun radius vector ($\alpha = 0°$). A consequence of this is the cancellation of any significant differential gas-jetting effects that could cause non-gravitational changes in the comet's orbit. This conclusion is supported by Yau et al. (1994) who compared a backwards integration of the orbit of P/Swift-Tuttle with observations of the comet. They concluded that the non-gravitational forces that affect the motion of most active comets appear to be negligible for comet P/Swift-Tuttle. (Similar results were found by Marsden et al., 1993). Comet P/Halley experiences an increase in its orbital period of around 4 days per revolution due to non-gravitational forces. Yau et al. suggested that either

(i) comet P/Swift-Tuttle outgasses *radially* toward the Sun and in a symmetric fashion about perihelion and/or

(ii) the nucleus of P/Swift-Tuttle is far more massive than periodic comets of comparable activity such as P/Halley.

If the mass of P/Swift-Tuttle were significantly larger than calculations would have us believe, then one would not expect to be able to detect any non-gravitational acceleration in its orbital

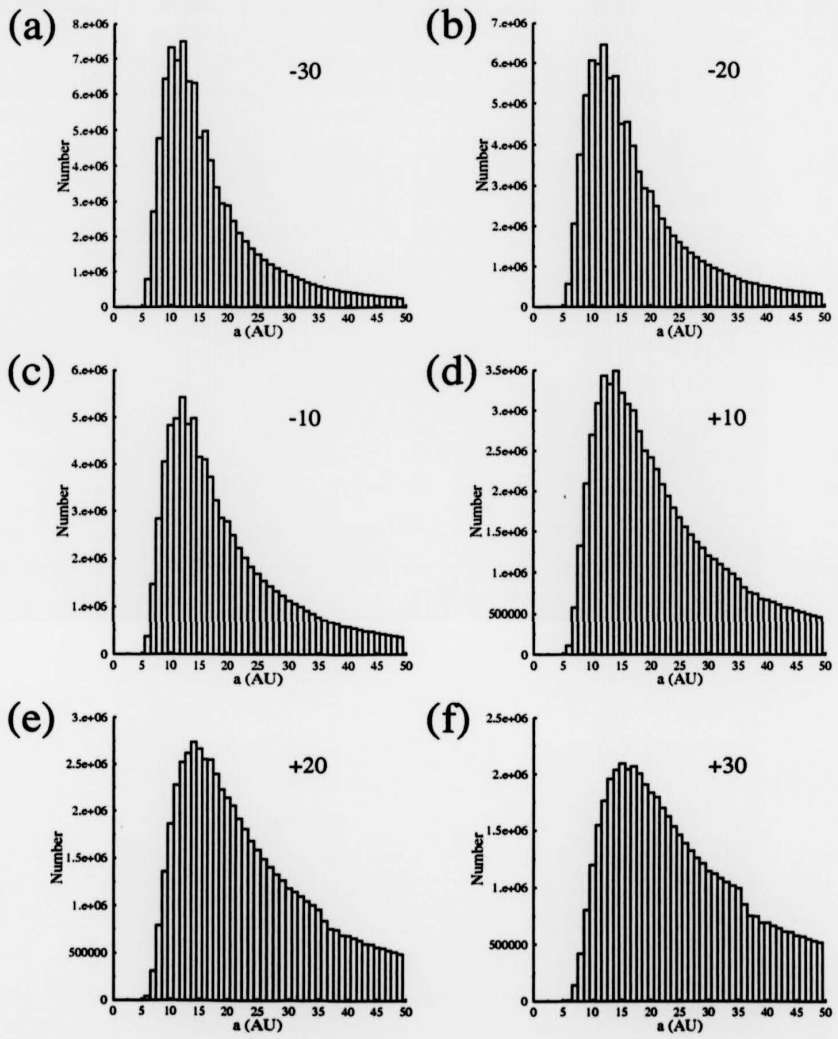

Figure 4.8: Histograms (a) to (f) correspond to the modelled distribution of meteoroid semi-major axes produced with lag angles, α_L, of $-30°$, $-20°$, $-10°$, $+10°$, $+20°$ and $+30°$ respectively. The emission conditions are otherwise the same as those that produced Fig. 4.6(d). Negative lag angles (prograde nucleus rotation) result in a higher proportion of meteoroids being ejected in the 'reverse' direction with respect to the direction of parent comet orbital motion and hence a higher proportion of low semi-major axis orbits ($a < 25$ AU) are produced. Conversely, positive lag angles (retrograde nucleus rotation) result in a lower proportion of meteoroids being ejected in the 'reverse' direction with a consequent reduction in the peak ordinate magnitude and a shift in the peak abscissa value to $a > 12$ AU.

motion.

For case (i) to be valid, the rotation axis and the size and location of the active regions on the cometary nucleus would have to be constant over the whole period of orbital observation covered by Yau et al.

For lag angles, α_L, of $-30°$, $-20°$, $-10°$, $0°$, $+10°$, $+20°$ and $+30°$ the curves in Fig. 4.8 maximise at 11.6, 12.1, 12.4, 13.0, 13.6, 14.6 and 16.2 AU respectively. Also the widths of the curves at half maximum are 10.1, 10.6, 11.6, 13.4, 15.7, 18.2 and 23.2 AU respectively. Fig. 4.9 shows a plot of semi-major axis, a AU, against lag angle, α_L, for the curves shown in Fig. 4.8. The circular points correspond to the semi-major axis curve maxima for various lag angles and the square points correspond to the semi-major axis width at half maximum for various lag angles. The observed Perseid semi-major axis distribution [Fig. 4.4(c)] maximises at about (12.7±0.5) AU and has a width at half maximum of around (13±1) AU. Interpolating these data into the curves plotted in Fig. 4.9 indicates that the lag angle of P/Swift-Tuttle is $-5° \pm 10°$ ($-15° \leq \alpha_L \leq +5°$). The inference from this is that the comet spins *slowly* in a *prograde* mode. This leads to the conclusion that around 14 % of the dust particles lost by the comet are forced onto hyperbolic orbits and are thus expelled from the solar system. (This hyperbolic fraction increases to around 16 % if the lag angle is assumed to be zero [see Fig. 4.6(d)]).

4.3.1 The perihelion distance distribution

In section 3.2.3 it was concluded that the mean perihelion distance of the observed Perseids is not the same as the mean perihelion distance of the Perseid stream, whereas the mean observed values of the semi-major axis, eccentricity and inclination do apply to the stream in general. The modelled meteoroid eccentricity is found by using the equation

$$e = \left[1 - \frac{r}{a^2}(2a - r)\sin^2\phi\right]^{\frac{1}{2}} \tag{4.6}$$

where r is the heliocentric distance of emission and ϕ is the angle between the meteoroid heliocentric velocity vector and the radius vector of the ejected meteoroid (Roy, 1978). As the observed range of Perseid meteoroid perihelion distances depends on the Solar longitude, the modelled perihelion distance distribution should therefore differ from the observed Perseid perihelion distance distribution.

The modelled perihelion distance distribution is shown in Fig. 4.10(a). Over the last twenty or so apparitions $q_{Swift-Tuttle} \simeq 0.975$ AU (see Table 4.1). When we look at the observed Perseids they have a mean perihelion distance, q_{Pers}, of 0.949 AU which is considerably smaller than that of the parent comet over recent history. The histogram in Fig. 4.10(a) is reasonably symmetrical whereas the histogram of observed perihelia (see Fig. 3.3) is not. This probably indicates that we are not sampling the whole stream from Earth. This would indicate that Earth-based estimates of the mass of the stream are probably too low.

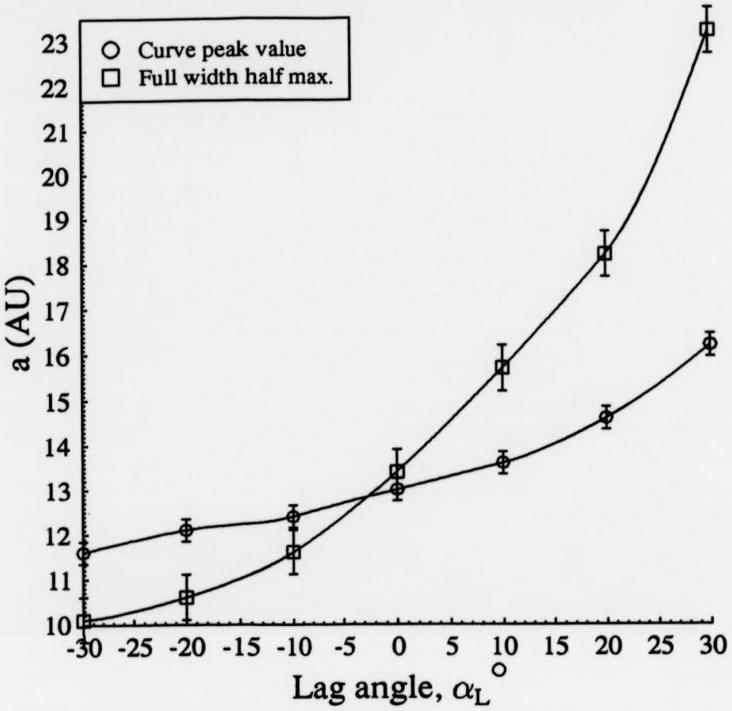

Figure 4.9: The distribution maxima and widths at half maximum for each of the plots in Fig. 4.8 have been plotted against lag angle, α_L. Points have also been plotted for the $\alpha_L = 0°$ case (Fig. 4.6(d). By interpolating the values for the observed Perseid semi-major axis distribution [Fig. 4.4(c)] into the above curves we can deduce that the lag angle of P/Swift-Tuttle is around $-5°$.

Fig. 4.10(b) shows the perihelion distribution of a modelled two-dimensional meteoroid stream that now has a parent comet with a perihelion distance of 0.955 AU (a value close to that of the present-day P/Swift-Tuttle) and a semi-major axis of 25.6579 AU, the same as before. The shape of the histogram is similar to that shown in Fig. 4.10(a), indicating that changing the perihelion distance of the parent comet over a limited range does not significantly effect the shape of the perihelion distance distribution of the resultant meteoroid stream about the perihelion distance of the parent comet.

4.3.2 Modelling the meteoroid angular orbital parameters

The ejection of a meteoroid at an arbitrary angle to the direction of parent comet motion, in the plane of the comet orbit, also produces a change in the meteoroid orbital argument of perihelion, as well as the semi-major axis, eccentricity and perihelion distance. In the absence of perturbative influences, the daughter meteoroid will return to the point of its emission in one meteoroid orbital period i.e. the point on the parent comet's orbit at which the meteoroid

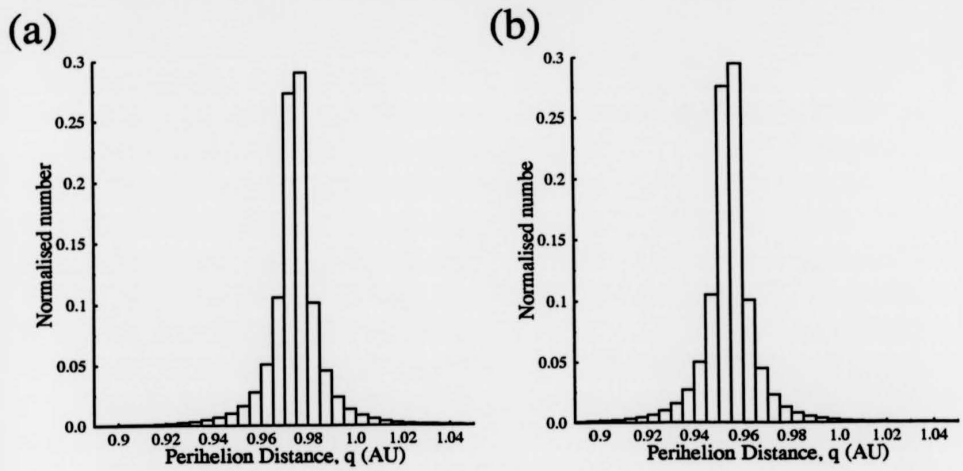

Figure 4.10: The histograms show the normalised numbers of meteoroids as a function of their perihelion distances. Histogram (a) is for a modelled meteoroid stream produced by the decay of the parent comet that has a mean perihelion distance of 0.975 AU. The emission process is the same as that in Fig. 4.6(d). Histogram (b) shows the perihelion distance distribution that is produced by meteoroid dust emission from a parent comet with a perihelion distance of 0.955 AU. The modelled emission process is the same as in the case of histogram (a).

was ejected. Knowing the heliocentric distance of the emission point and also the semi-major axis, eccentricity and perihelion distance of the parent comet and the daughter meteoroid allows us to determine the respective comet/meteoroid orbital true anomalies at this point. The change in meteoroid orbital argument of perihelion is then simply the difference between the two true anomaly values. This change may be positive or negative, depending on the angle of meteoroid ejection with respect to the direction of comet motion.

In order to model the distributions of meteoroid inclination, i, and longitude of ascending node, Ω, realistically after cometary dust ejection, we must consider the effects produced by meteoroid ejection 'above' and 'below' the parent comet's orbital plane. Following Roy (1978), the meteoroid's cometocentric velocity after ejection, $\mathbf{v}$, can be split into a component at right angles to the comet's orbital plane ($\mathbf{v}_W$) and two mutually perpendicular components lying along and at right angles to the radius vector ($\mathbf{v}_S$ and $\mathbf{v}_T$). In order to affect the inclination and the longitude of the ascending node the component $\mathbf{v}_W$ must be greater than zero. The equations that govern the change in meteoroid orbital inclination Δi and longitude of ascending node, $\Delta\Omega$ can be expressed as

$$\Delta i = \frac{r \cos u \mathbf{v}_W}{na^2\sqrt{1-e^2}} \tag{4.7}$$

$$\Delta\Omega = \frac{r \sin u \mathbf{v}_W}{na^2\sqrt{1-e^2}\sin i} \tag{4.8}$$

where $u = \theta + \omega$ (θ is the true anomaly). The appearance of θ in the calculations introduces

the phenomenon that the magnitudes and signs of the orbital changes depends on the point of meteoroid dust ejection on the parent comet's orbit. The greatest change in i is effected if meteoroid ejection takes place at one of the orbital nodes (u = 0°, 180°) (if $v_W > 0$). Conversely, the greatest change in Ω results from meteoroid ejection occurring midway between the nodes (u = 90°, 270°). Additionally, both these changes are maximum if $r = a(1 + e)$; i.e. when the comet is at aphelion. This situation will obviously not come into effect for an intermediate period comet such as P/Swift-Tuttle. The greatest change in the semi-major axis is obtained through meteoroid ejection at perihelion where the comet's heliocentric velocity is at a maximum.

4.4 The descending nodal distribution

Only those meteoroids with descending nodes that intersect the Earth's orbit can potentially be seen as Perseid meteors. To get some idea as to the way in which the influx of Perseid meteoroids varies as a function of the position of the Earth in its orbit we must first of all determine the distribution of the descending nodes of the meteoroids in the stream that has been modelled. The heliocentric distance, $r_{\mho}$, of the descending node of a meteoroid orbit is given by the equation

$$r_{\mho} = \frac{a(1 - e^2)}{1 + e\cos\theta} \tag{4.9}$$

The true anomaly, θ, of the descending node is given by $\theta = 180 - \omega$. The (x,y) ecliptic heliocentric co-ordinates of the descending node for each modelled meteoroid orbit is then calculated (see Chapter 2, equations 2.4, 2.5 and 2.6). These co-ordinates are used to produce an ecliptic contour plot showing the relative concentrations of the descending nodes of the modelled meteoroid orbits.

The resulting ecliptic 'footprint' is shown in Fig. 4.11. The x axis points in the direction of the first point of Ares and the y axis lies perpendicular to the x axis in the same plane. The Sun lies at the origin (0, 0) and the bold line represents the Earth's orbit through the stream. The columns of figures on the right of the footprint display the relative heights of each numbered contour, these heights being proportional to the number of descending nodes per unit area of the ecliptic.

It can be seen from Fig. 4.11 that the Earth passes through the 'central' concentration of meteoroid orbits around August 12 each year. The accompanying 3-D plot emphasises the central concentration of descending nodes. If this model is correct it indicates that significant Perseid activity should only be encountered between August 11 and August 13. The contour plot (Fig. 4.11) indicates that the increase to maximum activity and decrease from maximum activity is reasonably symmetrical [see the modelled activity histogram, Fig. 4.11]. This is not what is suggested by the Perseid meteoroid data extracted from the IAU Meteor Data Catalogue. This data is a collection of meteoroid orbits from a number of visual observers.

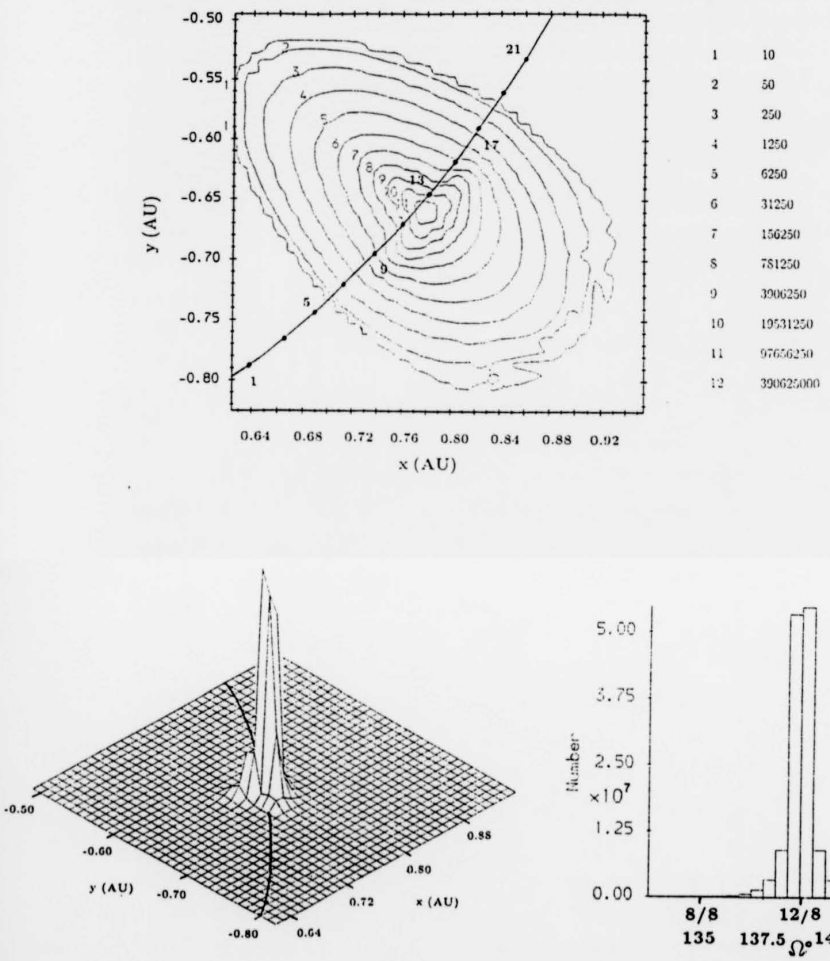

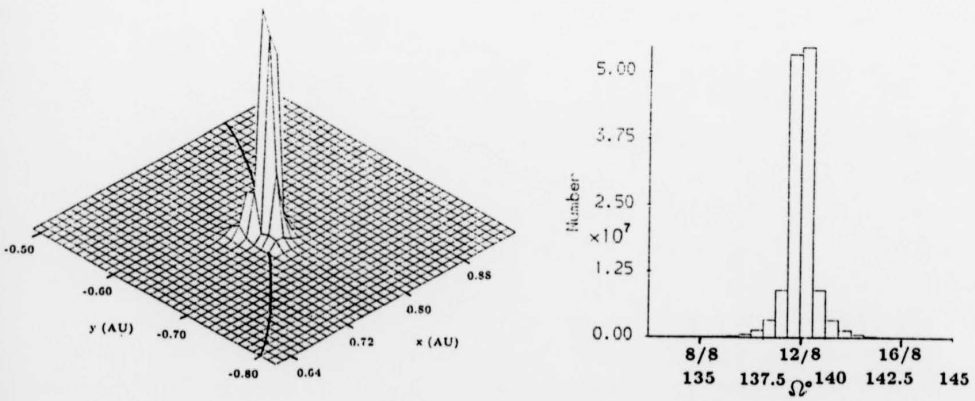

Figure 4.11: The ecliptic 'footprint' contour diagram shows the relative concentrations of the descending nodes of the modelled meteoroids produced by the decay of a comet with an orbit equal to the mean orbit given in Table 4.1. The contour 'heights' listed on the right of the plot are proportional to the number of meteoroid descending nodes per unit area. The Sun is at the origin and the x-axis points in the Sun-First Point of Aries direction. The accompanying 3-D plot shows the marked central concentration of nodes. The histogram shows the meteoroid flux to Earth which would occur as Earth moved through the contour plot. The activity is plotted as a function of the solar longitude of Earth.

The resulting activity histogram indicates that the Earth encounters a gradual, fluctuating rise to maximum Perseid activity followed by a steeper decrease [see Fig. 3.6(a)]. It takes twice as long to get from a third maximum rate to maximum rate as it does to decrease from a maximum rate down to a third maximum rate. The discrepancy between the observed activity profile in Fig. 3.6(a) and the profile predicted in Fig. 4.11 is probably due to the fact that Fig. 4.11 has been produced by modelling the dust ejection from comet P/Swift-Tuttle whilst it was travelling on a *single* specific orbit. To create a more realistic picture of the extent of the P/Swift-Tuttle dust complex we must allow for the past orbital evolution of the comet. This evolution has been caused by planetary perturbations. This will be dealt with in section 4.5.

4.4.1 The effect of cometary dust ejection velocity on the size of the ecliptic nodal footprint area

The following section investigates the outcome of varying the 'peak' meteoroid cometocentric velocity around 0.6 km s^{-1}. A major effect of increasing or decreasing the ejection velocity is to alter the semi-major axis distribution so that it diverges from the observations (see Fig. 4.7). However, the purpose of this section is to show how the ejection velocity effects the extent of the ecliptic descending nodal distribution i.e. the size of the footprint.

The modelling was repeated a further three times changing the mean Maxwellian velocity of 0.6 km s^{-1} to values of (a) 0.2, (b) 0.4 and (c) 0.8 km s^{-1}. The resulting footprints and corresponding 3-D plots are shown in Fig. 4.12. All plots have the same axis scaling as in Fig. 4.11 and the total number of ejected meteoroids is the same for each case. The effect of varying the ejection velocity is fairly evident. Reducing the ejection velocity can seriously curtail the meteor shower duration, down to only about 5 days for the case of 0.2 km s^{-1} as compared to a full duration of 12 days for the 0.6 km s^{-1} case. Conversely, increasing the ejection velocity to 0.8 km s^{-1} extends the total shower duration to 16 days.

4.5 The long-term orbital evolution of comet P/Swift-Tuttle

The previous sections have been concerned with the dust ejection and meteoroid stream formation from a single epoch in P/Swift-Tuttle's orbital history, i.e. the mean orbit of the last 20 apparitions. To create a more realistic picture of the extent of the P/Swift-Tuttle dust complex we must allow for the past orbital evolution of the comet due to gravitational perturbations.

The orbit of P/Swift-Tuttle has been integrated back in time over a period of 270,000 years taking into account the gravitational influences of the dominant perturbers, these being the planets Jupiter, Saturn, Uranus and Neptune. The way in which the orbital parameters q, a, i, ω and Ω have changed in this period is shown in Fig. 4.13 (Yau, private communication).

(a)

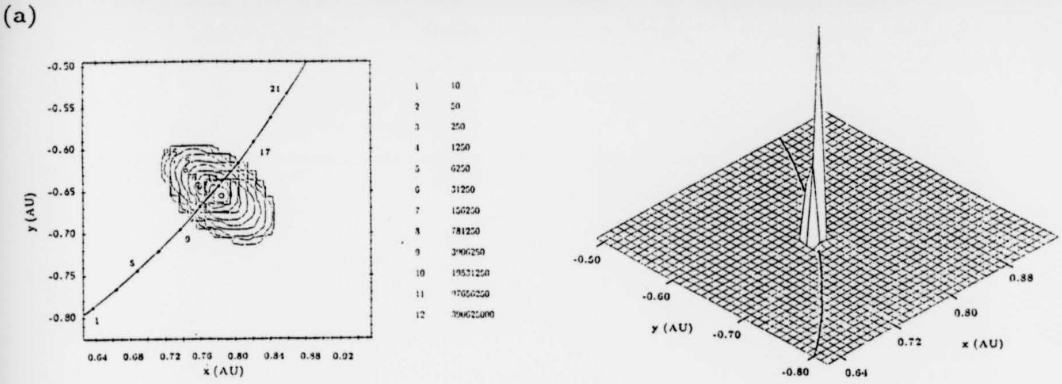

(b)

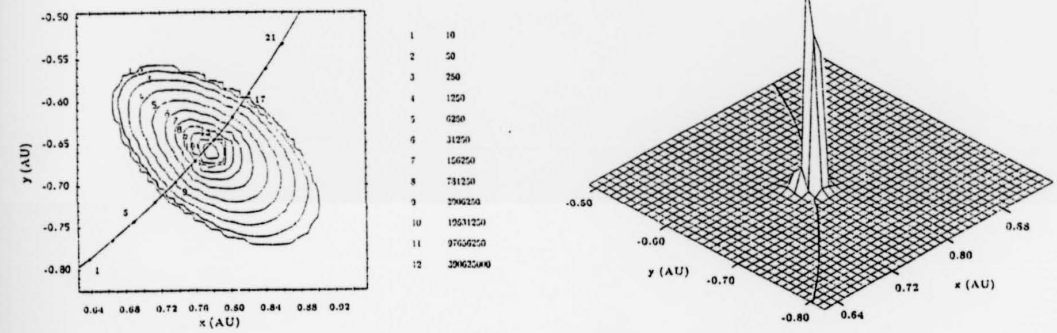

(c)

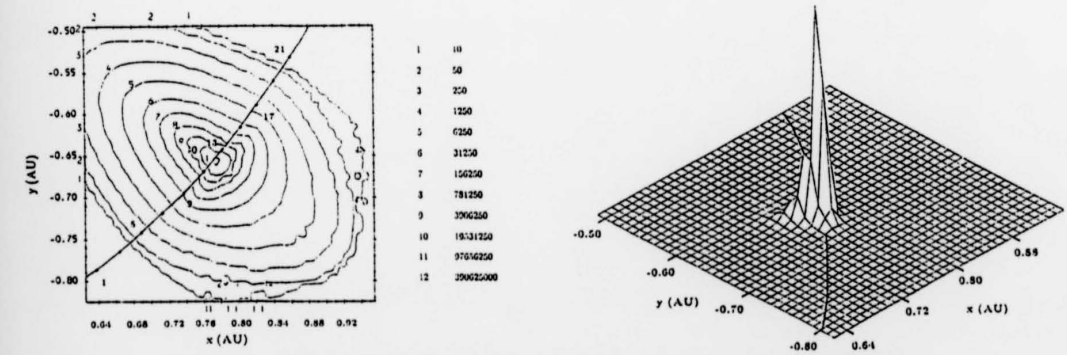

Figure 4.12: The three pairs of diagrams have been produced using the same process as in Fig. 4.11 but with the mean ejection velocity of 0.6 km s^{-1} being replaced by (a) 0.2, (b) 0.4 and (c) 0.8 km s^{-1}. The axis scales and orientations are also identical to those of Fig. 4.11, as are the contour heights.

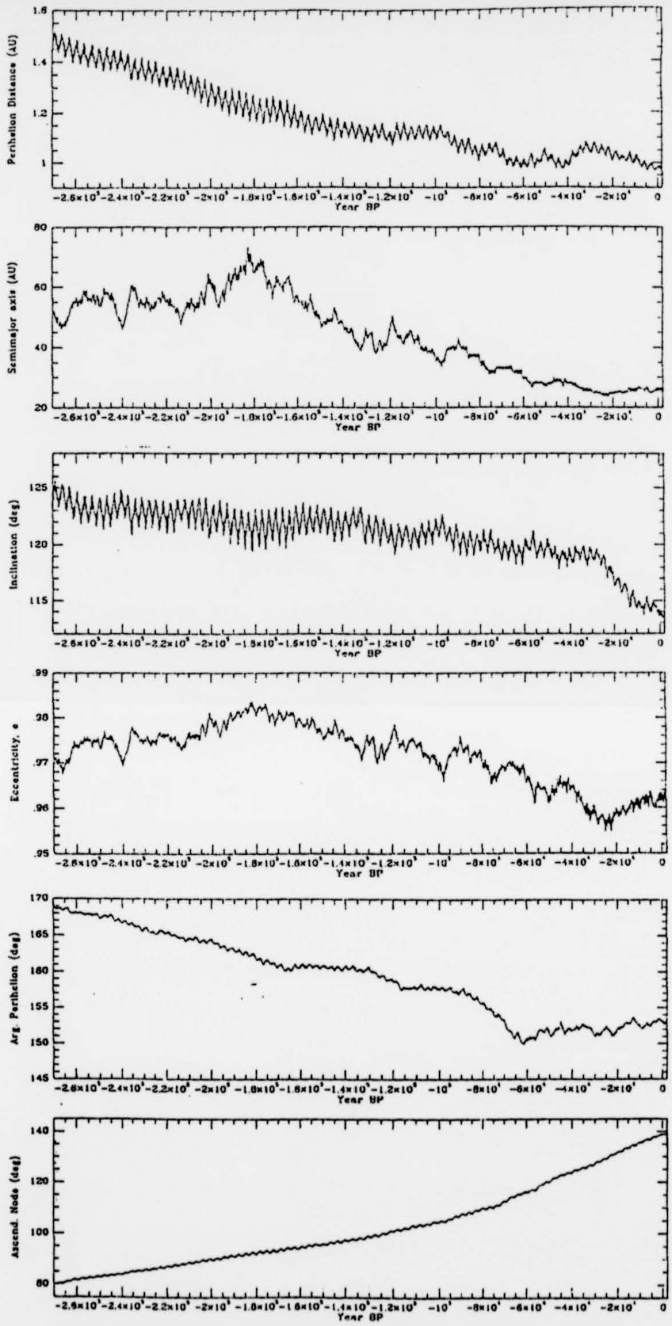

Figure 4.13: The orbit of P/Swift-Tuttle has been integrated back in time over a period of 270,000 years. The plots show how the orbital parameters q, a, i, ω and Ω have changed in this period due to the gravitational influences of Jupiter, Saturn, Uranus and Neptune.

It can be seen that the perihelion distance of P/Swift-Tuttle remained close to the current value for at least the last 70,000 years and at no point during the past 270,000 years of orbital integration did the comet's perihelion distance approach today's observed Perseid mean value of 0.949 AU. When modelling the orbital perihelion distance distribution of the Perseid meteoroid stream produced by the decay of a parent comet with a perihelion distance of 0.975 AU [see Fig. 4.10(a)] it was found that all the resulting meteoroids had perihelia in the range 0.975 ± 0.1575 AU, i.e. $0.818 < q < 1.133$ AU, although significant numbers were only found in the more restricted range between 0.92 and 1.025 AU. Observed Perseid meteoroid orbits have perihelia between 0.895 and 0.976 AU (see Fig. 3.3). As the theoretical shape of the perihelion distribution curve seems to be independent of the parent comet's perihelion distance it seems reasonable to suggest that today's observed Perseids first started to be produced when the parent comet had a perihelion distance of around 1.13 AU, this being $0.976 + 0.1575$ AU. The inference from this is that today's observed Perseids started forming a *maximum* of 160,000 years ago, at which time the semi-major axis, the inclination, the argument of perihelion and the longitude of the ascending node of P/Swift-Tuttle were around 55 AU, 122°, 160° and 94° respectively. The full range of observed perihelia would have been produced gradually over the next 70,000 years as the comet's perihelion distance decreased from 1.13 AU to 1.05 AU and the semi-major axis from around 55 AU to around 40 AU.

The formation of the observed Perseids can be thought of as occurring in two time periods. The interval 160,000 to 90,000 years BP (before present) saw the gradual production of a few observable meteoroids with progressively lower perihelia. From 90,000 years BP to the present day saw the strong 'building-up' of today's stream and its observed perihelion distance distribution.

Some idea as to the 'true' perihelion distribution can be obtained by adding together the contributions to the stream from various periods over the past 160,000 years. In doing this it has been assumed that the cometary emission process has not changed over this period. Due to limits on available computing time the gradual change in the orbit of the parent comet, shown in Fig. 4.13, has been replaced by a sequence of specific orbits, the cometary orbital parameters staying constant for 5000 years and then changing abruptly. Over the last 160,000 years it has thus been assumed that P/Swift-Tuttle had 33 different orbits. These orbits are listed in Table 4.2.

The perihelion distribution of all the meteoroids produced by the decay of P/Swift-Tuttle over the last 160,000 years is shown in Fig. 4.14(a). This distribution has three peaks, these being at perihelion distances of 1.00, 1.05 and 1.12 AU respectively. These peaks correspond to three periods of relative stability in the orbit of the parent comet (see Fig. 4.13). Observers on Earth only sample a fraction of the Perseid meteoroid dust complex, this fraction having both perihelion distances less than 0.98 AU and orbital descending nodes that intersect the Earth's orbit.

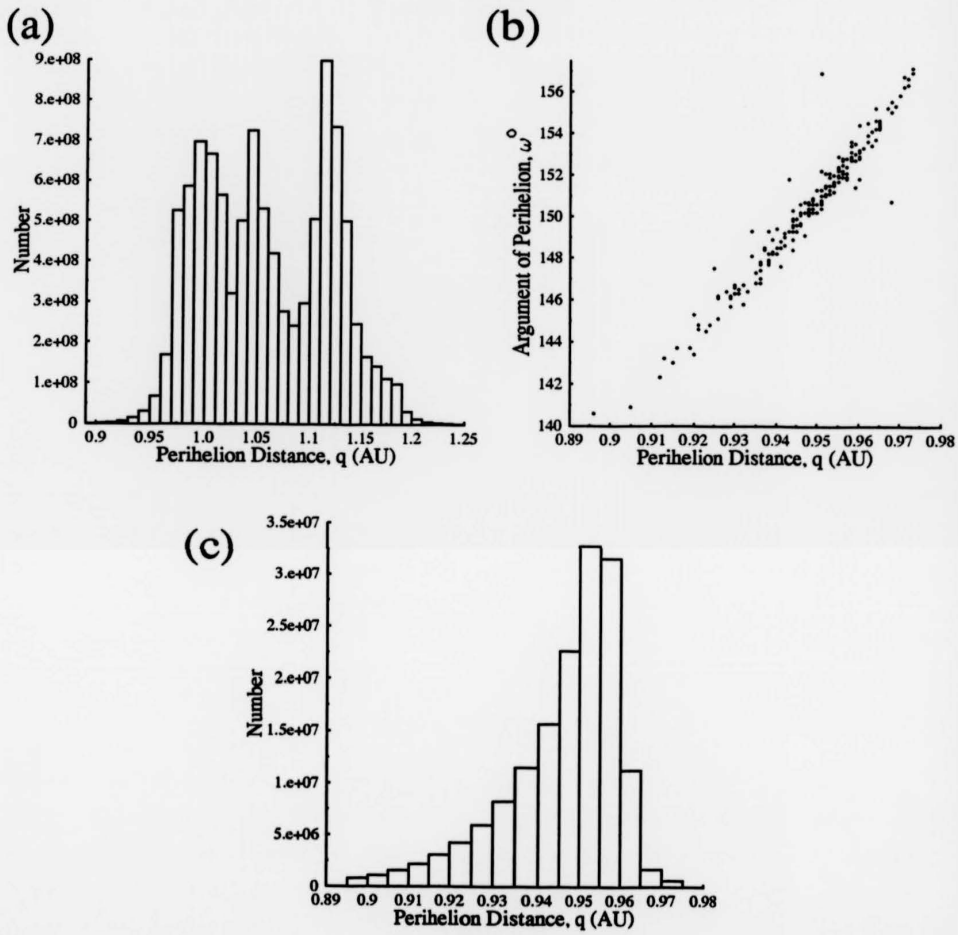

Figure 4.14: Histogram (a) shows the modelled perihelion distance distribution of the meteoroids produced by the decay of P/Swift-Tuttle over the last 160,000 years. The three peaks, at 1.00, 1.05 and 1.12 AU, correspond to three periods when the orbit of the parent comet was relatively stable. Plot (b) shows the relationship between the perihelion distance and the orbital argument of perihelion for the observed photographic meteors. For any specific meteoroid perihelion distance less than 1 AU there is only a narrow range of ω values that will result in an intersection with the Earth's orbit. Histogram (c) shows those meteoroids from histogram 4.14(a) that have descending nodes that intersect the Earth's orbit. This modelled distribution compares favourably with the observed distribution in Fig. 3.3.

Let us assume briefly that the Earth is on a circular orbit. To observe a Perseid meteoroid which had a perihelion distance of 1 AU would require that meteoroid to have a descending node at 1 AU and thus an argument of perihelion, ω, of 180°. The observed Perseids have an ω distribution with values in the range $139° < \omega < 158°$, so it is not possible to observe Perseids with perihelia of 1 AU. When $q < 1$ AU the descending node doesn't have to be at perihelion to intersect the Earth's orbit. For any specific q value less than 1 AU there is only one possible value of ω that will result in an intersection with the Earth's orbit. The relationship between these q and ω values is shown in Fig. 4.14(b). This, however, is not the theoretical relationship but actual data from the file of observed Perseid orbits. The reason that meteoroids with $0.98 < q < 1.0$ AU are not observed is simply because they have $\omega > 158°$, this being outside the observable argument of perihelion range. The decrease in the numbers of observed meteoroids with $q > 0.96$ AU is due to the fact that the numbers of meteoroids with $\omega > 153°$ steadily declines. Fig. 4.14(c) shows those meteoroids from the modelled distribution given in Fig. 4.14(a) that actually have descending nodes that intersect the Earth's orbit. Notice the similarity between this histogram and the observed Perseid perihelion distance distribution shown in Fig. 3.3.

Fig. 4.14(a) represents the meteoroid complex that has been produced over the last 160,000 years. If the orbital integration had been continued further backwards in time then the third peak (the one maximising at 1.125 AU) would steadily broaden, as the comet's perihelion distance increased, until the dust complex overlapped the orbit of Mars and beyond.

4.5.1 The modelled P/Swift-Tuttle dust complex

Figs. 4.15 and 4.16 show the ecliptic footprints of the descending node distribution of the modelled P/Swift-Tuttle meteoroids, along with the corresponding 3-D plots.

Fig. 4.15 consists of a series of 33 descending nodal concentrations, these corresponding to the 33 orbits of the evolving comet mentioned earlier. With a considerable increase in computing time and power we could increase the numbers of comet evolutionary steps drastically so that the peaks might be seen to merge into one another. An alternative method is to smooth the existing descending node data. This has been done in Fig. 4.16 using a 5×5 running mean method. The result is an unbroken 'ribbon' of material intersecting the ecliptic plane. The relative concentration of this ribbon is graphically shown in the accompanying 3-D plot. The ribbon itself displays areas of increased meteoroid activity, these being the peaks indicated by the contour marked 6. The bottom left-hand corner of the footprint contains those meteoroids that were produced around 160,000 years ago. As we move diagonally upwards along the footprint we encounter meteoroids that were produced during more recent eras. The top right-hand side of the footprint corresponds to those meteoroids produced over the last 5000 years. It is important to note that the gravitational perturbation suffered by the stream meteoroids has not been taken into account and that the model represents the

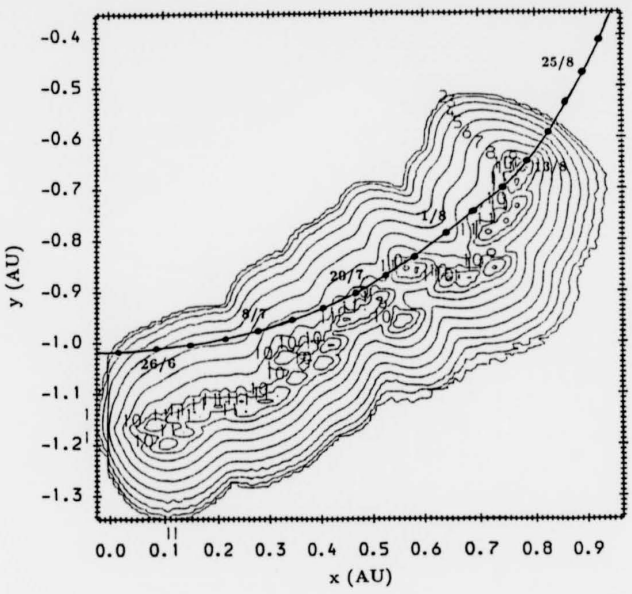

1.0	10.0
2.0	50.0
3.0	250.0
4.0	1250.0
5.0	6250.0
6.0	31250.0
7.0	156250.0
8.0	781250.0
9.0	3906250.0
10.0	19531250.0
11.0	97656250.0

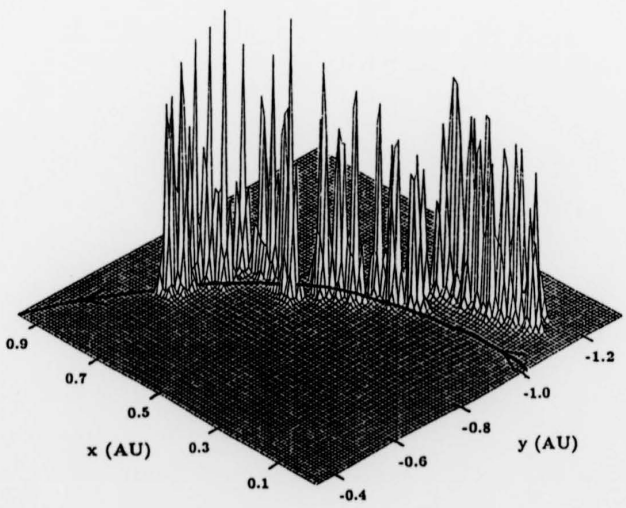

Figure 4.15: This ecliptic contour plot shows the relative concentrations of the descending nodes of the model meteoroids. The series of 33 descending nodal concentrations (also shown in the accompanying 3-D plot) correspond to the 33 orbits of the evolving comet as mentioned in section 3.3.6.

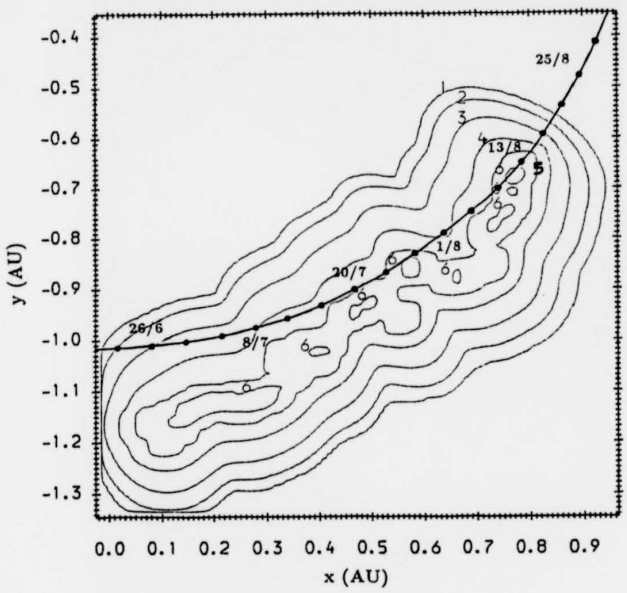

1.0	10.0
2.0	250.0
3.0	6250.0
4.0	156250.0
5.0	3906250.0
6.0	27343750.0

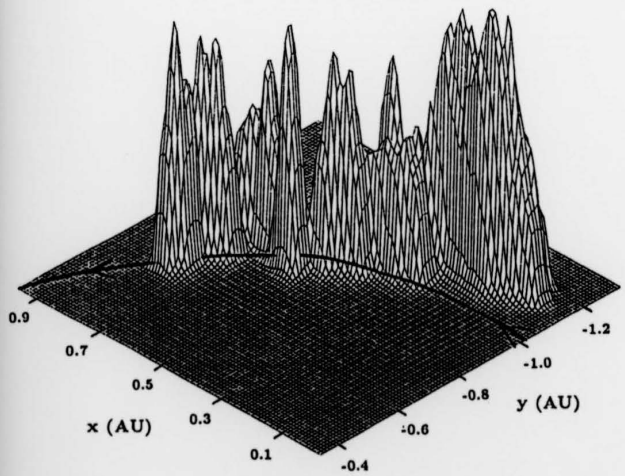

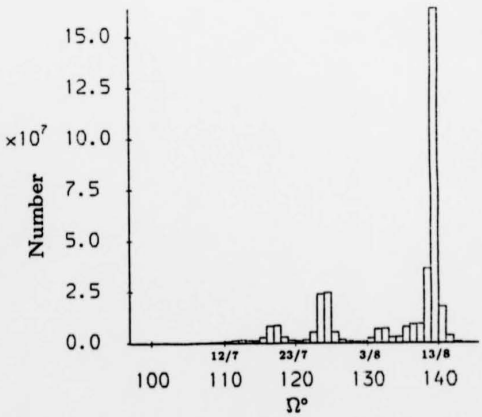

Figure 4.16: The data that produced Fig. 4.15 has been smoothed using a 5×5 running mean method. The concentrations of descending nodes have now 'merged' into one another to produce an unbroken 'ribbon' of material intersecting the ecliptic plane. The accompanying histogram shows the relative numbers of modelled meteoroids that the Earth (bold line) encounters as a function of the solar longitude of the Earth and the date in the year.

'core' meteoroids (see section 3.2), i.e. those with $D' < 0.07$ when compared to the orbital parameters of the parent comet at that specific era. Those meteoroids that suffer dispersion due to perturbations are not considered. Short term orbital perturbation might be negligible but it can be seen from the way in which the comet's orbit evolves that portions of the stream itself will 'move in' and as time progresses, the perihelion distances will decrease so that meteoroids that had nodes beyond the Earth's orbit will be perturbed so that they cross the orbit and thus become potentially detectable as meteors. The footprints shown in Figs. 4.15 and 4.16 will thus slowly pivot about the present x,y position of maximum activity. More and more meteoroids will intersect the Earth's orbit before maximum and these early-August, late-July meteoroids will be the oldest i.e. the early-August Perseids will generally have left the comet much longer ago than the mid-August ones.

The bold lines on Figs. 4.15 and 4.16 represent the Earth's orbit as it passes through the dust complex. The histogram in Fig. 4.16 shows the relative numbers of modelled meteoroids encountered by Earth as a function of the solar longitude of Earth and the date in the year. Significant numbers of meteoroids are not encountered until around July 8. The model then predicts a gradual, but fluctuating rise to maximum meteoroid flux, this occurring when the Earth intersects the 'central' meteoroid concentration around August 11/12. There is then a much steeper, smoother decline in meteor activity until the count drops to negligible numbers by August 18.

4.5.2 Perseid radiants

The Perseids have their radiant in the constellation of Perseus, this being the point on the celestial sphere from which the meteors seem to radiate (see section 2.3.1). As the orbital parameters are known for each modelled meteoroid that intersects the Earth's orbit during July and August, the corrected radiants can be calculated by following the method described by Porter (1952). (The corrected radiant is obtained from the observed radiant by removing the effects of the Earth's gravitational field and spin). The results are shown in Fig. 4.17(b) in the form of a contour plot.

The abscissa and ordinate correspond to right ascension, α, and declination, δ, respectively (in degrees). Fig. 4.17(a) shows a plot of the corrected radiants of the observed core photographic Perseids for comparison. The bold cross indicates the *observed* mean corrected radiant at $(\alpha, \delta) = (46.4°, +57.8°)$. The accompanying 3-D modelled radiant plot indicates the extent of the central radiant concentration around the mean. It is clear that significant numbers of photographic meteors are not detected outside the contour marked 2. The model predicts that there is an extension to the excepted radiant field, projecting towards the bottom right of the diagram. The concentrations of meteors in this part of the sky is, however, some 50 times less than around the mean corrected radiant, so it is not surprising that Perseid meteors have not been detected in any great numbers radiating from this part of the sky.

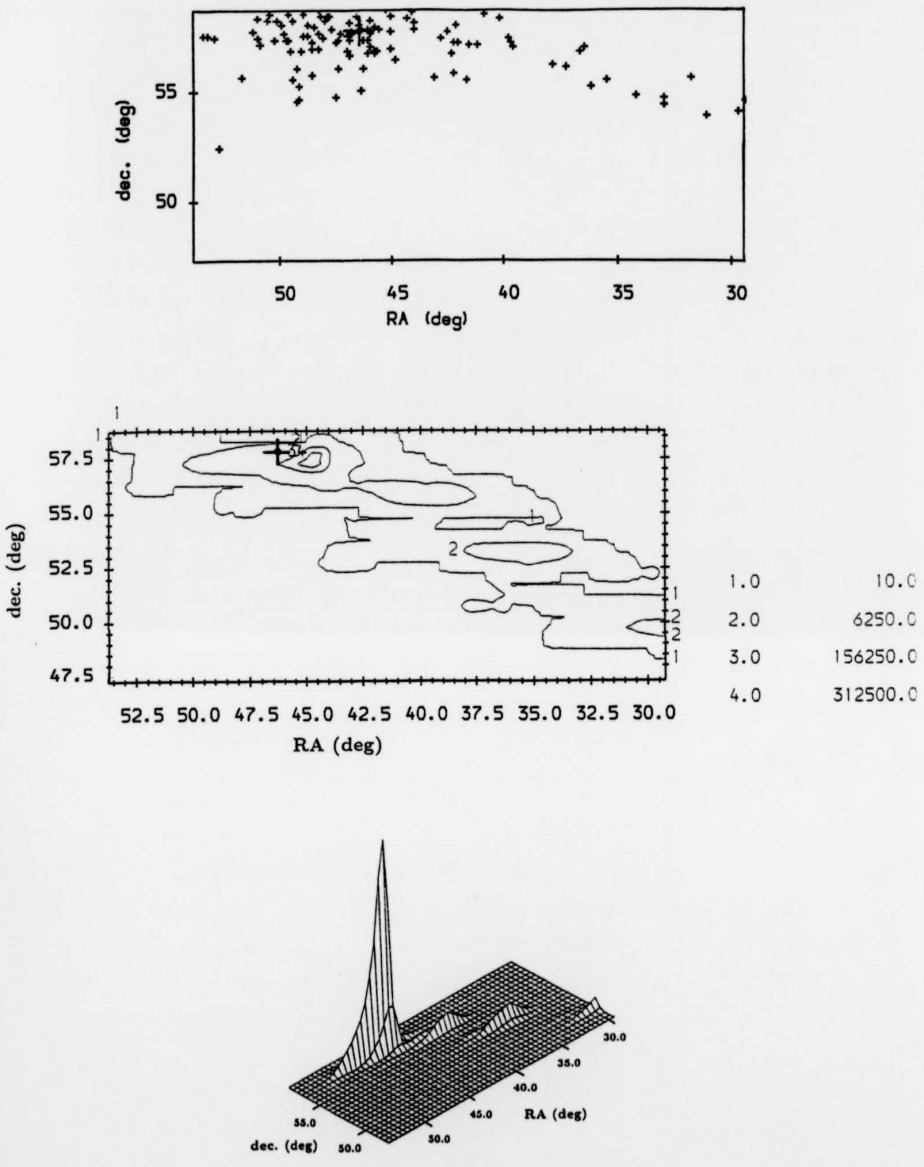

Figure 4.17: The top plot shows the distribution of the corrected radiants of the observed core photographic Perseids. The bold cross indicates the observed mean corrected radiant. The contour plot shows the modelled distribution of Perseid corrected radiants. The numbers listed on the right of the contour plot indicate the relative height of each numbered contour. The accompanying 3-D modelled radiant plot indicates the magnitude of the central radiant concentration.

Detection of these predicted meteors during late July/early August would have the effect of shifting the observed mean corrected radiant so that it coincides with the central contour in Fig. 4.17(b).

4.6 Conclusions

The Perseids are one of the most active of the meteor showers that can be seen from Earth at the present time. It is clear, however, that the Earth observer only samples a small percentage of the Perseid stream. The majority of the meteoroids in this stream have orbits that intersect the ecliptic plane outside the Earth's orbit. The distribution of meteoroid perihelion distances indicates that the Perseid meteoroids that are seen at the present time could not have left the parent comet more than about 160,000 years ago. *All* the meteoroids emitted before that time had orbits that did not intersect the Earth's orbit.

An integration of the orbit of P/Swift-Tuttle back in time for 270,000 years (Yau, private communication) has shown that there have been no sudden variations in any of the cometary orbital parameters during this time interval. This can be taken to indicate that this comet has been an intermediate-period comet for at least this time interval and that it was captured into the inner solar system from the Oort cloud some time before 270,000 BP.

Hughes and McBride (1989) estimated that the 'observed' Perseid stream had a total mass of around 3×10^{17} g. This is now seen to be very much a lower limit. In Fig. 4.15 it can be seen that Earth passes through only two of the 33 peaks of nodal distribution that were produced over the last 160,000 years. Many more Perseids could have been produced at even earlier times.

The mass loss from P/Swift-Tuttle at its 1992 perihelion passage is estimated to be of the same order of magnitude as that from P/Halley (see Hughes, 1985), this being around 3×10^{14} g. If the comet lost about the same amount of mass at each of its previous perihelion passages, and if (as is to be expected) about 30 % of this mass was in the form of meteoroid dust, it would be concluded that it has taken at least 3000 orbits of P/Swift-Tuttle to form the Perseids that are observed today. This is not possible as it is only over the last 1200 orbits (i.e. 160,000 years) that P/Swift-Tuttle has been producing observable meteoroids. It is thus clear that at some time during that interval the comet must have lost considerably more mass per perihelion passage than it has during the last 20 or so apparitions (see Yau et al., 1994). Hughes (1990) intimated that the cometary mass loss per perihelion passage is proportional to (among other things) $q^{-0.5}$, so the fact that the perihelion distance of P/Swift-Tuttle has been generally decreasing over the last 270,000 years does not help the situation.

The orbital evolution of the Perseid meteoroids that is caused by the gravitational influence of the major planets has been ignored in this thesis. Wu and Williams (1993) indicated that the general effect of this gravitational perturbation was to increase the scatter of the nodal distribution in the ecliptic plane and thus lead to a decrease in the number of

descending nodes per unit area as a function of time. This would not affect the conclusions that have been drawn in this chapter. Core Perseids are only seen for a few days in mid-August. The fact that Perseids are not seen throughout late July and early August in any great numbers indicates that the gravitational perturbations of meteoroids that were produced by the decay of the comet in the distant past do not produce concentrations of meteors that can be seen today.

Date BP($\times 10^3$ y)	q(AU)	a(AU)	i(deg)	ω(deg)	Ω(deg)
160	1.14	55.0	122.0	160.5	94.0
155	1.18	54.0	122.5	160.75	95.0
150	1.13	50.0	121.5	160.5	96.0
145	1.16	49.0	123.0	161.0	96.5
140	1.12	48.0	121.0	160.5	97.5
135	1.13	41.5	123.0	160.0	98.0
130	1.11	45.0	121.0	160.3	99.0
125	1.115	41.0	121.0	159.5	100.0
120	1.11	45.0	121.0	158.5	101.0
115	1.11	43.0	120.0	158.0	102.5
110	1.13	43.0	121.0	157.5	102.5
105	1.12	39.0	120.5	158.0	104.0
100	1.12	36.0	122.0	157.5	105.0
95	1.115	39.5	121.0	158.0	106.0
90	1.05	42.0	120.0	157.5	107.5
85	1.09	37.0	121.0	156.5	108.0
80	1.04	35.0	120.0	155.5	110.0
75	1.07	32.0	121.0	154.0	111.0
70	1.04	34.0	119.0	153.0	112.5
65	1.0	32.5	120.0	151.0	115.0
60	1.0	30.0	120.0	150.5	117.0
55	0.995	28.5	119.75	151.5	119.0
50	1.05	28.0	120.0	151.0	120.0
45	0.98	29.0	118.0	153.0	123.0
40	0.99	29.0	119.0	152.0	124.0
35	1.04	26.0	119.5	153.0	126.0
30	1.05	26.0	119.0	151.0	127.5
25	1.065	24.0	119.0	152.0	130.0
20	1.01	25.0	117.0	152.0	132.0
15	1.0175	25.0	116.5	153.0	134.0
10	1.01	26.0	114.5	152.5	136.0
5	0.98	26.0	115.0	152.5	137.5
0	0.975	25.658	113.8	152.7	139.3

Table 4.2: The 33 assumed orbits of comet P/Swift-Tuttle over the past 160,000 years of orbital evolution. The final orbit (0 BP) corresponds to the mean orbit of the 20 apparitions of the comet prior to 1862 (i.e. 703 B.C. to 1737 A.D.).

Chapter 5

The Physical and Orbital Distribution of Main Belt Asteroids

5.1 Introduction

The previous chapters have considered the physical and orbital characteristics and dynamics of cometary meteoroids in the mass range $10^{-3} \leq m \leq 30$ g. The following analysis covers an entirely different group of solar system minor bodies in the mass range $10^{5.5} \leq m \leq 10^{24}$ g.

Most asteroids are found in a torus of space between the orbits of Mars and Jupiter known as the Main Belt ($2.2 \leq a_{ast} \leq 3.3$ AU, see Fig. 5.1). The 'centre' of the asteroid belt is at a heliocentric distance of approximately 2.8 AU. The semi-major axis distribution of asteroids within the main belt is uneven. Fig. 5.2(a) shows that regions of depopulation exist where the orbital period of Jupiter has a small integer ratio with asteroidal orbital periods. These 'resonant' regions are known as the *Kirkwood gaps* and the most prominent gaps appear at Jupiter:asteroid orbital period ratios of 1:3, 2:5, 3:7 and 1:2. These should not be thought of as heliocentric regions of the solar system where asteroids do not exist as the mean asteroidal eccentricity of 0.14 ensures that these regions are well populated. The gaps appear in 'semi-major axis space' and not in 'actual space'. There are also regions of resonant orbital concentrations such as the Hilda group of asteroids at the 2:3 resonance and the Trojans at the 1:1 resonance with Jupiter. The Trojans oscillate around the Lagrangian points of gravitational stability that lie 60° behind and ahead of Jupiter.

Fig. 5.2(b) shows the longitude of perihelion (Π) distribution for 4976 Main Belt asteroids (orbital data taken from 'Dance of the Planets', ARC Inc., Science Simulation Software, 1991). The longitudes of perihelion for Jupiter and Mars are indicated at $\sim 15°$ and $\sim 336°$ respectively. It is evident that the majority of asteroids have been gravitationally 'herded' into a quasi-Gaussian distribution of Π around that of Jupiter. It is generally accepted that

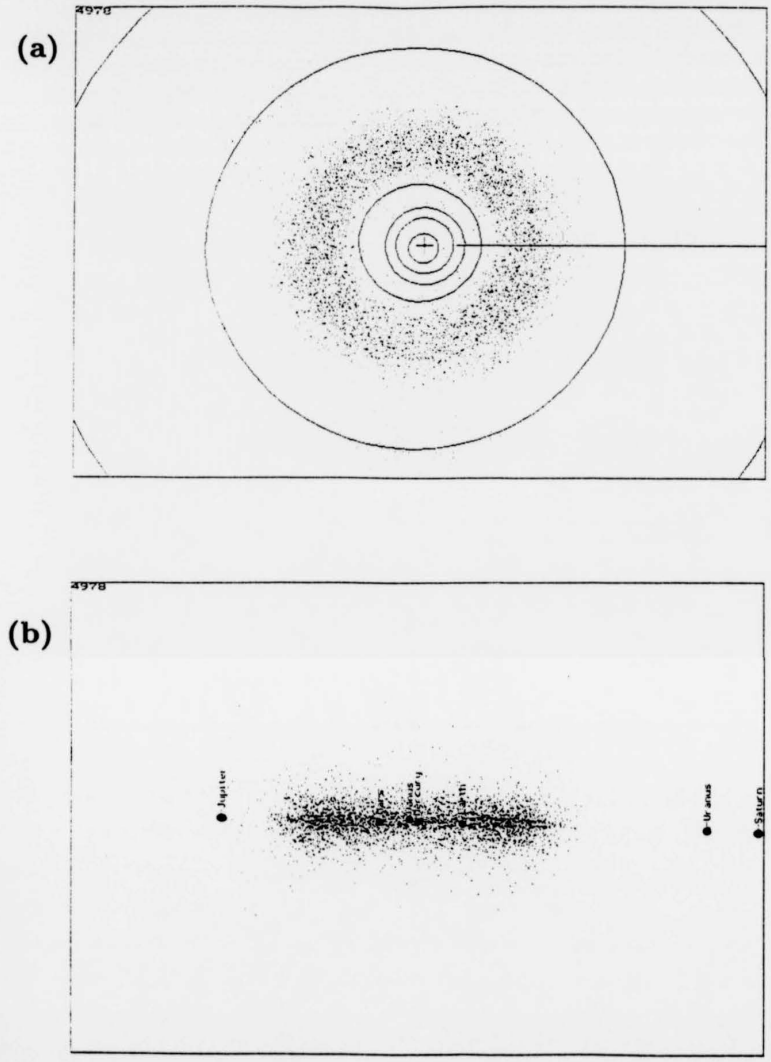

Figure 5.1: Plot (a) shows an overhead view of the main asteroid belt. Each of the 4978 dots represents the position of an individual asteroid at a specific time on its orbit. The Sun is at the centre (intersected by the cross) and the elliptical orbits radiating outwards represent the orbits of the planets Mercury, Venus, Earth, Mars, Jupiter and Saturn respectively. The horizontal line to the right of the diagram indicates the direction to the first point of Aries. Plot (b) shows the same set of asteroids viewed directly along the ecliptic plane. This viewing angle displays the varying degree of inclination of main belt asteroidal orbits.

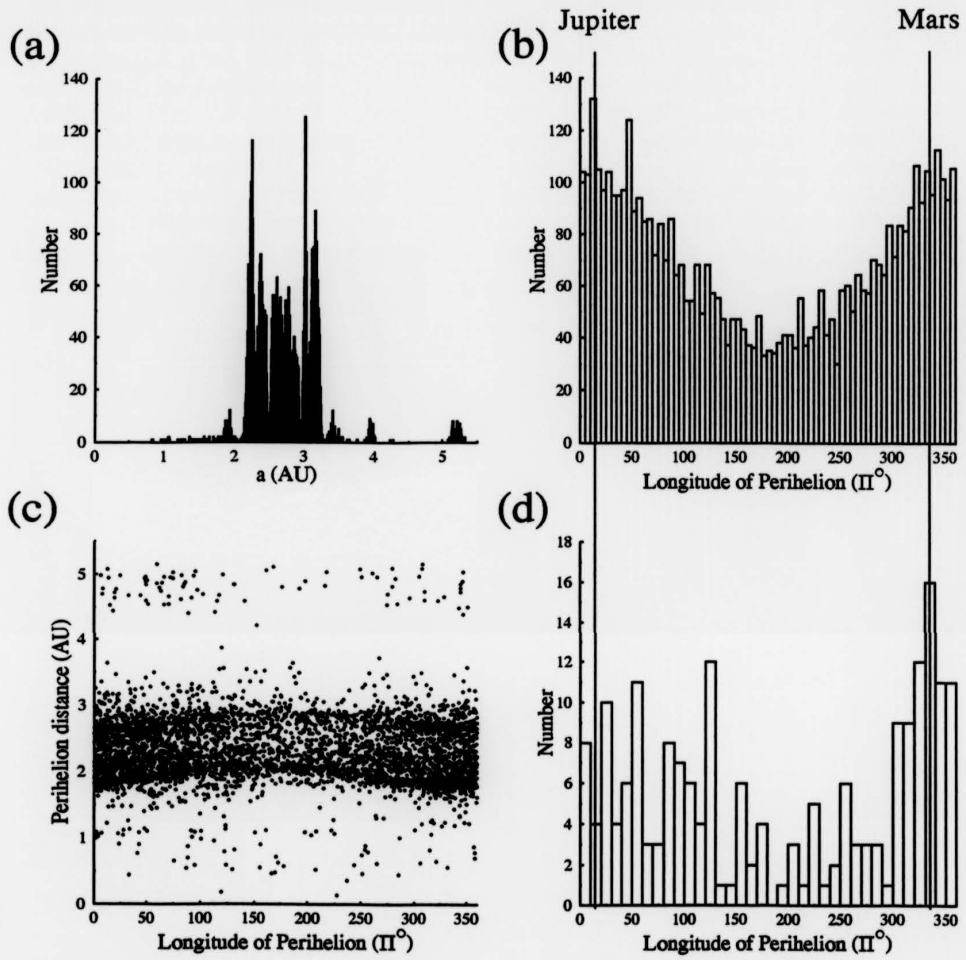

Figure 5.2: Histogram (a) shows the semi-major axis distribution for 4978 main belt asteroids. The 'Kirkwood gaps', created by resonant perturbations with Jupiter, show up clearly as regions of asteroid depopulation. Histogram (b) shows the longitude of perihelion (Π) distribution for these asteroids. The vertical lines at $\Pi \simeq 15°$ and $\Pi \simeq 336°$ indicate the longitudes of perihelion for Jupiter and Mars respectively. The majority of asteroids have been gravitationally 'herded' into a quasi-Gaussian distribution of Π around that of Jupiter. Mars itself has also probably suffered perturbations resulting in the re-orientation of its original longitude of perihelion into one similar to that of Jupiter's. Plot (c) shows the effect of long-term Jovian perturbations on the perihelia of Main Belt asteroids. The general effect of these perturbations, apart from the longitude of perihelion herding, is to decrease the asteroidal perihelia and increase the aphelia i.e. increase the orbital eccentricity. Histogram (d) shows the Π distribution for those asteroids with perihelia, q, less than 1.7 AU. The herding effect of Jupiter seems to be fairly limited in this region of the solar system and the majority of orbital perturbation is of Martian origin.

most Main Belt asteroids are fragments from the break-up of much larger bodies. During a collisional fragmentation event, the asteroidal fragments' longitudes of perihelion tend to become randomised (the extent of this randomisation depends on the energy of the collision and the resulting fragment ejection velocity). This would have the effect of broadening the distribution of $\Pi_{asteroid}$ around $\Pi_{Jupiter}$. The distribution in Fig. 5.2(b) is thus an indication of orbital age. During the early days of the solar system the distribution would presumably have been relatively flat. Those asteroids whose orbits have become aligned with that of Jupiter have survived long periods of time (> 10 My) since their last collisional fragmentation event. Fig. 5.2(c) shows this in more graphic form. Notice how the Main Belt of asteroids has been 'warped' by the gravitational influence of Jupiter towards lower perihelion distances. The reverse effect is seen for asteroidal aphelia, so the overall effect is the production of greater orbital eccentricities. Mars has exerted its own influence on the inner-belt asteroids. Fig. 5.2(d) shows the Π distribution for those Main Belt asteroids with $q < 1.7$ AU. It is clear that the influence of Jupiter is somewhat limited in this region and it is Mars that is performing the majority of the 'herding'.

5.2 The distribution of asteroid sizes and its significance

In the past the size distribution of Main Belt asteroids has been investigated by, among others, Hughes (1982) and Donnison & Sugden (1984). Hughes used the diameters of 740 asteroids given in the TRIAD file listed by Bowell, Gehrels and Zellner (1979) as his basic data. 740 represented just over 30% of the asteroids known at that time.

The following analysis uses the 1788 asteroidal diameters given by Tedesco (1989). This data set is also incomplete, the number 1788 again representing just over 30% of the 6000 or so asteroids that have numbers and thus well-known orbits. Even this latter number pales into insignificance in comparison to the total number of asteroids in the solar system.

The incompleteness of the data can be illustrated in two ways. Fig. 5.3 shows a plot of the diameter of an asteroid as a function of the perihelion distance of its orbit. The minimum size of an observable asteroid clearly increases as we move away from the Sun. This indicates that huge numbers of asteroids in the asteroid belt wait to be discovered.

Fig. 5.4 shows a logarithmic plot of the cumulative number of asteroids as a function of their diameters. As diameters decrease, this curve breaks away from linearity at about 130 km. The inference is that all asteroids larger than this size have been discovered in the $0 < q < 5.2$ AU range. Below this value there are many asteroids yet to be found. The break point (at 130 km) occurs at the same diameter as it did in the data used by Hughes (1982). The intervening twelve years have surprisingly made no difference to the completeness of the data at diameters less than 130 km.

Note that the curve in Fig. 5.4 can be thought of as being made up of subsidiary curves for asteroids of, say, small, medium and large perihelion distances. The 130 km break point

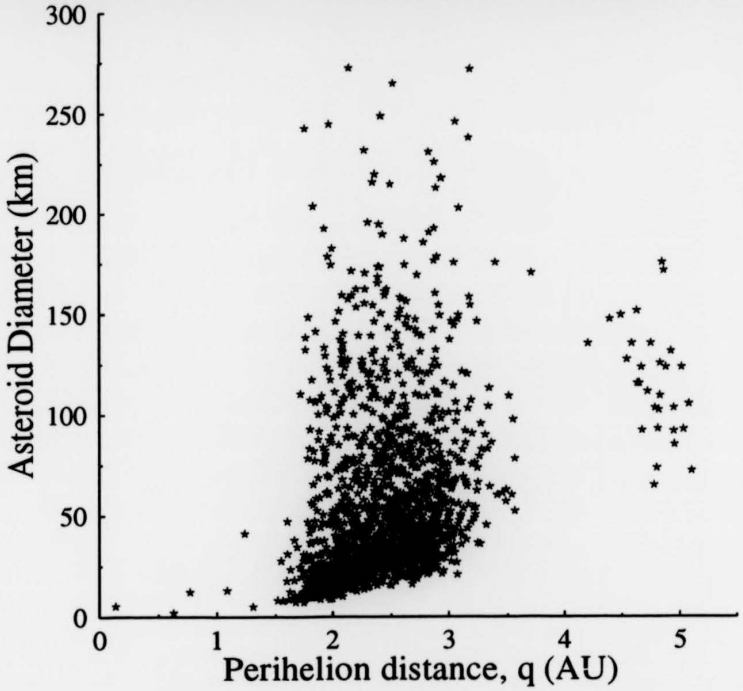

Figure 5.3: A plot of asteroid diameter as a function of perihelion distance. Note that the seven largest asteroids, 1 Ceres (diameter 913 km, perihelion distance = 2.554 AU), 2 Pallas (523 km, 2.120 AU), 4 Vesta (501 km, 2.147 AU), 10 Hygiea (429 km, 2.759 AU), 511 Davida (337 km, 2.607 AU), 704 Interamnia (333 km, 2.612 AU), and 52 Europa (312 km, 2.792 AU) have been omitted.

will apply to the large perihelion set. The medium and small set will have progressively lower break-point diameters. The break point is thought to be due entirely to a lack of completeness in the file of known asteroids. It occurs close to the $B(1,0)$ magnitude (Blue magnitude at 1 AU, zero phase angle) break in the estimated asteroid population function given by Shoemaker et al. (1989).

Let us return to the 1788 asteroids in Fig. 5.3. The minimum diameter, D_{min} km, of all the asteroids with perihelion distances, q, in the range $q - 0.05$ to $q + 0.05$ AU is noted. For the q range shown in Fig. 5.3 it was found that the relationship between D_{min} and q was approximately logarithmic. A least squares fit to the logarithmic data gave

$$\log D_{min} = (0.47 \pm 0.03) + (1.81 \pm 0.09) \log q \tag{5.1}$$

This contrasts with a similar analysis of the file of 740 asteroid diameters that was in existence twelve years before, which gave

$$\log D_{min} = (0.37 \pm 0.03) + (2.23 \pm 0.07) \log q. \tag{5.2}$$

In the asteroid region between perihelion distances of 1.3 and 5.0 AU it can be seen that the diameter of the smallest known asteroid has decreased considerably in the twelve year time period (1982-1994).

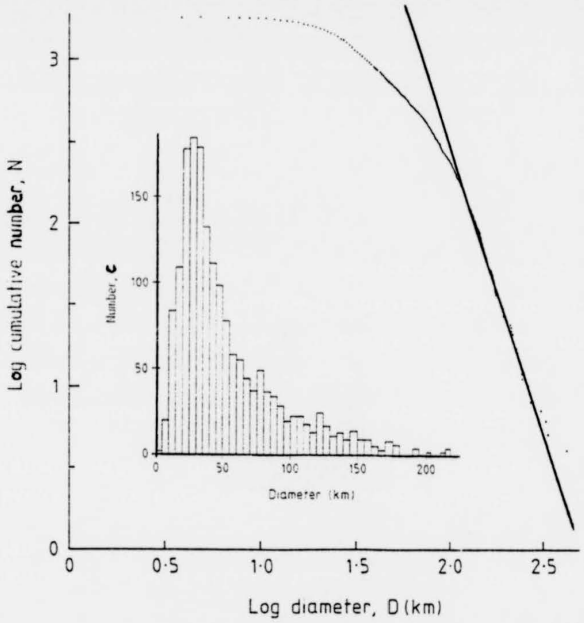

Figure 5.4: The logarithm of the cumulative number, N, of asteroids bigger than diameter D is plotted as a function of the logarithm of the diameter. The break from linearity occurs at about 130 km.
The inset histogram shows the 1788 asteroids with known diameters sorted into size bins. These bins are 5 km wide and C is the number of asteroids in each bin.

The relationships in equations 5.1 and 5.2 are not unexpected. For simplicity let us assume that (a) the brightness of an asteroid is not affected by its phase, that (b) all asteroids are spherical and that (c) all asteroids have the same albedo. The brightness of an asteroid will then be proportional to $D^2\Delta^{-2}r^{-2}$, where Δ and r are its distance from the Earth and the Sun respectively. The apparent magnitude, m, of the asteroid will be given by a formula of the type

$$m = K_1 + 5\log\Delta + 5\log r - 5\log D \quad , \tag{5.3}$$

where K_1 is a constant. There will be some limiting magnitude, m_1, such that asteroids that are brighter than this will be discovered and those that are not will not. This limiting magnitude will be approximately constant for any specific epoch. We can also assume that most of these small asteroids are discovered when they are both at opposition and at perihelion. Combining these circumstances converts equation 5.1 into

$$\log D_{min} = K_2 + \log(q-1) + \log q \quad , \tag{5.4}$$

where K_2 is another constant. The logarithmic relationship between the minimum asteroid diameter and the perihelion distance is clearly shown in equation 5.4.

The analysis of the data in Fig. 5.4 indicates that the linear portion of the cumulative relationship can be represented by

$$\log N = 8.93 - (3.27 \pm 0.30) \log D \qquad (D > 130 \text{ km}) \tag{5.5}$$

This is to be compared with the older equation

$$\log N = 8.574 - (3.057 \pm 0.42) \log D \qquad (248 > D > 130 \text{ km}) \tag{5.6}$$

which was given by Hughes (1982). In the intervening twelve years the total number of known asteroids has more than doubled and the number of asteroids with calculated *effective* diameters has increased by a factor of 2.4. Both these factors have had only a limited effect in the $D > 130$ km region. Here the increasing sophistication of infra-red observations has led to an improvement in the accuracy of the diameter measurements of individual asteroids, although the effective diameters are probably still only accurate to around 10% and are dependent on the thermal model used in the calculations (Lebofsky & Spencer, 1989). Some indication of how the effective diameters of the ten largest asteroids has changed as a function of time is shown in Table 5.1. The overall result of these changes is a *decrease* in accepted size and so the number of asteroids larger than say 130, 140, 150 km etc. is now thought to be *less* than it was eleven years ago (see Table 5.2).

Asteroid	Chambers (1889)	Barnard (1902)	Richter (1960)	Morrison (1977)	Bowell et al. (1979)	Tedesco (1989)
1 Ceres	315	780	768	1003	1025	913
2 Pallas	275	489	492	608	583	523
4 Vesta	344	391	392	538	555	501
10 Hygiea	166			450	443	429
31 Euphrosyne	74			370	270	248
704 Interamnia				350	338	333
511 Davida				323	335	337
65 Cybele	101			309	311	245
52 Europa	116			289	291	312
451 Patientia				276	281	230

Table 5.1: Recorded asteroid diameters (km) as a function of time.

Diameter (km)	130	140	150	160	170	180	190	200	220	250
Bowell et al. (1979)	124	99	84	67	54	47	42	34	24	14
Tedesco (1989)	121	95	73	56	47	35	30	26	18	10

Table 5.2: The numbers of asteroids larger than a specific diameter D (km).

Fig. 5.5 indicates how the size of the *largest* asteroids in each $q - 0.05$ to $q + 0.05$ AU range varies as a function of q. The upper abscissa indicates the apparent magnitude of an asteroid

of diameter 130 km, assuming that (i) it has an albedo of 0.22 and (ii) is seen when it is at perihelion and (iii) at opposition. As this apparent magnitude is less than 14 throughout the $q < 5.2$ AU range and D_{max} is above 130 km on the right hand side of Fig. 5.4 we can again conclude that the $D > 130$ km data is complete (as asteroids with magnitudes less than 14 are bright and 'unmissable').

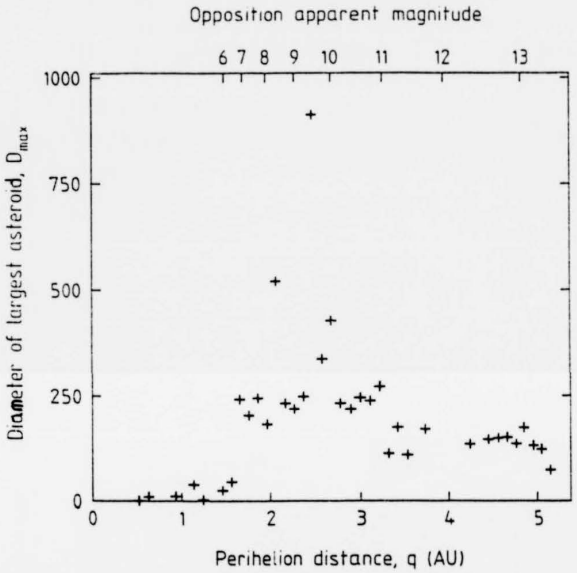

Figure 5.5: D_{max} is the diameter of the largest asteroid which has a perihelion distance in the range $q - 0.05$ to $q + 0.05$ AU. Remember that the knee of the curve in Fig. 5.4 occurred at $D = 130$ km. The upper abscissa shows the opposition perihelion apparent magnitude of $D = 130$ km asteroids.

One thing that has changed between equations 5.5 and 5.6 is the exponent of the power law. An astronomical collection of objects with differing sizes and masses is usually characterised by a mass distribution index, s. This index can be defined in a cumulative or noncumulative way (see Hughes 1972, 1982). If the number of objects with individual masses between m and $m + dm$ is taken to be proportional to m^{-s}, then the number of asteroids, $\zeta(D)$, with diameters between D and $D + dD$ and the number of asteroids, $\theta(D)$, with diameters greater than D are given by

$\zeta(D) = CD^{-(3s-2)}dD$ and $\theta(D) = ED^{-3(s-1)}$

where C and E are constants.

The $D > 130$ km data was analysed using the maximum likelihood method for various

ranges of asteroid semi-major axis. A least squares fit method obtains error values that are too small as the points in the empirical plot of $\theta(D)$ are not independent. The maximum likelihood method works with the raw data which do satisfy an independence condition (see Donnison & Sugden, 1984). The resulting mass distribution indices are shown in Table 5.3. As the mass distribution index for the $5.11 < a < 5.33$ AU asteroids is untypically large the best index for the large asteroid population has been taken as that given by the last line of Table 5.3. It is thus concluded that $s = 2.09 \pm 0.10$, a result that is to be compared to the $s = 2.02 \pm 0.14$ mass distribution index that was obtained previously for $248 > D > 130$ km (Hughes, 1972) and the $s = 2.02 \pm 0.09$ for $D > 130$ km (Donnison & Sugden, 1984). The *best estimate* of the value of s has increased from 2.02 to 2.09. Within the errors, however, it cannot be stated that this result is necessarily different from the previous results. Increasing the index above 2.0 means that the smaller asteroids provide a major contribution to the total mass of the asteroid belt and this larger index means that the asteroid belt is more massive than the 2.0×10^{25} g calculated by McBride & Hughes (1990).

semi-major axis (AU)	Number	Diameter (km)	Mass Index s
$2.20 < a < 2.71$	28	$131 < D < 501$	2.17 ± 0.22
$2.72 < a < 2.92$	28	$132 < D < 913$	2.05 ± 0.20
$2.93 < a < 3.14$	28	$131 < D < 429$	2.06 ± 0.20
$3.15 < a < 3.98$	28	$132 < D < 337$	2.01 ± 0.19
$5.11 < a < 5.33$	8	$131 < D < 175$	3.51 ± 0.89
$2.20 < a < 5.33$	121	$131 < D < 913$	2.14 ± 0.10
$2.20 < a < 3.98$	112	$131 < D < 913$	2.09 ± 0.10

Table 5.3: The mass distribution indices for various ranges of asteroid semi-major axis.

A logarithmic mass interval is defined as the interval between say 10^n and $10^{n+0.5}$ g. Let the total mass of all the asteroids with individual masses in that interval be ψ_n. This quantity is shown for the large asteroids in Fig. 5.6. It can be seen that the mass of *known* asteroids is concentrated in the $10^{20} < m < 10^{24.5}$ g region. For a collection of objects with a mass distribution index of 2.00, ψ_n is constant and is independent of n. For a distribution with $s = 2.09$, $\log \psi_n$ decreases by $(s - 2.0)$, i.e. 0.09 for every unit increase in n (see Hughes 1972). McBride & Hughes (1990) calculated the mass of the asteroid belt, M_A, by (i) estimating that Ceres has a mass of 2.0×10^{24} g, (ii) assuming that the mass distribution index was 2.0 in the $10^{21.5} < m < 10^{24}$ g mass range (iii) calculating that the average mass in the 0.5 log mass intervals in this $10^{21.5} - 10^{24}$ g mass range was 4.83×10^{23} g, (iv) assuming that hypervelocity collisional fragmentation was such that the mass distribution index retained the value of 2.0 over the *whole* mass range $10^{5.5}$ to 10^{24} g and that each interval in the $10^{5.5} - 10^{21.5}$ g mass range contained 4.83×10^{23} g and (v) assuming that there were no asteroids smaller than $10^{5.5}$ g. Thus

$$M_A = 2.0 \times 10^{24} + 2 \times 4.83 \times 10^{23}(24.0 - 5.5) \text{ g},$$

where $10^{5.5}$ g is the assumed mass of the smallest asteroid. So $M_A = 2.0 \times 10^{25}$ g.

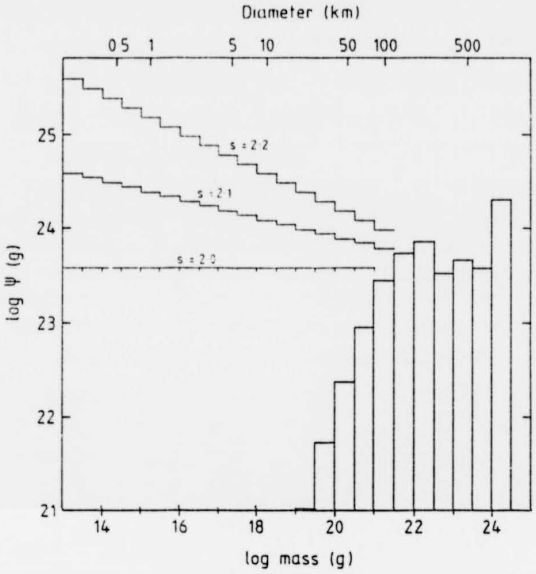

Figure 5.6: The histogram shows log ψ as a function of mass where ψ is the mass of those observed asteroids with individual masses in the range 10^n to $10^{n+0.5}$ g. If the mass distribution index, s, equals 2.0 then ψ does not vary with mass. If $s > 2.0$ it can be seen that the lower mass asteroids dominate the total mass. The upper abscissa gives the approximate asteroidal diameters. It can be seen that incompleteness sets in for $D < 130$ km.

It can be seen from Fig. 5.6 that mass distribution indices greater than 2.0 make the smaller sized asteroids dominate the total mass. If, for example, mass distribution indices of 2.05, 2.10, 2.15 and 2.20 apply to the $10^{24} > m > 10^{5.5}$ g mass range, the total mass of the belt would be 6.2×10^{25}, 2.1×10^{26}, 1.0×10^{27} and 5.4×10^{27} g respectively. With a mass distribution index of 2.09 ± 0.10 the mass of the belt is given by

$\log M_A(\mathrm{g}) = 26.21 \ \ (+1.4, \ -1.0)$.

One of the problems with the above calculation is the assumption that there are no asteroids with $m < 10^{5.5}$ g, an assumption that was justified in McBride & Hughes (1990). The justification was based on the fact that the Poynting-Robertson lifetime (the time taken for a body to spiral into the Sun under the influence of the Poynting-Robertson effect [see Chapter 2]) of asteroids with masses less than $10^{5.5}$ g is much shorter than the age of the solar system. This justification obviously does not account for the production of sub-$10^{5.5}$ g asteroids in more recent times due to collisional fragmentation. If this lower asteroidal mass

limit is changed to say 10^5, $10^{4.5}$, 10^4, $10^{3.5}$ and 10^3 g then the total mass of the belt, M_A, (assuming $s = 2.09$), is increased by 1.6×10^{25}, 3.7×10^{25}, 5.7×10^{25}, 1.1×10^{26} and 1.6×10^{26} g respectively.

The results from Fig. 5.3 and Fig. 5.4 can be combined in a rather interesting way. Fig. 5.7 shows the relative percentage of observed asteroids, n_{ob}, with perihelion distances in specific $q - 0.05$ to $q + 0.05$ AU bands. This curve suffers greatly from observational selection because the small asteroids are greatly under-represented, especially at larger perihelion distances. This effect can be corrected for in the following way. Assume that the incompleteness of the data in each perihelion region is quantified by the D_{min} value of each perihelion region, D_{min} being obtained from equation 5.1. Let us normalise everything to an asteroidal diameter of say 1 km and calculate $\frac{n_1}{n_{D_{min}}}$ for each perihelion region, where n_1 and $n_{D_{min}}$ are the numbers of asteroids larger than 1 km and D_{min} km respectively in that region. Assume that the size distribution index obtained from the linear region in Fig. 5.4, (i.e. the $D > 130$ km region), extends unaltered down to objects larger than 1 km. The multiple collisions that have taken place in the asteroidal regions make it likely that the size distribution index of asteroids does not vary from place to place. This is assumed to be true throughout the whole belt and throughout the Trojan regions.

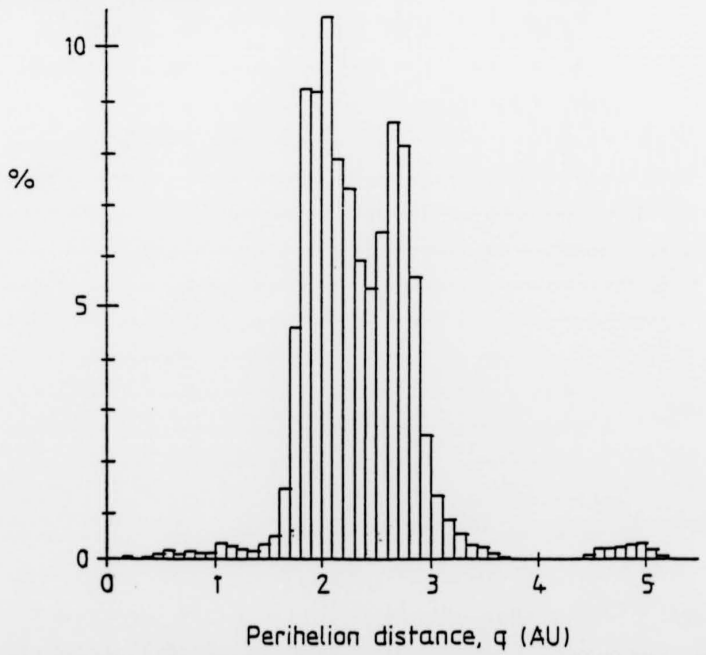

Figure 5.7: The orbits of 4976 asteroids have been used to plot the relative percentages of asteroids with perihelion distances in specific $q - 0.05$ to $q + 0.05$ AU bands.

Thus the ratio $\frac{n_1}{n_{D_{min}}}$ for a specific perihelion region is the same as the ratio $\frac{N_1}{N_{D_{min}}}$ for

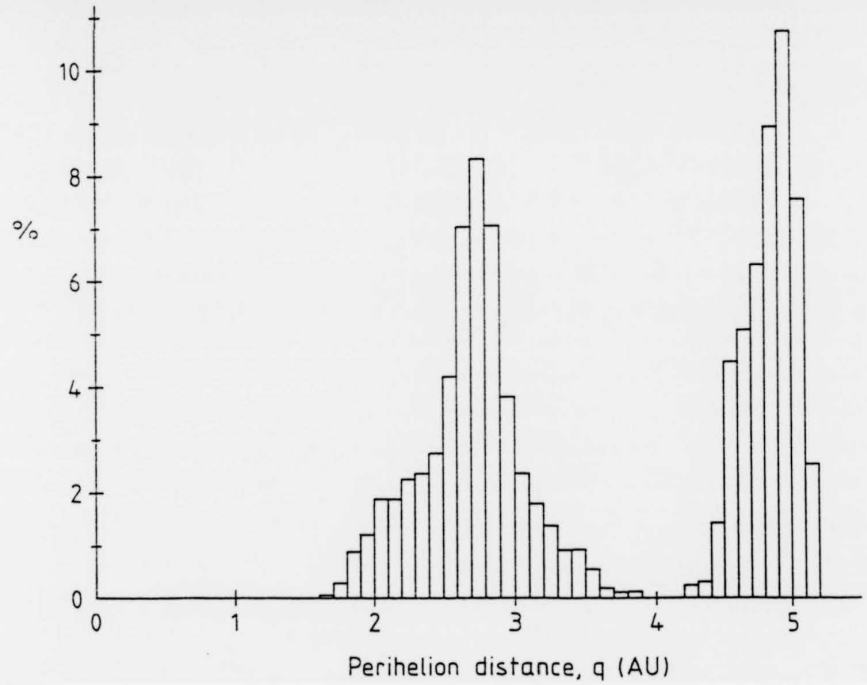

Figure 5.8: The histogram shows the *corrected* distribution of asteroidal perihelion distances.

the whole asteroid belt, where N_1 and $N_{D_{min}}$ are the total number of main belt asteroids larger than 1 km and the total number of main belt asteroids larger than a specific D_{min} respectively. This latter ratio can be obtained from equation 5.5. The number obtained by multiplying $\frac{n_1}{n_{D_{min}}}$ by n_{ob} (from Fig. 5.7) thus represents the true distribution of asteroids as a function of their perihelion distances and a normalised set of these numbers is shown in Fig. 5.8.

It can be seen that the *true* asteroidal perihelion distribution is much more concentrated than that of the observed belt and that the Trojan asteroids have a more dominant role. It can thus be concluded that the Trojan asteroid group is not a small feature of the solar system but contains a significantly large enough population to be considered an essential component.

The major problem with the above calculations is the assumption that s remains constant over such a large mass range. The validity of this assumption cannot be easily checked, the only help being the investigation of the distribution of crater diameters on satellite and planetary surfaces (see Chapter 6) and the estimation of the mass distribution of asteroid families and/or the parent bodies of meteorites.

5.3 Asteroid families : the Koronis family of asteroids

The Koronis family was one of the first three families of asteroids to be identified, along with the Themis and the Eos families (Hirayama, 1918). Hirayama identified these groups by looking for similarities in a, e and i. At present over 100 families are recognised and group associations are made by spectral characteristics as well as orbital similarities. The Koronis family has some 50 known members (the orbital parameters are listed in Appendix B) and the parent body is thought to have been an S-type asteroid of around 90 km in diameter. The family lies near the 5:2 Kirkwood gap and as a result it may be a source of some Earth-crossing fragments and meteorites. Binzel et al. (1989) found that the lightcurve amplitudes of the Koronis family were statistically higher than the amplitudes found for comparable field asteroids. The suspicion is that the Koronis family all have spin axes pointing in the same direction and this direction happens to be perpendicular to the mean orbital plane of the family. The orbital dispersion of the Koronis family is given by

$$a = 2.875 \pm 0.018;\ e = 0.049 \pm 0.006 \text{ and } i = 2.118 \pm 0.081.$$

The similarity of family orbital parameters is shown in Fig. 5.9. The plot has been drawn assuming that all 52 orbits have zero inclination. The two ellipses in the centre of the diagram represent the orbits of Earth and Mars respectively.

Figure 5.9: An orbital plot of 52 Koronis-family asteroids. The inner and outer bold ellipses represent the orbits of Earth and Mars respectively and the Sun is at the 'centre'. The vertical line at the top of the diagram points towards the First Point of Ares.

When a family is produced, by the fragmentation of the parent, many of the larger members of the family are thought to 'remember' the original spin of the precursor body due to their large moments of inertia (see Chapman et al., 1989). As time passes the collisional evolution of the family is thought to lead to the production of a distribution of both spin periods and spin axis orientation around the values of the original body. The idea behind this hypothesis is that non-random spin is indicative of youthfulness i.e. young families have non-random spin axis distributions and as time passes these distributions become more random. Paolicchi et al. (1989) state that different impact conditions can, however, lead to different spin and mass distributions.

Binzel et al. (1989) noted that the large members of the family have similar spin rates and that the dispersion increases with decreasing diameter. Sykes et al. (1989) noted that the Koronis family is associated with an IRAS dust torus. Again this has an 'age' connotation. Is the dust band produced when the family is produced or does it take a time to produce this dust? Also, when produced, how long does it take for a typical IRAS dust torus to dissipate? Typical dust torus particle diameters detected by IRAS are of the order of 10 μm (see Dermott et al., 1994). Assuming a dust particle density of 3.5 g cm^{-3}, this results in a PR lifetime of approximately 10^5 years. This lifetime will be lengthened by solar radiation pressure acting on the dust particles. The ratio, β (see Chapter 3), between the forces of solar radiation pressure and solar gravitational attraction is approximately 0.03 for the size of dust particles being considered. Sykes et al. quote the Koronis parent as having a minimum size of 90 km. He gives the Koronis family a minimum age of 1.3×10^8 years. In comparison the ages quoted for the Themis, Nysa and Eos families are 1.5×10^6, 1×10^9 and 5.8×10^8 years respectively.

The absolute brightness of an asteroid is proportional to the product of the albedo and the square of the diameter. Following Zellner and Bowell (1977) we have

$$\log D(\mathrm{km}) = 3.122 - 0.2V(1,0) - 0.5 \log p_V. \tag{5.7}$$

It is expected that all the asteroid fragments from the same family (and certainly from a family with a parent as small as 90 km) will have the same albedo. Take the albedo of all the Koronis family asteroids as being 0.21 (S-Type). Thus

$$\log D = 3.461 - 0.2V. \tag{5.8}$$

The estimated diameters listed in Appendix B have been calculated using this equation.

5.3.1 The mass distribution of the family and the mass of the parent body

Fig. 5.10 shows a plot of the size distribution of the Koronis family. Two things are obvious. (i) The larger fragments can be represented by a mass (size) distribution index of 2.0. (The curve deviates from linearity at $D < 30$ km because many of these smaller fragments have not been discovered yet.)

(ii) The largest fragment has a mass of around $10^{20.5}$ g. Let us refer to this largest mass as A.

This distribution is such that the number, N, of bodies with masses greater than m g is given by

$$\log N = \log A - \log m, \quad (s = 2.0) \tag{5.9}$$

and the amount of mass, U, made up of asteroids with individual masses in the logarithmic range 10^n to $10^{n+0.5}$ g is given by

$$U = A \log_e 10^{0.5}. \tag{5.10}$$

(see Hughes, 1972). Remember that a distribution with a mass distribution index of 2.0 is characterised by having the same amount of mass in each logarithmic mass interval (see section 5.2).

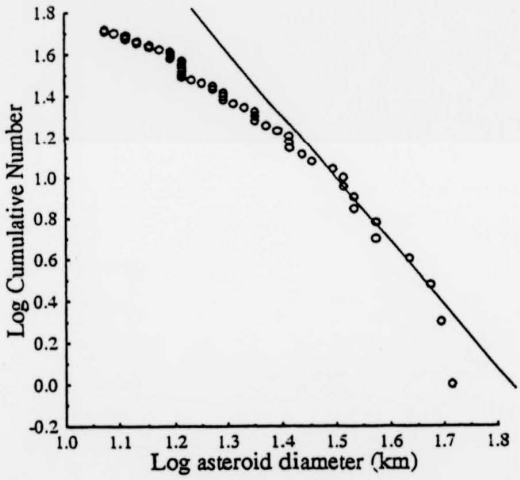

Figure 5.10: The cumulative number of koronis family asteroids with diameters greater than D km. The gradient of the straight line indicates a mass distribution index of 2.0.

To calculate the total mass of the Koronis family, a quantity that can be equated to the mass of the parent of that family (assuming no mass loss), one needs to know the least massive fragment produced by the collision. One also needs to assume that the mass distribution index of 2.0 applies to *all* the fragments. Let the least massive fragment have a mass of 10^a g. The total mass of the asteroid family, M_F, is then given by

$$M_F = 2A(\log A - a)\log_e(10^{0.5}). \tag{5.11}$$

Fig. 5.10 gives $A = 10^{20.5}$ g and the mass of the parent body obtained using equation 5.11 is given in Table 5.4 for various values of a. The diameter of the parent is obtained by assuming that it has a density of 3.5 g cm^{-3}.

Mass of smallest particle (g)	Diameter of smallest particle (cm)	Mass of Parent M_P (g)	Diameter of Parent (km)
10^{-9}	0.001	2.15×10^{22}	227
10^{-6}	0.01	1.93×10^{22}	219
10^{-3}	0.1	1.71×10^{22}	211
1	1	1.49×10^{22}	201
1000	10	1.27×10^{22}	191
10^{6}	100	1.06×10^{22}	179

Table 5.4: The size of the Koronis-family parent body for various smallest fragment masses.

The mass of the smallest particle produced by the fragmentation event is an unknown quantity. We could conceivably reduce this particle size down to sub-micron size or even down to molecular/atomic level if significant proportions of gas are produced during the catastrophic collision. The assumption that the mass distribution index after fragmentation is constant down to these particle sizes is, to say the least, highly unlikely. If the index rises above 2 as the particle size decreases then the majority of the mass of the parent body could be contained in the smaller end of the particle size spectrum. Conversely, if the index drops below 2 as the particle size decreases then the contribution, by mass, of the smaller particles could become insignificant when compared to the mass of the largest fragments. Experimental data on catastrophic disruption experiments (see Fujiwara et al., 1989) indicates that the fragment size distributions are usually divided up into two or three sections, with the size (mass) distribution index being generally higher for the larger fragments. If these results can be scaled up to asteroidal bodies then this would suggest that the parent body masses/diameters, given in Table 5.4 for specific lowest particle mass, are an upper limit. One thing that can be concluded from Table 5.4, which applies a mass distribution index of 2.0 down to particles of mass 10^{-9} g, is that on decreasing the mass of the smallest particle by a factor of 10^{15}, the mass of the parent body has increased by a factor of only around 2 and the diameter by around a quarter.

5.3.2 Collisional evolution of the asteroid belt

The present day asteroid belt has evolved through the process of collisional fragmentation. This is indicated by means of the mass distribution index, s. An index greater than 2 points towards evolution involving fragmentation whereas an index less than 2 indicates the process of accretion, as with the comet population (see Hughes, 1982). The asteroids that we observe today will be of two kinds:

(i) ejected fragments from craters on large parent asteroids, and

(ii) discrete fragments from the entire break-up of a parent asteroid due to a catastrophic collision.

Take the Koronis family member 243 Ida as an example. Ida is an S-class asteroid of stony-iron composition. It is irregular in shape and appears, from the Galileo images (see Fig. 5.11), to be about 52 km long. How can we tell in which category this asteroid lies? There is likely to be an upper limit to the size of crater ejecta. If we could determine the maximum size for crater ejecta then we could say that asteroids bigger than this size must be discrete fragments from a hypervelocity impact (which is what we would expect for a member of an asteroid family).

Consider a catastrophic collision between two bodies, one small asteroid, mass m, and one large asteroid, mass M. The energy gained by the target (the large asteroid) is $0.5mV^2M^{-1}$ per unit mass, where V is the encounter velocity. Typical asteroidal encounter velocities are of the order of 5 km s^{-1}. Following Farinella (1982), if this impact energy exceeds 10^5 J Kg^{-1} then both asteroids are catastrophically disrupted. So, for encounter velocities of 1, 3, 5 and 12 km s^{-1}, catastrophic disruption occurs if $\frac{m}{M} > 0.2$, 0.022, 0.008 and 0.0014 respectively.

The Galileo image of Ida (Fig. 5.11) shows that there is a very large crater (when compared to the asteroid size) at the top of the image. The estimated crater size is around 14 km which is approximately one third the mean diameter of Ida itself. The value of 3 for the ratio between the diameter of an asteroid and the diameter of the largest crater on its surface is displayed in other solar system bodies e.g. the Martian moon, Phobos (which has a mean diameter of around 23 km and its largest crater, Stickney, has a diameter of around 8 km) and the Saturnian moon, Mimas (which has a diameter of around 390 km and its largest crater, Herschel, is 130 km in diameter). This suggests that the ratio of 3 is probably the lowest value that is possible if a target body is to survive catastrophic disruption.

During the formation of Lunar impact craters, the larger ejecta are responsible for the formation of secondary impact craters. By analysing the sizes of these secondary craters it is evident that the largest fragment ejected from the primary crater has a diameter some 50 times smaller than the diameter of the primary crater. It can therefore be concluded that the largest crater fragment that can be produced by the collision of two asteroidal bodies is $\frac{1}{3} \times \frac{1}{50}$ times the diameter of the largest body. Therefore, if 243 Ida is a crater fragment then the parent body would have been around 6000 km in diameter. It is thus fairly likely that 243 Ida (and the other 51 known family members) is a fragment from a catastrophic collision event.

We can get some idea as to the largest crater ejecta in the solar system by assuming that Ceres (diameter 913 km) is typical of the largest asteroid that has ever been present in the asteroid belt. If this is so then only asteroids with diameters smaller than around 6 km can be crater ejecta. This means that practically all the asteroids shown in Fig. 5.4 are the result of catastrophic collisions. Hughes (1991), however, suggests that the largest asteroids that ever existed probably had diameters of around 8600 ± 800 km. This hypothesis indicates that asteroids with diameters smaller than around 60 km can be crater ejecta.

243 Ida is one of the most densely cratered objects that is observed in the solar system.

Figure 5.11: Galileo image of the Koronis family asteroid 243 Ida.

The size distribution of craters on planetary bodies can be represented by an equation of the form

$$\log N = b - 2.0 \log D \tag{5.12}$$

where N is the number of craters on the body that are larger than D km (see Chapter 6, section 6.2.2). If $N = 1$ for $D \geq 14$ km then $b = 2.29$. The inference from this is that the surface of Ida is scarred by around 200 impact craters with $D \geq 1$ km. It has been estimated that Ida's surface may date back 2×10^9 years (Chapman, 1994). The crater density is similar to that attained on surfaces that have been saturated by impacts and are in collisional equilibrium.

5.3.3 The collision velocity distribution of Koronis family asteroids and the probability of collision

The dominant process affecting asteroids during modern epochs has been their gradual grinding down due to collisions. These collisions may cause surface erosion as well as catastrophic fragmentation. The collisional evolution of individual family asteroids is affected by two distinct populations of asteroids: (a) collisions between a family asteroid and a Main Belt asteroid, and (b) collisions between two asteroids in the same family. Typical Main Belt asteroidal orbits are moderately eccentric ($\overline{e} \simeq 0.14$) and inclined ($\overline{i} \simeq 8.6°$), resulting in typical relative velocities between Main Belt asteroids of around 5 km s^{-1}. Relative

velocities between asteroids in the same family will be lower than this but the probability of inter-family collisions will be higher than for family-Main Belt collisions due to the increased family-asteroid spatial density (i.e. there are more asteroids per unit volume of space in a family than in the Main Belt as a whole).

The probability of collision between Ida and another orbiting body, per revolution of the body, is given by

$$P \propto \frac{U}{\sin i |U_x|} \tag{5.13}$$

where U is the relative velocity, i is the inclination of the orbits to one another and U_x is the radial component of the relative velocity at encounter (Öpik, 1951) (see Chapter 2, section 2.7.1).

The collision velocity distributions between Ida and another asteroidal body are shown in Fig. 5.12 for (a) Ida/Koronis family collisions and (b) Ida/Main Belt asteroid collisions. These velocity distributions have been calculated in the same way as for the meteoroid velocity distributions in Chapter 2, section 7, except that the gravitational acceleration of Ida has been ignored. The mean collision velocity for cases (a) and (b) is found to be (1.04 ± 0.64) km s^{-1} and (4.06 ± 1.56) km s^{-1} respectively. Case (a) involves 49 asteroidal collisions, whereas case (b) involves 2775 collisions. The corresponding collision probability distributions are shown in Fig. 5.12(c) and (d). The collision probabilities, P_{col}, are in arbitrary units. The median collision probabilities were found to be 15 for Ida/Koronis collisions and 3 for Ida/Main Belt collisions.

We can now get some idea as to the total probability of collision by multiplying each median probability by the number of colliding bodies in each of the two groups. It is assumed that the ratio of numbers of *observed* asteroids in each group is the same as the ratio of the *total* numbers of asteroids in each group. The inference from this is that Ida is around 11 times more likely to be hit by a Main Belt asteroid than an asteroid in its own family.

During Ida's collisional history, the largest body that it has encountered was that which formed the 14 km impact crater. This impacting body may have been a family member, in which case it collided with a velocity of around 1 km s^{-1}, or it may have been a main belt asteroid colliding with a velocity of around 4 km s^{-1} (around 11 times more likely). I mentioned earlier that the impact energy ($0.5mV^2M^{-1}$ per unit mass) must be less than 10^5 J kg^{-1} for the target body to survive intact. A rough estimate as to the mass of Ida (assuming a density of 3500 kg m^{-3}) gives $(1.4 \pm 0.5) \times 10^{17}$ kg. A simple calculation then leads to the conclusion that the largest body that Ida has encountered during its collisional history is a Koronis family asteroid of diameter (25 ± 3) km or a main belt asteroid of diameter (10 ± 1) km. It must be noted that the *mean* collision velocities have been used in these calculations. In reality a Koronis family asteroid may collide with a velocity anywhere between 0 and 2 km s^{-1} and a main belt asteroid between 0.2 and 17 km s^{-1} (although $1 \leq V \leq 6$ km s^{-1} is a more likely range of velocities for the latter case).

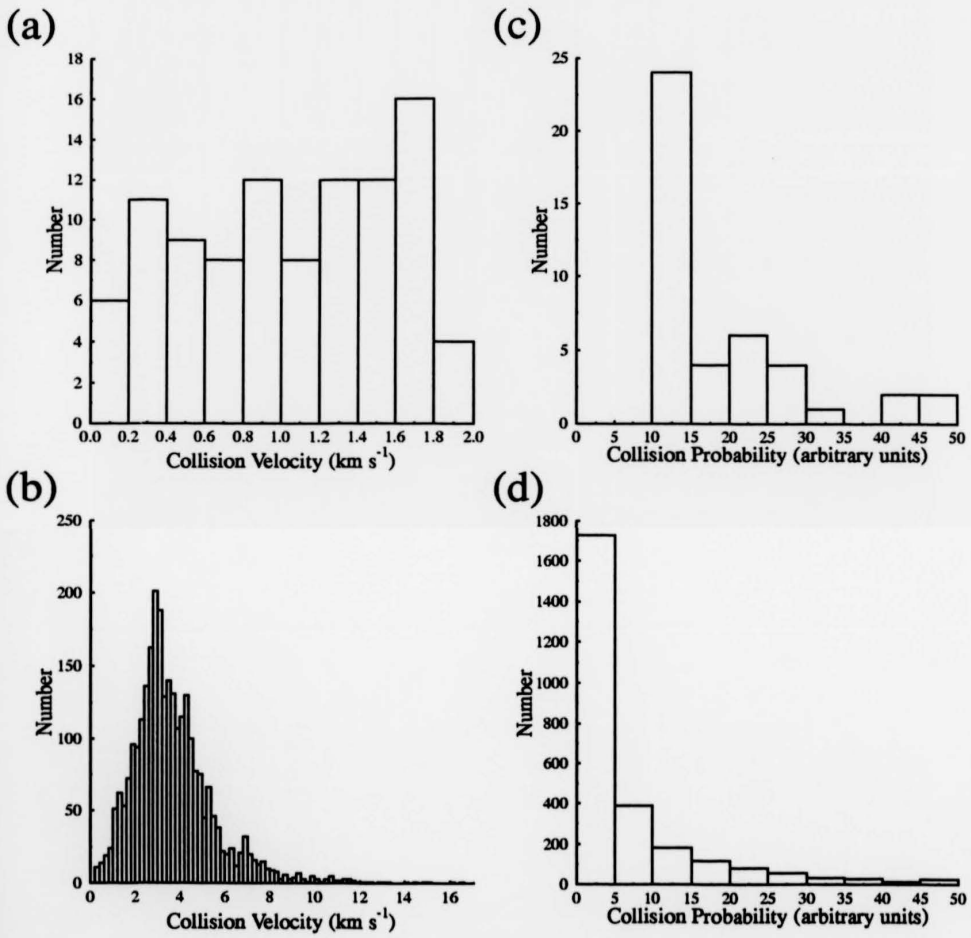

Figure 5.12: Histogram (a) shows the velocity distribution for collisions between 243 Ida and members of its own family. The mean collision velocity is 1.04 km s^{-1}. Histogram (b) shows the velocity distribution for collisions between 243 Ida and non-family main belt asteroids. The mean collision velocity is 4.06 km s^{-1}. The collision probability distributions are shown in histograms (c) and (d). The mean collision probability for Ida/Koronis collisions (c) is 15 (arbitrary units) and the corresponding value for Ida/Main belt collisions (d) is 3.

Chapter 6

Near-Earth Asteroids

6.1 Introduction

The Near-Earth Asteroids (NEAs) are a population of minor bodies whose orbits take them within the orbits of the inner planets ($q_{NEA} < 1.3$ AU). In 1898, 433 Eros was the first Earth-approacher to be discovered. In 1932, 1862 Apollo was found, the first Earth-orbit crosser. Since then many NEAs have been detected and they are classified into the following three groups (see Fig. 6.1):

(i) *Apollos* cross the Earth's orbit. An Apollo asteroid's perihelion distance must be within the Earth's aphelion (1.017 AU).

(ii) *Amors* have perihelia that lie in the range $1.017 < q \leq 1.3$ AU. i.e. their perihelia lie outside the Earth's orbit but inside the orbit of Mars.

(iii) *Atens* orbit entirely inside the Earth's orbit. i.e. they have $a < 1$ AU and their aphelion distances are less than the Earth's perihelion (0.983 AU).

Shoemaker et al. (1979) estimated that the population, to magnitude $V(1,0) = 18$, consists of approximately 100 Atens, 700±300 Apollos and 1000 to 2000 Amors, although the total number of known objects is currently in the hundreds.

These objects do not have long-term orbital stability. On a time scale of $\sim 10^4$ y the precession of their orbital arguments of perihelion and longitudes of their node and secular variations in their perihelia can convert the orbits of some Apollo objects into Amor objects and vice versa (Wetherill and Williams, 1968). These objects will then eventually either collide with one of the inner planets, or another asteroid, or be ejected from the inner solar system by a close-approach event (on a time scale of some 10-100 My.).

6.1.1 The source of NEAs

The short lifetime of these asteroids requires the existence of a constantly replenishing source. One probable source is the injection of asteroid fragments from the main belt. Until quite recently it was not fully understood just how these asteroidal fragments achieved such drastic

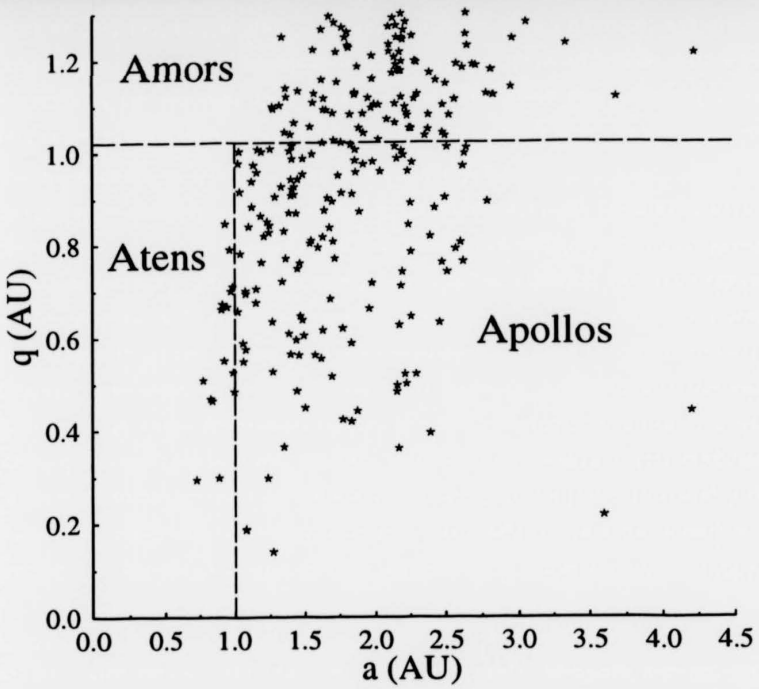

Figure 6.1: The orbital classification of 255 Near-Earth Asteroids. Near-Earth Asteroids (NEAs) are classified into three groups depending on their orbital characteristics. Amors have their perihelia between the orbits of Earth and Mars, Apollos cross the Earth's orbit and Atens orbit entirely inside the Earth's orbit.

orbit changes. The orbital velocities of main belt asteroids are of the order of 20 km s^{-1}. As a result, velocity increments of hundreds of m s^{-1} are required to achieve only a 1% change in their orbital parameters. As a consequence of interasteroidal impact events, fragments are usually ejected at velocities of a few 100 m s^{-1}. Ejection velocities of this magnitude are far too small to directly cause the drastic orbital changes required to achieve terrestrial planet-crossing orbits. The solution lies in the interplay between fragment ejection and resonant orbital perturbation. If the debris from a catastrophic collision in the main belt is ejected with the appropriate trajectory and velocity, fragments may stray into a resonance zone with Jupiter (or Saturn). Subsequent chaotic orbital perturbation can then transport these fragments into the terrestrial planet region (see Greenberg and Nolan, 1989). Wisdom (1983) indicated that an asteroidal fragment in the 3:1 commensurability resonance with Jupiter at 2.50 AU could become an Apollo object in around 1 My.

Extinct cometary nuclei in Earth-crossing orbits are also a possible source of some NEAs. The association of the asteroid 3200 Phaethon with the mean orbit of the Geminid meteor shower raises the question as to whether asteroids can have dust trails or whether 3200 Phaethon is an 'extinct' or 'dormant' cometary nucleus. Also a dust tail was discovered on a prediscovery image of asteroid 4015 1979 VA (Bowell 1992). The object now known as 4015 Wilson-Harrington is asteroidal in appearance. However, on prediscovery photographic plates

taken in 1949 the object had a fanned tail and was known as comet P/Wilson-Harrington 1949g=1949 III. This would suggest that 4015 Wilson-Harrington is also an inactive cometary nucleus. A third inactive comet candidate is asteroid 2060 Chiron. A faint coma has been observed around Chiron so it is therefore a comet (Meech & Belton, 1990). A CN emission band from Chiron was reported by Bus et al. (1991). In addition, the fact that comet P/Encke was not discovered until two centuries ago and comet P/Machholz not until 1986 suggests that these bodies are re-activated comets.

The surface of a cometary nucleus is likely to be an intimate mixture of snow and porous dusty and organic material. The continuous vaporisation of surface ice during successive cometary perihelion passages could eventually leave behind only dusty and organic surface materials, although ice would still be present within the porous structure under the insulating surface layer. The depletion of this 'surface ice' is a gradual process and it probably explains the tendency for shorter period comets being less active than longer period comets. The complete depletion of the surface ice could then result in the 'switching-off' of the cometary nucleus. To an observer the cometary nucleus might then be thought of as an asteroidal body. It is unlikely that the 'dormant' cometary nucleus would exist in this state for very long. The constant bombardment of the surface by meteoroids of varying sizes will cause fragments of the surface to break off the comet and may even cause a splitting of the nucleus if the impactor energy is high enough. In this scenario limited areas of the pristine, sub-surface cometary ices can be exposed to solar radiation and the result is the 'turning-on' of the cometary nucleus around specific 'active areas'. These freshly created active areas will themselves eventually either be switched off due to surface ice depletion, rendering the cometary nucleus inactive once again, or be replaced by new active areas created by further meteoroid bombardment.

The timescales for the evolution of short-period cometary bodies into asteroidal orbits is one to two orders of magnitude longer than the timescales of cometary volatile activity, so the existence of dormant or extinct comets is plausible.

Apollo objects are the parent bodies of the majority of Earth-impacting meteorites. Tons of interplanetary material fall into the Earth's atmosphere every day. Averaged over geological time, a total influx of around 1.7×10^8 kg/y hits the Earth over the mass range from 10^{-21} to 10^{15} kg (Ceplecha 1992). Every now and again, fragments heavier than a few kilograms partially survive their passage through the atmosphere to reach the Earth's surface as meteorites. Less frequently, the fall of larger bodies also occurs. The typical time interval between two Earth-impacts is a few centuries for 50 m sized bodies, causing an explosion equivalent to 10 Mtons of TNT (e.g. Tunguska, 1908); a few times 10^5 years for kilometre-sized objects and $\sim 10^8$ years for an asteroid or comet 10 km across (Farinella et al. 1994). A terrestrial impact with one of these larger Earth-crossing objects could conceivably produce disastrous effects on a global scale, such as that recorded at the K-T boundary.

6.2 Asteroid-Earth collision velocities

The diameter, D, of a crater on the Earth's surface can be related to the mass, m, and velocity, V, of the impacting body by an equation of the type

$$0.5mV^2 = 8.41 \times 10^{23} D^{3.57} \text{ erg}, \tag{6.1}$$

where D is in kilometres (see Wood, 1979). The mass loss and deceleration in the atmosphere is negligible for these large crater-producing objects ($m > 10^9$ g), so V can be equated to V_O, the velocity of the body just outside the Earth's atmosphere.

Meteoriticists are more interested in the $10^4 < m < 10^9$ g range which are significantly retarded in the atmosphere. Here,

$$m_f = m_o exp\left[-0.5\,\sigma\,(V_O^2 - V_f^2)\right] \tag{6.2}$$

where σ is the mean ablation parameter along that part of the trajectory where the majority of the mass loss occurs (typical values being between 0.02 and 0.03 s^2km^{-2}), m_f is the final mass that impacts with the ground, m_o is the mass of the body just outside the Earth's atmosphere and V_f (km s^{-1}) is the velocity at which ablation ceases (see Hughes, 1992).

Meteoriticists and astroblem geophysicists usually make an informed guess as to the value of V_O, but in the following analysis the aim is to be more specific.

The ease with which a Near-Earth Asteroid is discovered increases as a function of its size and albedo. Huge numbers of NEAs wait to be found. The present collection of NEAs ranges in absolute magnitude, H, between 4954 Eric, at 12.5 and 1991 BA at 28. Helin (1992) concluded that the NEA population is not even complete in the $13 < H < 14$ region. Note that a typical relationship between asteroidal diameter, D km, geometric visual albedo, p_v, and absolute magnitude H is

$$\log\,(0.25\,D^2 p_v) = 5.642 - 0.4H \tag{6.3}$$

[see Zellner and Bowell (1977)]. As the mean albedo of Aten and Apollo asteroids is 0.25 [using, for example, the data in table III of McFadden, 1989, and the suggestion made by Gradie & Tedesco (1982) that the inner regions of the asteroid belt are predominantly populated by S-type asteroids] the equation above becomes

$$\log D = 3.451 - 0.2H \ . \tag{6.4}$$

So $13 < H < 14$ corresponds to $6.7 > D > 4.2$ km.

Uncertainties in the albedo and the absolute magnitude coupled with the fact that asteroids are irregularly shaped and the quoted diameter is the diameter of a sphere having the same surface area, lead to the estimated error in the value of D obtained from equation 6.4 being about ±30%. As time has progressed more NEAs have been discovered. In 1991 the Palomar Planet-Crossing Asteroid Survey (see Helin, 1992) was discovering NEAs at a

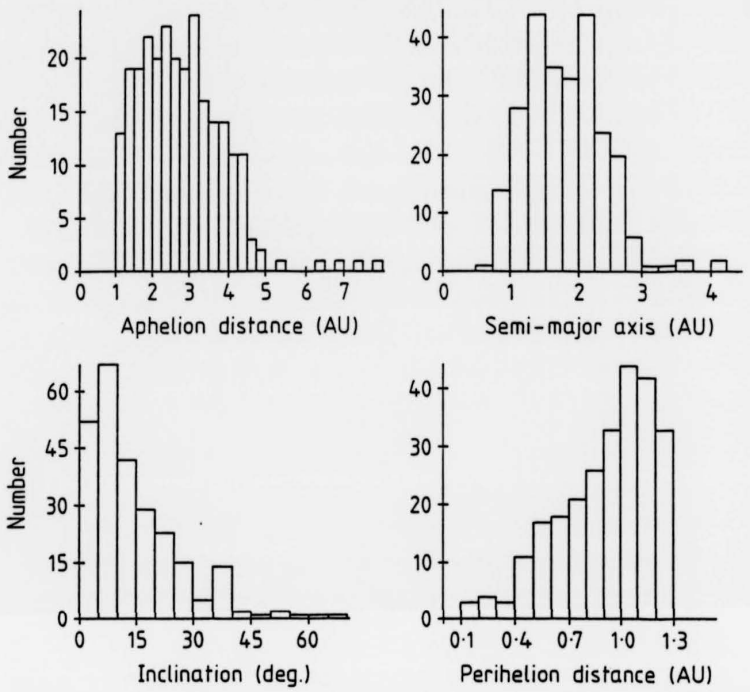

Figure 6.2: The distribution of the major orbital parameters of the 255 Near-Earth Asteroids.

rate of about one per month and the rest of the world was discovering NEAs at about the same rate. When the following analysis was carried out there were 255 NEAs (i.e. those with $q < 1.3$ AU) whose orbits had been calculated. The distribution of the major orbital parameters of the 255 NEAs are shown in Fig. 6.2. The aphelion distances are reasonably well scattered throughout the asteroid belt and the inclination distribution echoes that of the more-normal main belt asteroids. As one would expect the majority of known NEAs have perihelia around 1 AU. The perihelion distribution suffers greatly from observational selection for perihelia greater than 1 AU and the drop-off in observed numbers with increasing perihelion distance is thought to be entirely false. The perihelion distribution also suffers from observational selection for perihelia less than 1 AU, although not to such a great extent as those NEAs with $q > 1$ AU. The orbits of the $q < 1$ AU group of NEAs pass within the Earth's orbit and they may be discovered during a favourable 'close approach' to Earth.

6.2.1 The Earth-impact velocity distribution

Out of the list of 255 NEAs a subset of 136 have $q \leq 1.0$ AU. The orbital parameters and estimated diameters of these asteroids are listed in Appendix C. The mean diameter of this

group of asteroids is 1.31 km.

Thankfully these asteroids have, as yet, not hit Earth. In the following analysis the 136 Earth crossing asteroids are *made* to collide with the Earth by adjusting each asteroid's orbital argument of perihelion, ω, until the asteroid orbit and the Earth's orbit intersect. This is a reasonable approach to the problem as, in reality, secular planetary perturbations cause asteroid orbits to precess in argument of perihelion and longitude of ascending node. This method creates two possible collision points, as ω can be rotated in either direction to produce the desired effect. As the Earth's orbit is assumed, however, to be circular, with $a = 1.0000$ AU, the collision geometries at the two possible points of intersection are identical. The heliocentric velocity, V_H, of the colliding asteroid is given by

$$V_H = 29.78\sqrt{\frac{2}{r} - \frac{1}{a}} \quad \text{km s}^{-1} \tag{6.5}$$

where the heliocentric distance, r, is taken to be 1 AU and a is the semi-major axis of the asteroid's orbit. Taking into consideration the inclination of the asteroid's orbit and the asteroid-Earth collision geometry, this velocity is then added vectorially to the Earth's heliocentric velocity to give the geocentric velocity, V_G. The intersection velocity V_O is greater than V_G due to the enhancement produced by the Earth's gravitational attraction. So

$$V_O^2 = 2GM_E R_E^{-1} + V_G^2 = 125 + V_G^2 \tag{6.6}$$

where both velocities are in km s^{-1} and M_E and R_E are the mass and radius of the Earth respectively. Values of V_G and V_O are also listed in Appendix C.

The mean intersection velocity V_O is found to be 20.8 km s^{-1} and the standard deviation of the data about the mean value is 6.2 km s^{-1}. The distribution of V_O values is shown in Fig. 6.3. There is a hint that the data is skewed towards lower velocity values, but it must be remembered that no asteroid can hit the Earth at a velocity of less than the Earth's escape velocity of 11.2 kms^{-1}.

An examination of the list of NEAs in Appendix C indicates that, in general, the smaller asteroids hit Earth with lower velocities than the larger ones. It is thus expected that, as more NEAs are discovered, both the mean Earth-impact velocity and the mean NEA diameter will decrease. This conclusion strongly suggests that the observed distribution of the orbital parameters of the NEAs is dependent on asteroid size.

In order to check this hypothesis the NEAs were sorted in order of diameter and then divided into 8 bins each of which contained 17 asteroids. The mean estimated diameters, D_m km, and the mean Earth-impact velocities, V_O km s^{-1}, were calculated for each bin and these are plotted in Fig. 6.4. The smaller asteroids clearly have lower Earth-impact velocities.

Fig. 6.5 shows the orbital eccentricities of all the 255 Near Earth Asteroids as a function of (a) their estimated diameters and (b) their perihelia. If it is assumed that the orbits have zero inclination, then orbits with low eccentricities will result in low Earth-impact velocities simply because both the collision angle and asteroid heliocentric velocity will be relatively low. Fig.

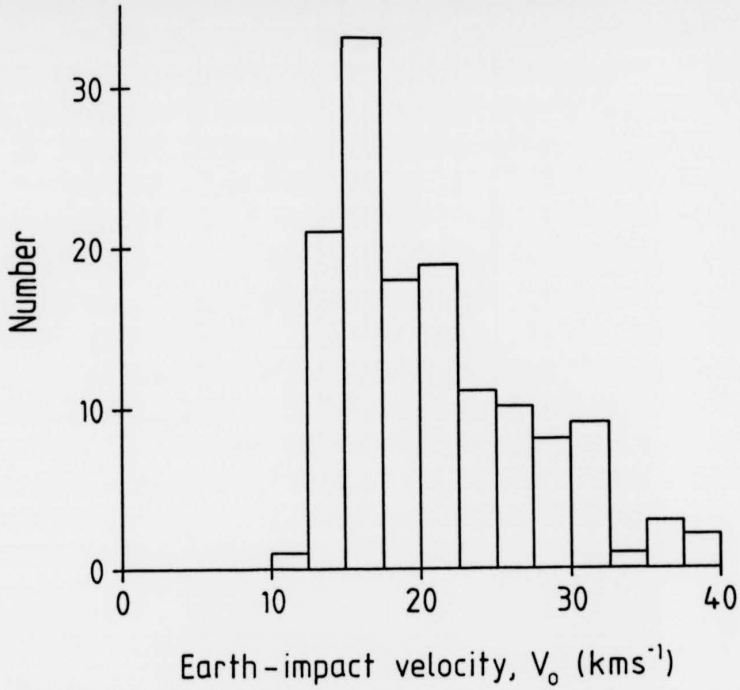

Figure 6.3: The histogram shows the distribution of NEA impact velocities with the Earth. The mean Earth-impact velocity is 20.8 km s^{-1}.

6.5(a) reveals that the least eccentric orbits ($e < 0.225$) are for those NEAs with estimated diameters less than about 2 km although it can be seen that these low diameter asteroids can also have high orbital eccentricities ($e > 0.675$). However, an examination of Fig. 6.6 shows that there is an asymmetry in the observed eccentricity distribution of low diameter NEAs, biased towards lower orbital eccentricities. Larger ($D_{mean} > 1$ km) NEAs tend to be distributed around an eccentricity of about 0.5. Rabinowitz (1993) stated that small NEAs have lower orbital eccentricities and perihelia near the orbit of the Earth. Preliminary physical studies of some of the small NEAs also indicates that they have significantly different colours to the larger NEAs and to the main belt asteroids (Rabinowitz et al. 1993).

Fig. 6.5(b) shows a plot of asteroidal eccentricity against asteroidal perihelion distance for the 255 NEAs. The general trend indicates that NEAs with the lowest perihelia tend to have the highest orbital eccentricities. i.e. the orbital eccentricity must be high in order to bring the asteroid orbit to the inner terrestrial planet region. NEAs with $e > 0.225$ are represented by the full range of asteroidal diameters ($0 < D \leq 8$ km), although the observed numbers are somewhat depleted for perihelia less than around 0.5 AU and NEAs with eccentricities greater than around 0.8 tend to have diameters greater than 1 km. This is probably due to the fact that NEAs with low q (and hence high e) are most likely to be discovered when they are close to the Earth's orbit. This 'discovery factor' is also probably a function of the geocentric velocity of the NEA and the inference from this is that observational selection increases with

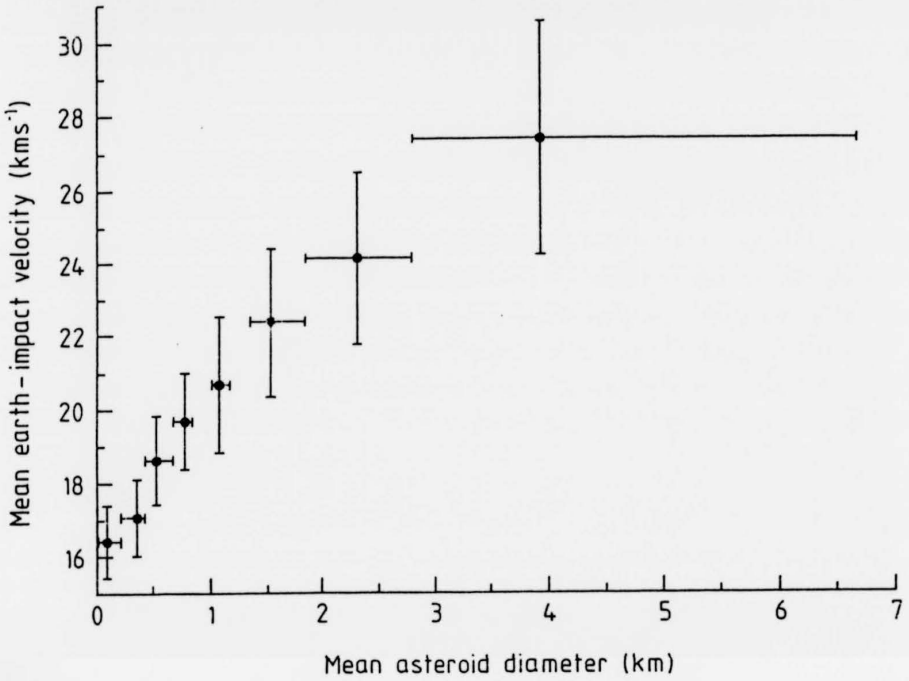

Figure 6.4: A plot showing the relationship between mean Earth-impact velocity and mean asteroid diameter. The horizontal bars represent the extent of the diameter data in each bin, whereas the vertical bars correspond to the standard deviation of the bin impact-velocity data about the mean.

decreasing perihelion distance (and increasing eccentricity). This would suggest that the low eccentricity bias is caused by the observational selection of low diameter bodies with relatively high perihelia ($\simeq$ 1 AU). NEAs with $e < 0.225$ do indeed tend to occupy only a limited perihelion distance range ($0.75 < q < 1.3$ AU) 'centred' around 1 AU. As this group of NEAs also have $D \leq 2$ km, the immediate conclusion is that these small bodies are only discovered because their perihelia lie close to the Earth's orbit. A question then arises as to why there are no NEAs with $D > 2$ km in this $e < 0.225$ group. The answer to this question will probably involve some dynamical property of small NEAs.

The very long-term action of the Poynting-Robertson effect would produce just such a decrease in eccentricity with decreasing asteroidal diameter but it is found that the magnitude of the effect for the asteroids concerned (i.e. those with $0.01 < D < 2$ km) is far too small to account for the phenomenon, even over the whole age of the solar system, a time interval that is much longer than the typical time between close approaches to terrestrial planets (some 10^3 to 10^4 years) and the eventual collision or ejection of the asteroid.

An alternative scenario is the production of a low diameter population due to catastrophic disruption of NEA fragments. A simple collisional fragmentation model in which a parent

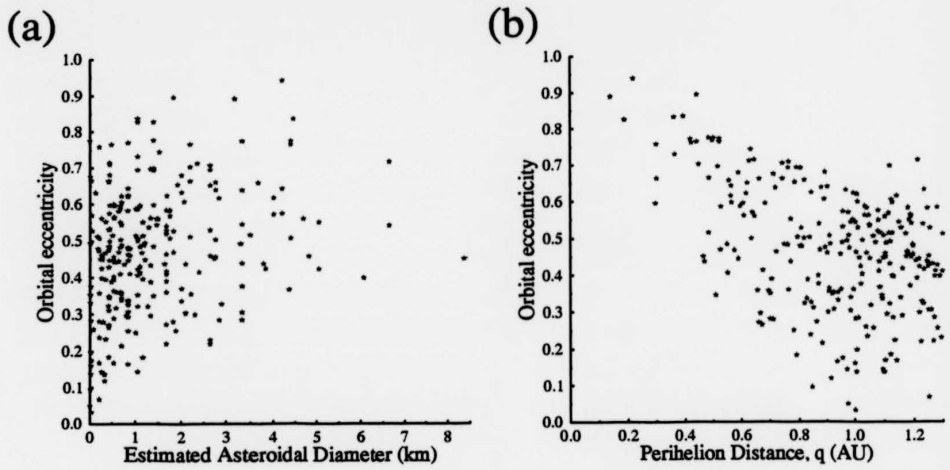

Figure 6.5: A plot of Near Earth Asteroid orbital eccentricity as a function of (a) estimated asteroid diameter and (b) perihelion distance.

body is broken up into a host of daughter fragments is illustrated in Fig. 6.7. The parent asteroid has been given an initial orbit with $e = 0.25$ and $q = 1.0$ AU ($Q = 1.67$ AU) i.e. the parent body already describes an Apollo-type orbit. The body is broken up near its aphelion. During the fragmentation process it has been assumed that fragments are ejected in all directions, in the plane of the asteroid orbit, with an ejection velocity of 0.2 km s^{-1}. Fig. 6.7 shows that, under these conditions, the fragments are given a wide range of orbital eccentricities, with the majority of fragments attaining eccentricities near the upper and lower limits. This is found to be true for any initial parent asteroid orbit. If NEAs are catastrophically disrupted and some of the resulting NEA fragments themselves are also catastrophically disrupted, then the end-product could be a population of low diameter, irregular bodies with a wide range of eccentricities. Only those bodies with perihelia relatively close to the Earth's orbit will be easily detected.

The population of NEAs with $e < 0.225$ have also become collisionally decoupled from the main belt. The lifetimes of this group of asteroids becomes dominated by collisions with terrestrial planets instead of catastrophic fragmentation by smaller main belt projectiles. These increased lifetimes may explain the build-up of the population of small, low eccentricity objects near the Earth.

6.3 Estimating s from Lunar impact-cratering evidence

The number of Lunar impact craters, N_{cr}, with diameters greater than D_{cr} km can be well represented by an empirical relation of the form

$$\log N_{cr} = 1.6 - 2.0 \log D_{cr}, \qquad \log D_{cr} > 0; \tag{6.7}$$

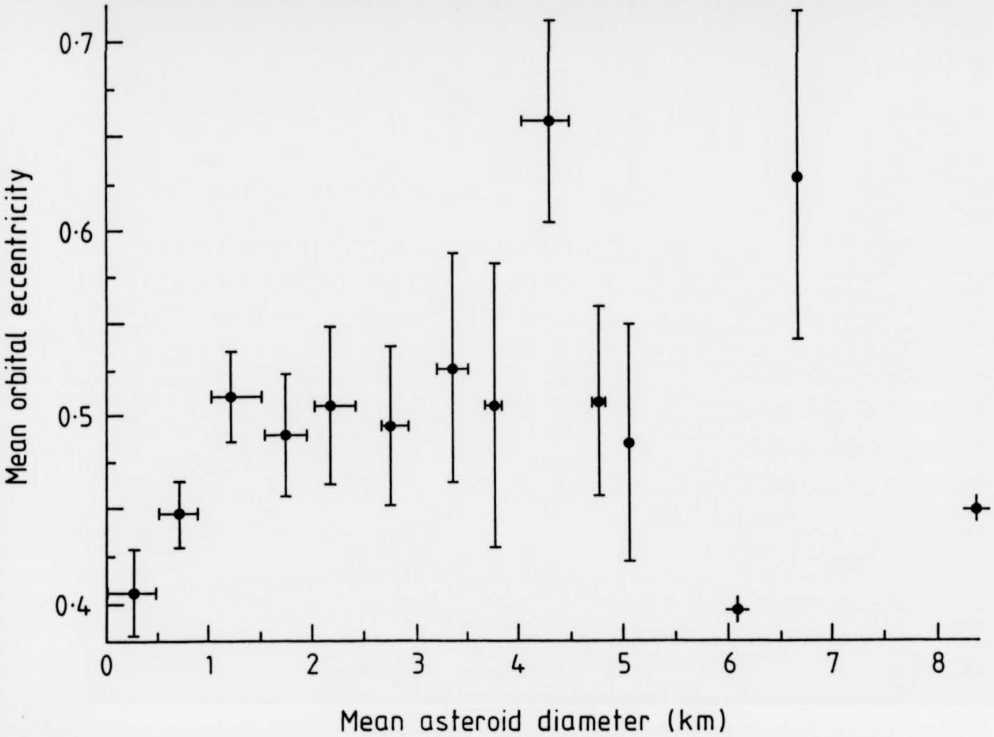

Figure 6.6: A plot showing the relationship between mean orbital eccentricity and mean asteroid diameter. The horizontal bars represent the extent of the diameter data in each bin, whereas the vertical bars correspond to the standard deviation of the bin eccentricity data about the mean.

down to a crater diameter of approximately 1 km [see Shoemaker (1965) and Hartmann (1965)]. Below diameters of 1 km the statistics begin to be significantly influenced by secondary impact cratering. The power law, such that N_{cr} is proportional to D_{cr}^{-2}, is strongly supported by similar power laws that have been found to apply to terrestrial (Grieve, 1984; Hughes, 1994) and martian (Neukum & Wise, 1976) crater distributions.

A number of researchers have attempted to establish a relationship between the energy of an impacting body and the diameter of the resulting crater. Five of these relationships, considering the formation of terrestrial craters, are as follows.

$$E = 8.41 \times 10^{23} D_{cr}^{3.57} \text{ erg } (D_{cr} > 1 \text{ km}) \text{ (Wood, 1979)} \tag{6.8}$$

$$E = 4 \times 10^{22} D_{cr}^{3} \text{ erg (Allen, 1973)} \tag{6.9}$$

$$E = 1.45 \times 10^{23} D_{cr}^{3} \text{ erg } (D_{cr} < 2.4 \text{ km}) \text{ (Dence et al., 1977)} \tag{6.10}$$

$$E = 1.01 \times 10^{23} D_{cr}^{3.4} \text{ erg } (D_{cr} > 2.4 \text{ km}) \text{ (Dence et al., 1977), and} \tag{6.11}$$

$$E = 8.71 \times 10^{22} D_{cr}^{3.25} \text{ erg } (0.09 < D_{cr} < 140 \text{ km}) \text{ (Hughes, 1994)} \tag{6.12}$$

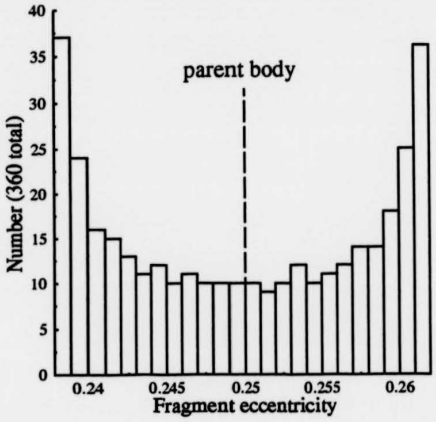

Figure 6.7: The histogram shows the eccentricity distribution of daughter fragments after the modelled break-up of a hypothetical parent body. The parent asteroid had an original orbital eccentricity of 0.25. The daughter fragments have been ejected with a velocity of 0.2 km s^{-1} over all orbital-plane directions (with ejection angle increments of 1°).

Where the crater diameter, D_{cr}, is in km.

The energy of the impactor is entirely kinetic. The mean collision velocity, V_{cm}, between a Near-Earth-Asteroid (NEA) and the Moon is found to be 18.9 km s^{-1}. If we assume an energy-crater diameter relationship as given by equation 6.12, the corresponding equation for Lunar impact craters is given by

$$0.5 M_{ast} V_{cm}^2 = 8.74 \times 10^{15} D_{cr}^{3.25} \quad \text{J} \tag{6.13}$$

It is now a simple calculation to convert the impact-crater diameter data into impactor diameter data (assuming that the impactors are all spherical in shape and have a constant density of 3600 kg m^{-3}).

A plot of $\log N_{ast}$ versus $\log D_{ast}$ is shown in Fig. 6.8, where N_{ast} is the number of asteroids with diameters greater than D_{ast} km. A least square fit to the data points leads to

$$\log N_{ast} = -1.91(\pm 0.03) \log D_{ast} - 1.29(\pm 0.03) \tag{6.14}$$

This indicates that the mass distribution index, s, is 1.64±0.01. Hughes (1994) concluded that the mass distribution index for *Earth* impact-cratering bodies was 1.62 ± 0.03. When these results are compared to the *observed* asteroidal mass distribution index that was calculated in the previous chapter there is a large discrepancy. However, it must be remembered that the observed asteroid mass distribution index only applies to Main Belt asteroids with diameters greater than 130 km. The asteroids responsible for planetary and satellite impact-craters are (were) NEAs and not Main Belt asteroids. The present day observed NEAs have diameters, D_{NEA}, in the $0.01 < D_{NEA} < 7$ km range and their mass distribution index is presently unknown (it is not clear whether the mass distribution index calculated above applies to the

present day population of NEAs or just to the population of bodies that formed the observed impact-craters).

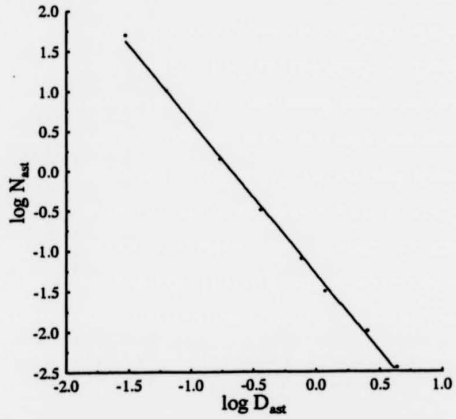

Figure 6.8: The diameter (mass) distribution of Lunar-impacting asteroids plotted on logarithmic scales. N_{ast} is the number of asteroids with estimated diameters greater than D_{ast} km. The straight line is a least square fit to the data points and the gradient is -1.91 ± 0.03.

It is generally proposed that the present asteroidal population is the product of multiple collisional fragmentation and that the population is in quasi-equilibrium. Thus it is assumed by most researchers that the mass distribution index of around 2 also applies to Main Belt asteroids with diameters less than 130 km. It is difficult to envisage any physical process that would change this index as a function of asteroid mass (except for the PR effect, although, as mentioned earlier, the timescales for this effect are too large). Extrapolations have been made down to diameters of 0.1 km and even 0.001 km. Morrison and Bowell (see Morrison, 1993), however, disagree and have concluded that the mass distribution index varies with asteroidal diameter. In *The Spaceguard Survey* they have assumed that the mass distribution of NEAs was 1.87 in the $D_{NEA} < 0.25$ km range, 1.67 in the $0.25 < D_{NEA} < 2.5$ km range and 2.43 for the $D_{NEA} > 2.5$ km range. The incompleteness of the data in this diameter region and the uncertainties involved with asteroidal diameter estimations deems this suggestion unverifiable at present.

Chapter 7

Summary and further work

7.1 Summary of work done

Chapter 2 of this thesis discussed the relationship between meteoroid streams and meteor showers and a method was described for identifying stream meteoroids from a random meteoroid orbital parameter data set (the D' criterion). The sporadic to stream meteoroid ratio was then estimated for a specific photographic meteor data set (meteors listed in the IAU Photographic Meteor Data Catalogue that occurred between July 23 and August 23) using three different methods. The average ratio was found to be 0.17 ± 0.04 and it was also found that $27 \pm 3\%$ of the general sporadic background comprises of undetected stream meteoroids. The orbital distributions of stream and sporadic meteoroids were compared to those of the known short-period comets and, as was to be expected of meteoroids of cometary origin, the distributions were fairly similar. The orbits of each of the 136 known short-period comets were replaced with a modelled 'typical' meteoroid stream and the intersection velocity distribution of these meteoroids with Earth and Mars was determined. The 'cosmic weighting factor' was then introduced to make up for the relative paucity of low-velocity meteoroids observed.

Chapter 3 investigated the relationship between the mass and semi-major axis of Perseid meteoroids. The 'core' Perseid meteoroids were identified from the IAU Photographic Meteor Data Catalogue using the D' method described in Chapter 2. It was found that there is no systematic variation in the spread of the semi-major axis data as a function of meteoroid mass. This result was confirmed by analysing Geminid meteoroids in a similar manner. It was thus concluded that the meteoroid cometocentric ejection velocity is also independent of meteoroid mass and that the meteoroid radius-density product is a constant.

Chapter 4 was concerned with modelling the formation of the Perseid meteoroid stream via dust ejection from the nucleus of parent comet P/Swift-Tuttle. The meteoroid cometocentric ejection velocity, emission plane orientation and sublimation activity are all factors that were considered. The model that produced a semi-major axis distribution that favourably

agreed with the observations used a Maxwellian meteoroid ejection velocity distribution that peaks at a velocity of 0.6 km s^{-1} and a meteoroid ejection lag angle of $-5°$. It was thus concluded that the nucleus of P/Swift-Tuttle spins slowly in a prograde mode. In addition it was calculated that around 14% (by number) of the dust particles lost by the comet are forced onto hyperbolic orbits and are lost from the solar system. The ecliptic distribution of modelled meteoroid descending nodes was determined and the relative influx of Perseid meteoroids as the Earth passes through the stream was calculated. As expected, the vast majority of modelled Perseid meteoroids are encountered between August 11 and August 13.

The last part of Chapter 4 improved the stream formation model by including the past orbital evolution of the parent comet. The orbit of P/Swift-Tuttle was integrated backwards in time for 270,000 years by Kevin Yau (private communication). It was estimated that the observed Perseids started forming around 160,000 years BP. Modelled Perseid meteoroids were thus ejected from the parent comet orbit at every 5000 year interval of orbital evolution from 160,000 BP to the present day. The ecliptic distribution of modelled meteoroid descending nodes was again determined and this indicates that the Earth only intersects the 'inner edge' of the dust complex, although it does pass close to the centre of the most recently formed concentration of meteoroid orbits. A new estimate of the Perseid meteoroid influx to the Earth produces a slow, erratic build-up from August 3 to maximum activity followed by a much steeper decline to negligible numbers by August 17. This is what is observed in reality. Finally the modelled Perseid meteor radiant distribution was determined and compared with the observed radiant field.

The second part of this thesis was devoted to my research work in the field of asteroids. Chapter 5 reviewed the spatial and size distribution of main belt asteroids and the mass distribution index was found to be 2.09 ± 0.1. Using this result the total mass of the asteroid belt was estimated to be around 1.6×10^{26} g and it was concluded that the Trojan asteroid population is a significant element of the solar system. A method was developed to determine the mass of the Koronis asteroid family parent body. The resulting mass depends on the value adopted for the smallest Koronis family fragment. The collisional history and the collision velocity distribution of the family was investigated.

The orbital and size distribution of Near Earth Asteroids (NEAs) was investigated in Chapter 6. NEA nomenclature and potential sources were briefly discussed. Using an orbital data set of 255 NEAs, the mean Earth-impact velocity was found to be 20.8 km s^{-1}. An anomalous population of low diameter (< 2 *km*), low eccentricity ($e < 0.225$) NEAs with perihelia near to 1 AU were found. Some possible explanations for these observations were discussed. The size distribution of Lunar impact-craters was used in order to estimate the mass distribution index of NEAs in the past. The index was found to be 1.64 ± 0.01. It is unknown whether this index applies to the present-day population of NEAs.

7.2 Further work

The majority of this thesis has been concerned with meteoroid streams and their formation mechanism. The dust ejection model based on the past orbits of P/Swift-Tuttle (developed in Chapter 4) could be improved and expanded in a number of ways. Firstly, more observed Perseid meteoroid orbits are required. These also need to be of greater accuracy, especially for the case of the meteoroid mass and semi-major axis distribution. With a data file of say 500 photographic Perseid meteoroids with accurate orbital parameters and masses, observed between solar longitudes of 135° and 145°, we could really tie down the cometary emission process.

Due to the limitations of time and facilities, the variable emission parameters (ejection velocity, heliocentric emission function and sub-solar point emission function) were not analysed in any great detail. A future model, instead of using a fixed mean ejection velocity of 0.6 km s^{-1}, may use a mean ejection velocity that varies with heliocentric distance, r, according to a function of the type $\overline{V} = V_0 r^{-x}$. V_0 is likely to be around 0.58 and the value of x is likely to be around 0.5 (see equation 4.5). This means that meteoroids ejected at higher heliocentric distances (say > 1.5 AU) would be given lower mean ejection velocities (< 0.58 km s^{-1}). This would have the effect of removing the first few outer contours in the ecliptic footprints shown in Chapter 4 and increasing the central concentration of descending nodes.

The r^{-2} heliocentric emission function could also be adjusted so that the relationship either weakens to, say, $r^{-1.5}$ or strengthens to r^{-5} and beyond (as was observed during the 1992 perihelion passage of P/Swift-Tuttle [see Mobberley, 1994]). A heliocentric activity factor such as the latter would render pre- and post-perihelion emission fairly insignificant and this would give the meteoroid stream formation mechanism an 'anchor point' at perihelion (where the vast majority of dust would be ejected). A simple $\cos\alpha$ sub-solar point emission function is used in the present model. Other emission functions could be experimented with, e.g. a $(\cos\alpha)^{0.25}$ function is derived by equating received to emitted energy.

As the ejection velocity is assumed to be independent of meteoroid mass, (perhaps due to a high meteoroid surface area to mass ratio), a mass distribution index could be applied to the ejected meteoroids to give an indication as to the particle size distribution within the stream. The present model does not include the influences of gravity, radiation pressure and the PR effect on the orbits of the modelled meteoroids. These effects are small in the short-term, but over a period of tens of thousands of years the effects may become significant, especially for the case of gravitational perturbation. A future model will have to include all three influences.

An interesting use of the dust ejection model would be to apply it to each of the present-day short-period comets (and perhaps some of the Apollo-Amor-Aten extinct/dormant comet candidates) in order to produce a realistic representation of the large particle (> 1 mg)

cometary dust cloud as it exists today. A potential problem with this might be to decide the (relative) mass values for the comets. This problem could perhaps be overcome by associating an absolute magnitude H_{10} with each parent body and thus a mass weighting factor for each associated modelled meteoroid stream. This dust distribution model could be used to estimate the influx of large meteoroids to an orbiting body, such as a cometary nucleus, a planet or a spacecraft, as a function of its position in the solar system.

Appendix A

Orbital parameters

The dimensions and orientation of a Keplerian orbit are described by the orbital parameters a, e, q, Q, i, ω, Ω and Π (or L). A diagrammatic representation of an elliptical orbit is shown below (taken from Richter, 1963)

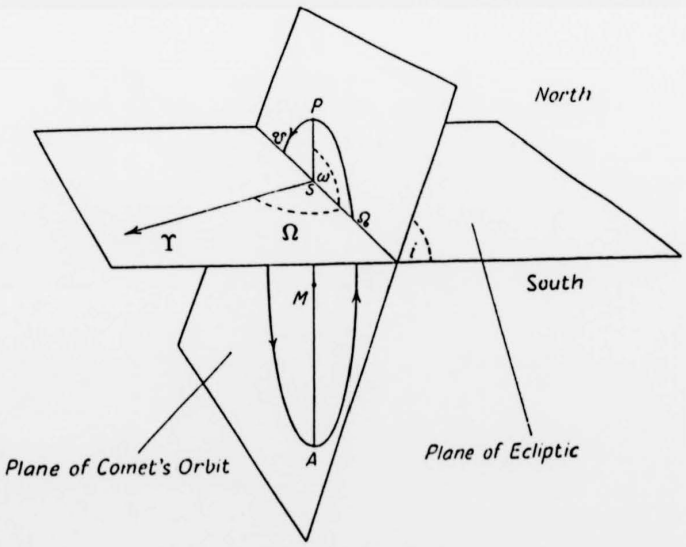

Orbital parameters:

a = PM = semi-major axis (AU).

e = SM/PM = eccentricity.

q = PS = perihelion distance (AU).

Q = AS = aphelion distance (AU).

i = inclination (degrees).

ω = argument of perihelion (degrees).

Ω = longitude of ascending node (degrees).

$\Pi = \omega + \Omega$ = longitude of perihelion (degrees).

where,

S = the Sun

Υ = the First Point of Aries (Vernal Equinox)

M = the centre point of the orbit

P = perihelion (the nearest point of the orbit to the Sun)

A = aphelion (the furthest point of the orbit from the Sun)

Ω = ascending node (point where the orbit intersects the ecliptic plane moving South to North)

$\mho$ = descending node (point where the orbit intersects the ecliptic plane moving North to South)

The linear orbital parameters can be related to one another by the following expressions:

$$q = a(1 - e)$$

$$Q = a(1 + e)$$

The period, P, of a body on an orbit of semi-major axis a AU is given by

$$P = a^{3/2} \text{ years}$$

The heliocentric distance of a body when at true anomaly of θ (where θ is the angle perihelion–Sun–body) is given by

$$r = \frac{a(1 - e^2)}{1 + e\cos\theta}$$

The velocity, V, of a body on an orbit of semi-major axis a AU at heliocentric distance r AU is given by

$$V = 29.78\sqrt{\frac{2}{r} - \frac{1}{a}} \text{ km s}^{-1}$$

Appendix B

Orbital parameters of 52 Koronis-family asteroids

The orbital parameters and physical properties of 52 Koronis family members are listed in order of increasing absolute magnitude. The asteroid diameters, D km, have been estimated by using equation 5.8 which assumes a constant surface albedo of 0.21 (S-Type). Asteroids whose spin periods have not been estimated are assigned a spin period of 0.00.

No.	a (AU)	e	i (°)	Ω (°)	ω (°)	Mag.	D (km)	Spin P. (hr.)
462	2.87164	.088022	3.1922	105.5265	250.4101	9.01	47.2	8.6
208	2.89266	.010723	1.7545	4.8648	112.6707	9.05	51.8	13.5
167	2.85228	.036807	2.2041	166.6205	131.2148	9.16	49.4	16.00
158	2.86967	.051891	1.0015	279.1821	142.3251	9.49	43.1	14.18
720	2.88581	.018568	2.3665	36.1115	114.8996	9.53	37.5	14.49
534	2.88412	.057958	3.2772	94.4514	338.7176	9.81	37.5	9.39
277	2.88349	.092441	1.1558	232.1868	135.4901	9.96	34.2	30.00
243	2.86166	.042061	1.1412	324.7228	110.9907	10.02	34.2	4.65
1245	2.89110	.082642	2.8827	152.0954	206.7754	10.05	32.7	4.855
311	2.89812	.004392	3.2270	81.3142	78.3239	10.09	32.7	11.48
321	2.88732	.047072	2.5957	40.6103	36.4285	10.20	31.2	2.87
975	2.83460	.031684	2.5658	39.0317	55.3306	10.38	28.4	0.00
263	2.88964	.076910	1.3052	217.0809	161.6259	10.52	27.2	14.22
658	2.85279	.065975	1.5148	351.5169	59.8452	10.56	25.9	28.00
1350	2.85694	.089548	2.9325	139.8656	236.9609	10.62	25.9	6.0
1289	2.86009	.062869	1.6054	193.5947	116.3515	10.64	25.9	3.6
1223	2.86881	.058226	2.5544	41.2161	14.2972	10.66	24.8	8.78
811	2.89644	.071491	3.1324	131.2154	177.2986	10.8	23.7	5.58
761	2.86326	.064650	2.1689	24.2009	297.2508	10.91	22.6	0.00
1336	2.84931	.064203	3.1964	97.6728	219.3258	10.93	22.6	0.00
1029	2.88865	.028304	2.4382	30.3541	142.0412	10.95	22.6	15.37
1482	2.87441	.035416	2.9764	71.4288	212.5933	10.97	21.6	10.45
1725	2.90295	.088539	3.1690	119.5059	227.8930	11.0	20.6	0.00
1913	2.87969	.077269	1.5780	359.1626	33.2270	11.2	19.7	0.00
832	2.86730	.079280	1.0010	255.3364	120.5328	11.20	19.7	18.82
1423	2.86053	.078061	2.9127	58.8912	319.9565	11.23	19.7	0.00
1100	2.89663	.070078	1.0379	304.9888	21.6642	11.25	18.8	0.00
1079	2.87401	.049465	1.1873	330.0677	104.6251	11.25	18.8	7.3
1848	2.87029	.045718	1.4468	332.5239	313.7962	11.41	17.9	0.00
1741	2.88405	.069797	2.8979	55.8325	337.1789	11.5	17.1	0.00
1442	2.87428	.076610	1.2456	221.6775	125.1203	11.6	16.4	0.00
1618	2.86810	.028197	3.2261	103.1433	182.7190	11.6	16.4	0.00
1835	2.83274	.087143	0.9933	297.6692	77.4117	11.6	16.4	0.00
1363	2.90183	.066620	1.0917	215.5500	107.7704	11.60	16.4	0.00
962	2.90589	.097579	2.5969	145.8852	222.7657	11.61	16.4	0.00
1635	2.85710	.057022	1.8041	184.8463	134.2428	11.62	16.4	0.00
1389	2.86715	.016494	2.0336	174.9097	293.3863	11.64	16.4	22.5
1762	2.87496	.077562	2.2697	161.0216	232.1700	11.7	15.6	0.00
1824	2.88397	.043385	1.9383	15.4070	67.0936	11.7	15.6	0.00
2051	2.84138	.075068	1.3401	215.8348	172.3294	11.7	15.6	0.00
1802	2.84213	.037705	2.6808	142.8251	295.7936	11.72	15.6	0.00
1497	2.89322	.082791	1.0642	301.0957	27.8243	11.8	14.9	0.00
1878	2.84618	.010788	1.7703	188.2132	289.8401	11.88	14.3	0.00
1742	2.88865	.096854	2.4880	152.4653	213.0699	11.88	14.3	8.56
1912	2.90296	.091495	3.1615	76.5961	317.3125	12.0	13.6	0.00
1745	2.84725	.056124	3.2599	79.0108	339.3356	12.00	13.0	0.00
993	2.86297	.048483	1.7652	184.6878	250.0223	12.02	13.6	0.00
1570	2.84468	.056036	1.6550	190.4614	223.5950	12.07	13.0	0.00
1955	2.85455	.064305	1.0005	258.9782	152.7332	12.08	13.0	0.00
452	2.84566	.014606	3.2261	92.8001	70.6948	12.2	11.9	0.00
1774	2.87641	.068845	1.8465	175.6383	249.0489	12.2	12.4	0.00
1894	2.88713	.071586	0.9048	258.9975	114.2651	12.3	11.9	0.00

Appendix C

Orbital parameters of 136 Earth-crossing asteroids

The orbital parameters of 136 known Earth-crossing asteroids are listed in order of asteroidal classification number:

Ast.No.	q (AU)	Q (AU)	a (AU)	i (°)	V_G km s^{-1}	V_O km s^{-1}	D (km)
1566	0.18682	1.96928	1.07805	22.8803	29.75	31.79	1.39
1620	0.82727	1.66231	1.24479	13.3196	11.59	16.12	2.01
1685	0.77103	1.96325	1.36714	9.3743	13.07	17.21	3.78
1862	0.64736	2.29485	1.47111	6.3514	16.94	20.31	1.49
1863	0.89083	3.63033	2.26058	18.4160	16.00	19.53	2.07
1864	0.56269	2.35908	1.46089	22.1746	22.11	24.79	2.84
1865	0.57570	1.58463	1.08017	16.0938	16.55	19.98	1.14
1866	0.87225	2.91459	1.89342	41.1628	25.42	27.78	6.65
1981	0.62171	2.93032	1.77602	39.8378	27.99	30.15	2.65
2062	0.79013	1.14313	0.96663	18.9343	11.03	15.72	1.16
2063	0.70114	1.45407	1.07761	9.4191	11.66	16.17	1.39
2100	0.46886	1.19521	0.83204	15.7623	13.93	17.88	1.63
2101	0.44196	3.30890	1.87543	1.3526	24.97	27.36	0.48
2102	0.90484	1.67534	1.29009	64.0096	33.66	35.47	2.31
2135	0.79485	2.40477	1.59981	23.0443	17.97	21.17	0.68
2201	0.62873	3.72210	2.17541	2.5149	20.40	23.27	2.36
2212	0.36105	3.97495	2.16800	11.7769	28.99	31.08	4.46
2329	0.81899	3.98381	2.40140	24.4284	20.24	23.14	2.77
2340	0.46429	1.22369	0.84399	5.8599	12.74	16.97	0.23
3103	0.90725	1.90494	1.40610	20.9406	13.92	17.87	2.22
3200	0.13959	2.40295	1.27127	22.0958	33.48	35.31	3.18
3360	0.63405	4.29628	2.46517	21.7377	23.88	26.38	1.52
3361	0.81923	1.59936	1.20929	2.6881	9.12	14.44	0.41
3362	0.52575	1.45314	0.98945	9.9204	15.15	18.84	0.64
3554	0.70057	1.24689	0.97373	23.3576	14.42	18.26	1.82
3752	0.98608	1.84110	1.41359	55.5520	29.96	31.99	2.10
3753	0.48410	1.51144	0.99777	19.8151	18.53	21.65	3.49
3838	0.44879	2.56052	1.50465	29.2861	26.85	29.09	2.20
4015	0.99660	4.28514	2.64087	2.7840	8.49	14.05	1.68
4034	0.58932	1.53064	1.05998	11.1726	14.80	18.56	0.64
4179	0.90266	4.10991	2.50628	0.4714	12.22	16.57	4.20
4183	0.71855	3.24296	1.98075	6.7632	17.41	20.70	3.33
4197	0.52213	4.07361	2.29787	12.2073	24.66	27.09	3.33
4257	0.87549	2.41871	1.64710	40.7114	24.47	26.91	1.83
4341	0.58973	3.08131	1.83552	11.8691	21.25	24.02	2.01
4450	0.59617	2.28746	1.44181	5.5181	18.15	21.32	1.01
4486	0.74245	3.65467	2.19856	3.0398	17.04	20.39	2.20
4544	0.78128	1.30292	1.04210	14.1425	10.48	15.34	1.01
4581	0.65748	1.38789	1.02268	4.9128	11.15	15.81	0.21
4660	0.95279	2.02621	1.48950	1.4203	6.83	13.12	0.58
4769	0.54948	1.57689	1.06318	8.8808	15.65	19.24	1.10
4953	0.55599	2.68652	1.62125	24.4189	23.76	26.27	3.66
5011	0.81773	2.45220	1.63497	7.3983	13.06	17.21	1.05
5131	0.63920	2.33354	1.48637	36.3779	25.19	27.57	4.01
5143	0.41924	3.24926	1.83425	9.1867	25.88	28.20	4.40
5189	0.80968	2.29195	1.55081	3.5820	12.35	16.68	0.84
5381	0.66710	1.22784	0.94747	48.9712	25.36	27.73	1.33
5496	0.88011	3.98716	2.43364	68.0128	38.75	40.34	2.77

Ast.No.	q (AU)	Q (AU)	a (AU)	i (°)	V_G km s^{-1}	V_O km s^{-1}	D (km)
5590	0.71019	1.26040	0.98529	14.1925	11.03	15.72	0.30
5604	0.55125	1.30307	0.92716	4.7875	12.19	16.55	1.05
1937 UB	0.61768	2.64779	1.63273	6.2173	18.80	21.88	0.70
1950 DA	0.83784	2.52975	1.68379	12.0918	13.73	17.72	2.77
1954 XA	0.50905	1.04570	0.77737	3.9171	7.45	13.45	0.44
1974 MA	0.42343	3.12702	1.77522	37.8459	30.88	32.85	4.40
1978 CA	0.88306	1.36624	1.12465	26.1164	14.93	18.66	0.70
1979 XB	0.64634	3.87843	2.26238	24.8524	23.99	26.48	0.44
1983 LC	0.76438	4.49494	2.62966	1.5216	17.24	20.56	0.44
1983 VA	0.80532	4.41930	2.61231	16.2310	18.28	21.44	1.39
1983 VB	0.95680	2.77987	1.86833	17.6279	13.01	17.17	0.70
1984 KB	0.52228	3.91046	2.21637	4.8524	23.77	26.28	2.20
1984 QY1	0.21825	6.97629	3.59727	17.8798	36.31	38.00	4.20
1986 JK	0.89370	4.70066	2.79718	2.1392	13.11	17.24	0.44
1987 OA	0.60569	2.38737	1.49653	9.0261	18.62	21.73	0.55
1988 EG	0.63552	1.90268	1.26910	3.4869	15.30	18.96	0.44
1988 TA	0.80330	2.27820	1.54075	2.5447	12.42	16.72	0.18
1988 VP4	0.78514	3.74027	2.26270	11.6545	17.04	20.39	1.92
1988 XB	0.76064	2.17487	1.46776	3.1188	13.29	17.38	0.84
1989 AZ	0.87570	2.41624	1.64597	11.7571	12.38	16.70	0.35
1989 DA	0.98660	3.33704	2.16182	6.4431	8.69	14.17	0.70
1989 JA	0.91319	2.62702	1.77010	15.2270	12.94	17.12	1.39
1989 QF	0.67601	1.62712	1.15156	3.9352	12.70	16.94	1.10
1989 UP	0.98222	2.74519	1.86371	3.8626	7.50	13.48	0.20
1989 UR	0.69522	1.46512	1.08017	10.3402	12.06	16.46	0.70
1989 UQ	0.67272	1.15765	0.91518	1.2875	7.47	13.46	0.42
1989 VA	0.29517	1.16221	0.72869	28.8142	19.44	22.43	1.10
1990 HA	0.79152	4.36564	2.57858	3.8878	16.39	19.86	1.05
1990 MF	0.95041	2.54283	1.74662	1.8646	8.23	13.90	0.53
1990 OS	0.90216	2.43611	1.66913	1.1039	9.73	14.83	0.28
1990 SM	0.48427	3.82819	2.15623	11.5691	25.29	27.66	1.39
1990 SP	0.83023	1.87943	1.35483	13.5129	12.47	16.76	1.33
1990 SS	0.89449	2.51171	1.70310	19.3933	14.79	18.55	0.42
1990 TG1	0.76284	4.20436	2.48360	9.0645	17.72	20.96	2.65
1990 UA	0.77113	2.67115	1.72114	0.9698	14.34	18.20	0.35
1990 UN	0.80764	2.61128	1.70946	3.6615	13.27	17.37	0.05
1990 UO	0.29830	2.17002	1.23416	29.3461	28.71	30.81	0.21
1991 AM	0.51692	2.87895	1.69793	30.0313	26.50	28.77	1.33
1991 AQ	0.49818	3.81945	2.15881	3.1933	24.26	26.72	0.84
1991 BA	0.71214	3.66607	2.18911	1.9946	17.90	21.12	0.01
1991 VE	0.29940	1.48173	0.89057	7.2037	20.58	23.43	0.42
1991 BB	0.86307	1.50941	1.18624	38.4790	21.42	24.17	1.67
1991 BN	0.86862	2.01717	1.44289	3.4418	9.75	14.85	0.26
1991 CS	0.93803	1.30781	1.12292	37.1109	19.83	22.77	0.84
1991 CB1	0.68409	2.69053	1.68731	14.5659	18.52	21.64	0.67
1991 DG	0.90931	1.94526	1.42729	11.1585	10.11	15.09	0.53
1991 EE	0.84365	3.64780	2.24572	9.7657	14.83	18.59	0.84
1991 GO	0.66363	3.25663	1.96013	9.6642	19.31	22.33	0.42

Ast.No.	q (AU)	Q (AU)	a (AU)	i (°)	V_G km s^{-1}	V_O km s^{-1}	D (km)
1991 JW	0.91541	1.16129	1.03835	8.7188	5.71	12.57	0.33
1991 LH	0.36446	2.33981	1.35214	52.0550	33.78	35.59	1.05
1991 RB	0.74884	2.15201	1.45043	19.5392	16.97	20.33	0.42
1991 RC	0.18809	1.97343	1.08076	23.1542	29.77	31.80	1.05
1991 TU	0.94188	1.87201	1.40694	7.5599	7.88	13.69	0.01
1991 TB1	0.94209	1.96551	1.45380	23.4630	14.65	18.44	1.05
1991 TB2	0.39421	4.40016	2.39718	8.6402	28.30	30.43	1.05
1991 TF3	0.95857	3.12537	2.04197	14.0482	11.93	16.37	0.42
1991 VA	0.92597	1.93175	1.42886	6.5232	8.27	13.92	0.01
1991 VG	0.97631	1.07728	1.02679	1.4447	1.51	11.30	0.01
1991 VH	0.97300	1.29978	1.13639	13.9153	8.00	13.77	1.05
1991 VK	0.91061	2.77579	1.84320	5.4132	10.58	15.41	1.05
1991 WA	0.56356	2.58949	1.57652	39.6613	28.04	30.19	0.84
1991 XA	0.97795	3.56696	2.27246	5.2676	9.07	14.41	0.04
1992 BC	0.92081	1.90608	1.41345	14.2138	10.84	15.58	0.42
1992 CC1	0.86956	1.91332	1.39144	36.8972	21.75	24.47	3.33
1992 DU	0.95704	1.36263	1.15983	25.0555	13.87	17.83	0.03
1992 HE	0.95927	3.52198	2.24062	37.3656	23.13	25.70	4.20
1992 HF	0.60994	2.16895	1.38945	13.2700	18.40	21.54	0.26
1992 JB	0.99649	2.11717	1.55683	16.0698	10.34	15.25	0.67
1992 LC	0.74206	4.29520	2.51863	17.8410	20.25	23.14	2.65
1992 QN	0.76285	1.61885	1.19085	9.5853	11.62	16.14	1.67
1992 SK	0.84291	1.65423	1.24857	15.3152	11.95	16.38	0.84
1992 SY	0.99370	3.42507	2.20939	8.0234	8.91	14.31	0.67
1992 TB	0.72133	1.96225	1.34179	28.3171	19.92	22.85	0.84
1992 BF	0.66186	1.15402	0.90794	7.2574	8.37	13.98	0.42
1993 DA	0.84625	1.02333	0.93479	12.3250	6.64	13.02	0.01
1993 BW2	0.92638	1.74390	1.33514	21.9167	13.66	17.67	0.84
1993 EA	0.52728	2.01671	1.27199	5.0559	18.67	21.77	1.05
1993 HC	0.97992	2.99726	1.98859	9.3955	9.39	14.61	0.21
1993 KH	0.85038	1.61500	1.23269	12.7467	10.74	15.52	0.42
1993 KA2	0.50166	3.95282	2.22724	3.1879	24.35	26.80	0.01
5025 P-L	0.44232	7.97312	4.20772	6.3544	28.95	31.04	1.83
6344 P-L	0.96975	4.28909	2.62942	4.4815	9.98	15.00	0.13
1993 GD	0.84000	1.36463	1.10231	15.4594	10.63	15.44	0.21
1993 HD	0.48543	2.40480	1.44511	5.7406	21.49	24.23	0.03
1993 HP1	0.97407	2.86831	1.92119	7.7752	8.94	14.33	0.01
1993 PB	0.56503	2.23798	1.40151	39.2533	26.92	29.16	1.39
1993 PC	0.70526	1.60242	1.15384	3.2143	11.82	16.28	0.48
1993 QA	0.98676	1.99454	1.49065	13.5541	9.19	14.49	0.70

Appendix D

Publications

The following publications have resulted from the work contained in this thesis. The last two papers were accepted for publication in early November 1994:

Asteroid-Earth collision velocities.

Harris, N.W. & Hughes, D.W., 1994. *Planet. Space Sci.*, **42**, No. 4, pp 285–289.

The distribution of asteroid sizes and its significance.

Hughes, D.W. & Harris, N.W., 1994. *Planet. Space Sci.*, **42**, No. 4, pp 291–295.

Perseid meteoroids – the relationship between mass and orbital semi-major axis.

Harris, N.W. & Hughes, D.W., 1994. *MNRAS*, in press.

The true extent of the nodal distribution of Perseid meteoroids.

Harris, N.W., Yau, K. & Hughes, D.W., 1994. *MNRAS*, in press.

References

Allen, 1973. In *Astrophysical Quantities*, 3rd edn., Athlone Press, London.

Babadzhanov, P.B., 1994. In A. Milani et al. (eds.), *Asteroids, Comets, Meteors 1993*, p. 45.

Barnard, E., 1902. *Astron. Nachr.*, **157**, 260.

Benyukh, V.V., 1970. *Solar System Research*, **4**, 198.

Binzel, R.P., Farinella, P., Zappala, V. & Cellino, A., 1989. In *Asteroids II*, p. 416, eds. Binzel, R.P., Gehrels, T. & Matthews, M.S., University of Arizona Press.

Bortle, J.E., 1993. *Sky & Telesc.*, **86**, 107.

Boswell, J. & Hughes, D.W., 1992. *MNRAS*, **258**, 602.

Bowell, E., 1992. *IAU Circular*, 5585.

Bowell, E., Gehrels, T. and Zellner, B., 1979. In *Asteroids I*, p. 1108, ed Gehrels, T., University of Arizona Press.

Burns, J.A., Lamy, P.L. & Soter, S., 1979. *Icarus*, **40**, 1.

Bus, S.J., A'Hearn, M.F., Schleicher, D.G. & Bowell, E., 1991. *Science*, **251**, 774.

Ceplecha, Z., 1951. *Bull. Astr. Inst. Czech.*, **2**, 114.

Ceplecha, Z., 1992. *Astron. Astrophys.*, **263**, 361.

Chambers, G.F., 1889. In *A Handbook of Descriptive and Practical Astronomy*, 4th edn., **Vol. 1** (The Sun, Planets and Comets), p. 654, Oxford University Press.

Chapman, C.R., 1994. In A. Milani et al. (eds.), *Asteroids, Comets, Meteors 1993*, p. 357.

Chapman, C.R., Paolicchi, P., Zappala, V., Binzel, R.P. & Bell, J.F., 1989. In *Asteroids II*, p. 386, eds. Binzel, R.P., Gehrels, T. & Matthews, M.S., University of Arizona Press.

Cook, A.F., 1973. In *Evolution and Physical Properties of Meteors*, NASA SP-319, p. 183.

Davies, J.G. & Gill, J.C., 1960. *MNRAS*, **121**, 437.

Delsemme, A.H., 1982. In *Comets*, p. 85, ed. Wilkening L.L., Univ. of Arizona Press.

Dence, M.R., Grieve, R.A.F. & Robertson, P.B., 1977. In Roddy, D.J., Peppin, R.O. & Merrill, R.B., eds., *Impact and Explosion Craters, Planetary and Terrestrial Implications*, Pergamon, New York, p. 247.

Dermott, S.F., Durda, D.D., Gustafson, B.A.S., Jayaraman, S., Liou, J.C. & Xu, Y.L., 1994. In A. Milani et al. (eds.), *Asteroids, Comets, Meteors 1993*, p. 127.

Donnison, J.R. & Sugden, R.A., 1984. *MNRAS*, **210**, 673.

Drummond, J.D., 1981. *Icarus*, **45**, 545.

Farinella, P., 1982. *Icarus*, **52**, 409.

Farinella, P., Froeschle, C. & Gonczi, R., 1994. In A. Milani et al. (eds.), *Asteroids, Comets, Meteors 1993*, p. 205.

Fox, K., Williams, I.P. & Hughes, D.W., 1982. *MNRAS*, **199**, 313.

Fujiwara, A., Cerroni, P., Davis, D., Ryan, E., Di Martino, M., Holsapple, K. & Housen, K., 1989. In *Asteroids II*, p. 240, eds. Binzel, R.P., Gehrels, T. & Matthews, M.S., University of Arizona Press.

Gradie, J. & Tedesco, E., 1982. *Science*, **216**, 1905.

Green, D.W.E., 1993. *International Comet Quarterly*, **15**, 182. (see also *ICQ* **14**, 95).

Greenberg, R. & Nolan, M.C., 1989. In *Asteroids II*, p. 778, eds. Binzel, R.P., Gehrels, T. & Matthews, M.S., University of Arizona Press.

Grieve, R.A.F., 1984. *J. Geophys. Res.*, **89 Suppl.**, B403.

Harris, N.W. & Hughes, D.W., 1994. *MNRAS*, in press.

Harris, N.W., Yau, K. & Hughes, D.W., 1994. MNRAS, in press.

Hartmann, W.K., 1965. *Icarus*, **4**, 157, 207.

Hasegawa, I., 1993. in *Meteoroids and their Parent Bodies*, ed. Williams, I.P. & Stohl, J., Ast. Inst. Slovak Acad. Sci., Bratislava, p. 209.

Hawkins, G.S. & Almond, M., 1952. *MNRAS*, **112**, 219

Helin, E.F., 1992. In *Asteroids, Comets, Meteors 1991*, p. 235, eds. A.W. Harris and. E. Bowell, Lunar and Planetary Inst., Houston.

Hirayama, K., 1918. *Astron. J.*, **31**, 185.

Hughes, D.W., 1972. *Planet. Space Sci.*, **20**, 1949.

Hughes, D.W., 1974. *MNRAS*, **166**, 339.

Hughes, D.W., 1975. *Space Res.*, **15**, 565.

Hughes, D.W., 1977. *Space Res.*, **17**, 565.

Hughes, D.W., 1978. In *Cosmic Dust*, ed. McDonell, J.A.M., John Wiley & Sons, Chichister.

Hughes, D.W., 1982. *MNRAS*, **199**, 1149.

Hughes, D.W., 1985. *MNRAS*, **213**, 103.

Hughes, D.W., 1986. In *The Comet Nucleus Sample Return Mission*, p. 173, ESA S P-249.

Hughes, D.W., 1990a.In *Asteroids Comets Meteors III*, eds. Lagerkvist, C.I., Rickman, H., Lindblad, B.A. & Lindgren, M., Uppsala University Reprocentralen, Uppsala, p. 327.

Hughes, D.W., 1990b.*MNRAS*, **245**, 198.

Hughes, D.W., 1991. *Q. Jl. R. astr. Soc.*, **32**, 133.

Hughes, D.W., 1992. *Space Science Reviews*, **61**, 275.

Hughes, D.W., 1993. J.Stohl and I.P.Williams (eds.): *Meteoroids and their Parent Bodies*, p. 15.

Hughes, D.W., 1994. *MNRAS*, in press.

Hughes, D.W. & Emerson, B., 1982. *The Observatory*, **102**, 38.

Hughes, D.W. & Harris, N.W., 1994. *Planet. Space Sci.*, Vol. **42**, No. 4, p. 291.

Hughes, D.W. & McBride, N., 1989. *MNRAS*, **240**, 73.

Hughes, D.W., Williams, I.P. & Fox, K., 1981. *MNRAS*, **195**, 625.

Imoto, S., Hasegawa, I., 1958. *Smithson. Contr. Astrophys.*, **2**, 131.

Jacchia, L.G. & Whipple, F.L., 1956. In *Vistas in Astronomy*, ed. A. Beer, **Vol.2**, Pergamon, London.

Jones, J. & Wheaton, K.R., 1985. *Observatory*, **105**, 34.

Kashcheyev, B.L. & Lebedinets, V.N., 1967. *Smithson. Contrib. Astrophys.*, **11**, 183.

Kirkwood, D., 1867. *Meteoric Astronomy*, Lippincott, Philadelphia.

Kronk, G.W., 1984. *Comets a Descriptive Catalog*, Enslow Pub. Inc., Hillside, N.J., **304**, p. 15.

Lebofsky, L.A., & Spencer, J.R., 1989. In *Asteroids II*, p. 128, eds. R.P. Binzel, T. Gehrels & M.S. Matthews, University of Arizona Press.

Leinert, C.H. & Grün, E., 1989. In *Physics of the Inner Heliosphere*, eds. Schwenn, R. & Marsch, E., Springer press.

Lindblad, B.A., 1971. *Smithson. Contrib. Astrophys.*, **12**, 14.

Lindblad, B.A., 1987. In *Interplanetary Matter*, eds. Ceplecha, Z. & Pecina, P., Proc. 10th European Reg. Meeting of the IAU, **vol. 2**, Prague, p. 201.

Lindblad, B.A., 1991. In Levasseur-Regourd A.C., Hasegawa H., eds., *Origin and Evolution of Interplanetary Dust*, Kluwer Acad. Publishers, p. 311.

Lovell, A.C.B., 1954. *Meteor Astronomy*, Oxford Univ. Press, p. 400.

Luu, J., 1994. In A. Milani et al. (eds.), *Asteroids, Comets, Meteors 1993*, p. 31.

Marsden, B.G., 1973. *A.J.*, **78**, 662.

Marsden, B.G., 1986. *Catalogue of Cometary Orbits*, 5th edn., Minor Planet Centre, Cambridge, Mass.

Marsden, B.G., 1993 . *Sky & Telescope*, **85**, 16.

Marsden, B.G., Williams, G.V., Kronk, G.W. and Waddington, W.G., 1993 . *Icarus*, **105**, 420.

McBride, N. & Hughes, D.W., 1990a.In Lagerkvist, C.I., Rickman, H., Lindblad B.A. & Lindgren M., eds, *Asteroids Comets Meteors III*, Uppsala University Reprocentralen, Uppsala, p. 555.

McBride, N. & Hughes, D.W., 1990b.*MNRAS*, **244**, 513.

McBride, N. & Hughes, D.W., 1992. In *Asteroids Comets Meteors IV*, Ed. A.W.Harris & E.Bowell, Lunar and Planetary Institute, Houston, p. 403.

McFadden, L-A., Tholen, D.J. & Veeder, G.J., 1989. In *Asteroids II*, p. 442, eds. R.P. Binzel, T. Gehrels & M.S. Matthews, Univ. of Arizona Press.

McKinley, D.W.R., 1967. In *Meteor Science and Engineering*, McGraw-Hill, New York.

Meech, K.J. & Belton, M.J.S., 1990. *Astron. J.*, **100**, 1323.

Mobberley, M.P., 1994. *J. Brit. Astron. Assoc.*, **104**, 11.

Morrison, D., 1977. In *Comets, Asteroids, Meteorites*, p. 177, ed. Delsemme, A.H., University of Toledo Press.

Morrison, D., 1993. *The Spaceguard Survey*, JPL.

Neukum, G. & Wise, D.U., 1976. *Science*, **194**, 1381.

Nilsson, C.S., 1964. *Aust. J. Phys.*, **17**, 205.

Olivier, C.P., 1925. *Meteors*, Baltimore, Williams & Williams, ch. 5.

Olsson-Steel, D., 1986. *MNRAS*, **219**, 47.

Oort, J.H., 1950. *Bull. Astr. Inst. Neth.*, **11**, 91.

Öpik, E.J., 1951. *Proc. R.I.A.*, **Vol.54**, Sect. A.

Paolicchi, P., Cellino, A., Farinella, P. & Zappala, V., 1989. *Icarus*, **77**, 187.

Plavec, M., 1955. *Bull. Astr. Inst. Czech.*, **6**, 20.

Poole, L.M.G. & Kaiser, T.R., 1972. *MNRAS*, **156**, 283.

Porter, J.G., 1952. *Comets and Meteor Streams*, Chapman and Hall, London, p. 117.

Rabinowitz, D.L., 1993. *Astrophys. J.*, **407**, 412.

Rabinowitz, D.L., Gehrels, T. & Scotti, J.V., 1993. *Nature*, **363**, 704.

Richter, N.B., 1960. *Die Sterne*, **36**, 125.

Richter, N.B., 1963. In *The Nature of Comets*, p. 168, Methuen.

Robertson, H.P., 1937. *MNRAS*, **97**, 423.

Roy, A.E., 1978. *Orbital Motion*, p. 310, Adam Hilger, Bristol.

Roy, A.E., 1982. *Orbital Motion*, 2nd edn., p. 79, Adam Hilger, Bristol.

Sekanina, Z., 1981. *AJ*, **86**, 1741.

Shoemaker, E.M., 1965. *JPL. Tech. Rep.*, No. **32-700**, p. 75.

Shoemaker, E.M., Williams, J.G., Helin, E.F. & Wolfe, R.F., 1979. In *Asteroids*, T.Gehrels, ed., p. 253, Univ. of Arizona Press, Tucson.

Shoemaker, E.M., Shoemaker, C.S. & Wolfe, R.F., 1989. In *Asteroids II*, p. 487, ed. Binzel, R.P., Gehrels, T. & Matthews, M.S., University of Arizona Press.

Southworth, R.B., & Hawkins, G.S., 1963. *Smithson. Contrib. Astrophys.*, **7**, 261.

Sykes, M.V., Greenberg, R., Dermott, S.F., Nicholson, P.D., Burns, J.A., Gautier, T.N.III, 1989. In *Asteroids II*, p. 336, eds. R.P. Binzel, T. Gehrels & M.S. Matthews, Univ. of Arizona Press.

Tedesco, E.F., 1989. In *Asteroids II*, p. 1090, ed. Binzel, R.P., Gehrels, T. & Matthews M.S., University of Arizona Press.

Terentjeva, A.K., 1967. *Smithson. Contrib. Astrophys.*, **11**, 109.

Tokhtas'ev, V.S., 1978. *Summaries of Reports of All-Union Symposium on the Interaction of Cosmic Material with the Earth's Atmosphere*, Moskow-Frunze, p. 32 (in Russian).

Verniani, F., 1969. *Space Sci. Rev.*, **10**, 230.

Verniani, F., 1973. *J. Geophys. Res.*, **78**, 8429.

Wasson, J.T. & Wetherill, G.W., 1979. In *Asteroids*, ed. T. Gehrels, p. 926, University of Arizona Press.

Wetherill, G.W., 1974. *A. Rev. Earth Planet. Sci.*, **2**, 303.

Wetherill, G.W. & Williams, J.G., 1968. *J. Geophys. Res.*, **73**, 635.

Whipple, F.L., 1938. *Proc. Amer. Phil. Soc.*, **79**, 499.

Whipple, F.L., 1949. *Sky & Telescope*, **8**, No.4.

Whipple, F.L., 1950. *Astrophys. J.*, **111**, 375.

Whipple, F.L., 1951. *Astrophys. J.*, **113**, 464.

Whipple, F.L., 1954. *Astron. J.*, **59**, No.6.

Whipple, F.L., 1967. *NASA special publication* **no. 150**, p. 409.

Williams, I.P. & Wu, Z., 1993. *MNRAS*, **264**, 659.

Williams, I.P., Murray, C.D. & Hughes, D.W., 1979. *MNRAS*, **189**, 483.

Wisdom, J., 1983. *Icarus*, **56**, 51.

Wood, J.A., 1979. *The Solar System*, Prentice-Hall, New Jersey, p. 41.

Wu, Z., & Williams, I.P., 1993. *MNRAS*, **264**, 980.

Wyckoff, S., 1982. In *Comets*, p. 3, ed. Wilkening L.L., Univ. of Arizona Press.

Yau, K., Yeomans, D. & Weissman, P., 1994. *MNRAS*, **266**, 305.

Zellner, B. & Bowell, E., 1977. In *Comets, Asteroids, Meteorites*, p. 185, ed. A.H. Delsemme, Univ of Toledo.